Supplementary Materials

Supplementary Tables

Supplementary Table 1: Mapping statistics for SMAC-seq datasets in this study

sample	number reads	total bases	mean read length	median read length
Sample 1	847,262	3,475,258,237	4,102	1,474
diamide 0 min rep1	2,462,311	4,018,221,647	1,632	722
diamide 30 min rep1	1,127,937	3,376,196,280	2,993	1,254
diamide 60 min rep1	1,543,217	4,187,296,821	2,713	1,171
diamide 0 min rep2	2,605,209	7,815,151,882	3,000	1,383
diamide 30 min rep2	2,266,191	6,046,929,720	2,668	977
diamide 60 min rep2	1,397,628	5,335,378,307	3,817	1,919
positive control gDNA High EcoGII	553	4,345,539	7,858	3,706
positive control gDNA Low EcoGII	11,265	137,959,334	12,247	6,383
negative control gDNA	740,001	3,437,777,966	4,646	1,161
negative control λ DNA	120,711	455,213,644	3,771	2,528
positive control λ DNA EcoGII	311,974	895,965,634	2,872	1,950
GM12878 m^6A-SMAC	1,054,719	5,385,628,670	5,106	2,768

Supplementary Table 2: Mapping and QC statistics for ATAC-seq datasets used in this study

Dataset	Complexity	TSS ratio	Read Length	uniquely mapped deduplicated reads	Raw fragments
L464 Diamide 0 min rep1	0.79	1.38	2×36	2,284,992	2,363,608
L465 Diamide 0 min rep2	0.79	1.36	2×36	2,383,094	2,409,446
L466 Diamide 15 min rep1	0.77	1.49	2×36	1,907,268	1,760,891
L467 Diamide 15 min rep2	0.75	1.42	2×36	3,415,058	3,058,834
L468 Diamide 30 min rep1	0.72	1.49	2×36	3,223,114	3,414,835
L469 Diamide 30 min rep2	0.74	1.41	2×36	3,081,970	2,846,193
L470 Diamide 45 min rep1	0.79	1.37	2×36	2,411,938	2,457,100
L471 Diamide 45 min rep2	0.75	1.40	2×36	3,135,316	2,885,651
L472 Diamide 60 min rep1	0.74	1.45	2×36	3,205,726	3,120,294
L473 Diamide 60 min rep2	0.76	1.43	2×36	2,387,398	2,244,141

Supplementary Table 3: Mapping and QC statistics for ChIP-seq datasets used in this study

Dataset	Complexity	Read Length	Uniquely mapped deduplicated reads	Raw fragments
L482 Diamide 0 min Input	0.88	2 × 36	8,776,410	5,488,322
L483 Diamide 0 min Pol2	0.87	2 × 36	4,944,766	2,894,414
L484 Diamide 0 min Pol2pS2	0.80	2 × 36	5,834,864	3,434,723
L485 Diamide 0 min HSF1-V5 Input	0.90	2 × 36	6,089,572	3,850,484
L486 Diamide 0 min HSF1-V5	0.93	2 × 36	2,540,876	1,726,223
L487 Diamide 30 min Input	0.86	2 × 36	10,052,178	6,212,240
L488 Diamide 30 min Pol2	0.84	2 × 36	6,763,128	3,961,384
L489 Diamide 30 min Pol2pS2	0.84	2 × 36	6,332,462	3,901,689
L490 Diamide 30 min HSF1-V5 Input	0.92	2 × 36	4,587,466	2,831,871
L491 Diamide 30 min HSF1-V5	0.89	2 × 36	3,324,498	2,054,869
L492 Diamide 60 min Input	0.90	2 × 36	5,812,736	3,539,630
L493 Diamide 60 min Pol2	0.90	2 × 36	3,774,106	2,204,126
L494 Diamide 60 min Pol2pS2	0.85	2 × 36	4,873,244	2,924,345
L495 Diamide 60 min HSF1-V5 Input	0.87	2 × 36	7,683,586	4,679,564
L496 Diamide 60 min HSF1-V5	0.91	2 × 36	1,094,048	698,664

Supplementary Table 4: Mapping and QC statistics for RNA-seq datasets used in this study

Dataset	Complexity	Read Length	Unique	Unique Splices	Multi	Multi Splices	Raw fragments
Diamide 0 min	0.20	2 × 75	30,692,672	461,804	3,974,211	38,859	18,719,790
Diamide 15 min	0.21	2 × 75	26,991,043	182,208	3,217,924	18,788	15,960,277
Diamide 30 min	0.19	2 × 75	34,711,193	201,334	3,716,196	21,450	21,717,800
Diamide 45 min	0.22	2 × 75	28,668,901	116,773	3,103,601	19,301	17,832,222
Diamide 60 min	0.31	2 × 75	14,991,437	71,198	1,759,048	10,455	13,548,619
Diamide Hsf-V5 0min	0.19	2 × 75	32,981,363	519,649	4,320,132	35,513	21,535,487
Diamide Hsf-V5 30min	0.19	2 × 75	33,505,595	211,992	3,973,770	23,016	22,974,020
Diamide Hsf-V5 60min	0.19	2 × 75	40,290,524	196,082	4,698,437	29,628	28,894,301

Supplementary Figures

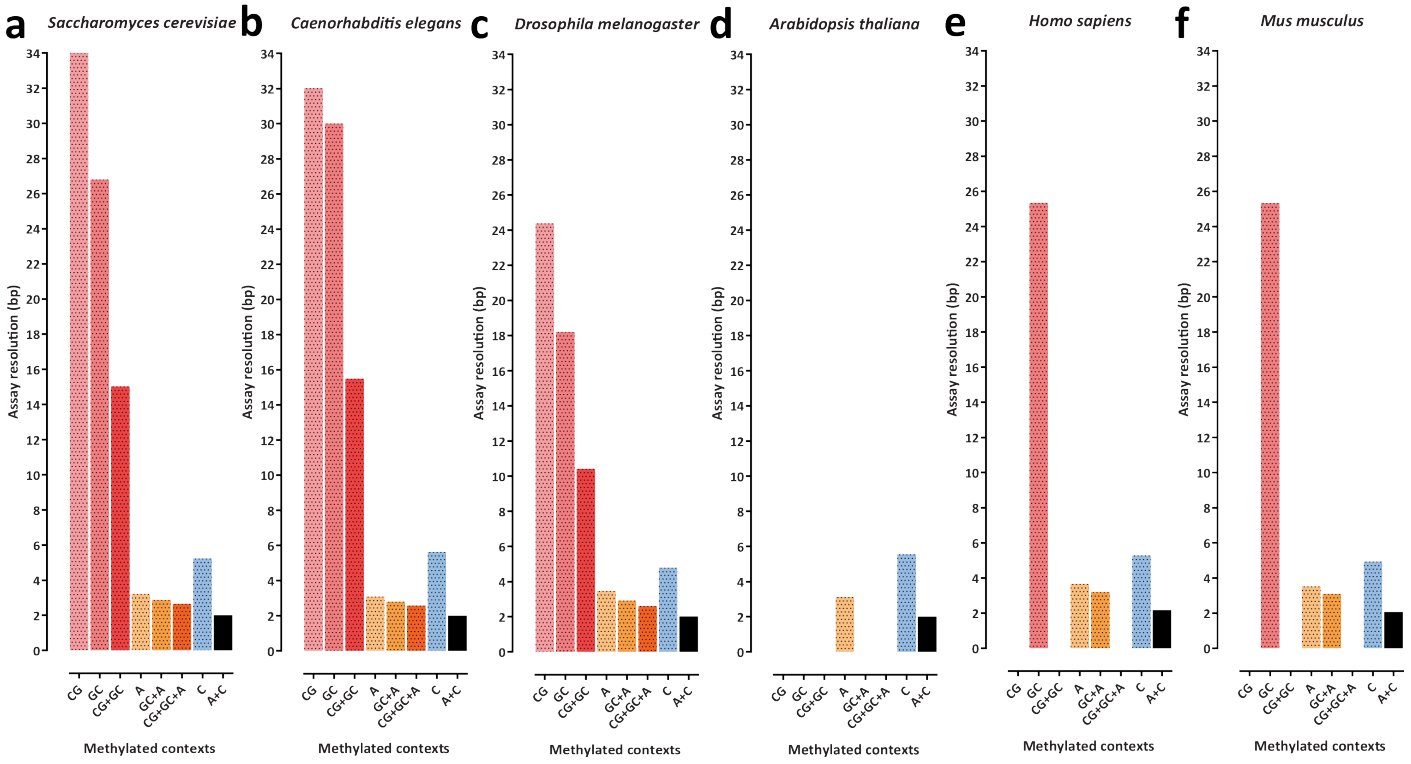

Supplementary Figure 1: Resolution of the SMAC-seq assay in its current form and some potential other versions of it in the main model organism systems. Note that where endogenous methylation confounds readout of accessibility, the corresponding combination of sequence contexts has been omitted from the plot. Also note that while m^6A has been reported to be present in the genomes of *Arabidopsis*[68] and *C. elegans*[69], it is generally found at low levels ($\leq 1\%$), and is not as strongly correlated with open chromatin and nucleosome positioning as it is in some other eukaryotes such as *Chlamydomonas*[47], thus its utility for accessibility profiling is not altered significantly. Nevertheless, a universally applicable version of SMAC-seq that is minimally confounded by endogenous methylation status in all eukaryotes will probably require the use of different methyltransferases (once they become available as efficient recombinant enzymes), for example, ones depositing the 4mC mark, which is what the "C" sequence context shown here corresponds to. (a) *Saccharomyces cerevisiae* (complete absence of endogenous methylation); (b) *Caenorhabditis elegans* (no endogenous 5mC, small amounts of endogenous m^6A); (c) *Drosophila melanogaster* (no significant endogenous 5mC or m^6A methylation); (d) *Arabidopsis thaliana* (endogenous 5mC in CpG, CHG and CHH contexts, small amounts of endogenous m^6A); (e) *Homo sapiens* (endogenous 5mC in CpG contexts, small amounts of endogenous 5mC in CHG and CHH contexts); (f) *Mus musculus* (endogenous 5mC in CpG contexts, small amounts of endogenous 5mC in CHG and CHH contexts).

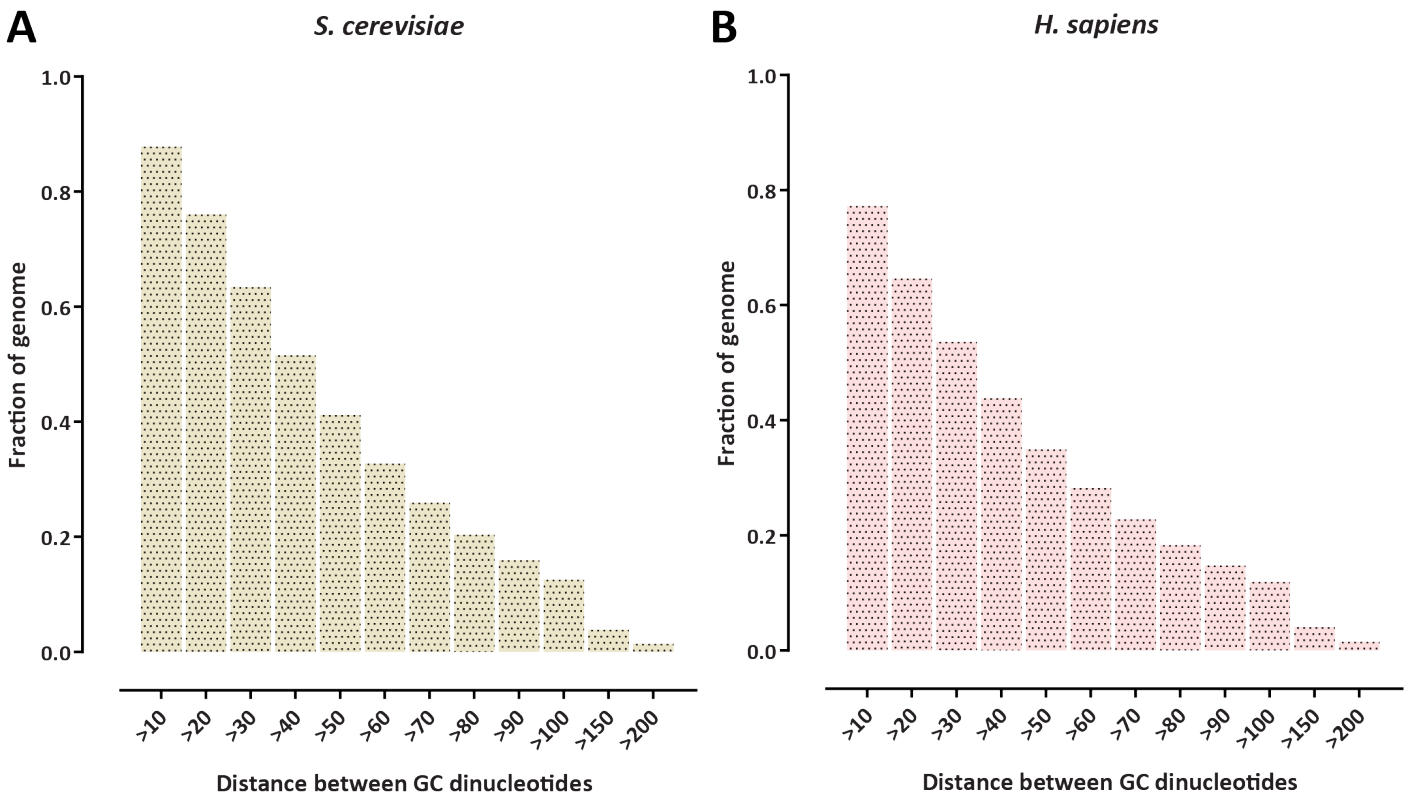

Supplementary Figure 2: GC positions alone are insufficient to provide proper coverage of the genome in the context of a methylation-based assay for profiling chromatin accessibility. Shown is the distribution of the fraction of the genome that contains no GC dinucleotides closer to each other than the indicated distance. The mitochondrial genome was excluded from the calculation. (a) *Saccharomyces cerevisiae*; (b) *Homo sapiens*. More than 50% of each genome consists of regions with GC dinucleotides spaced at least 30 bp apart (and 40 bp in the case of *S. cerevisiae*), i.e longer than a typical nucleosome linker.

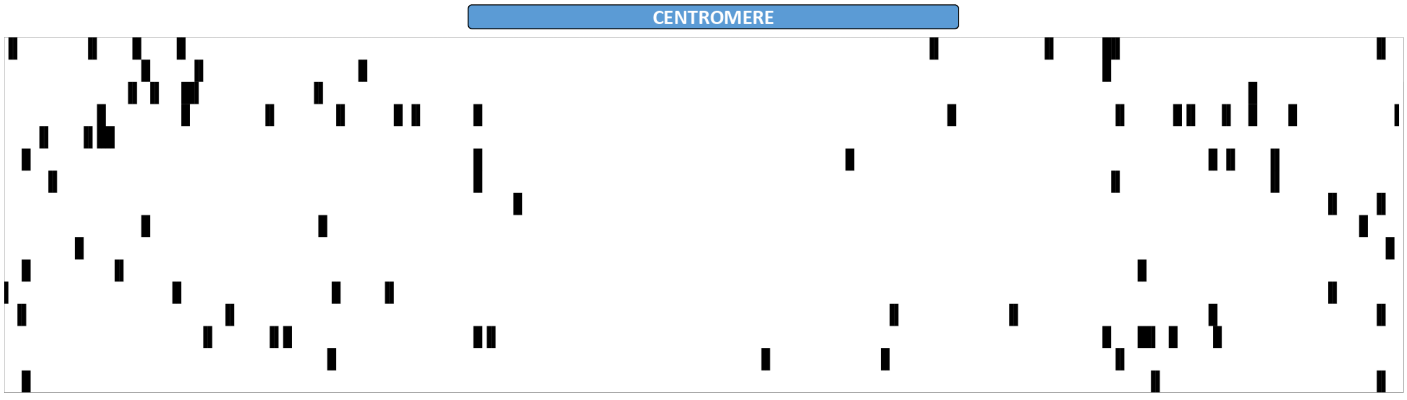

Supplementary Figure 3: Important functional elements in the yeast genome, such as, in this example, centromeres, are almost completely devoid of GC/GC dinucleotides. Shown is the distribution of GC dinucleotides (black rectangles) around *S. cerevisiae* centromeres.

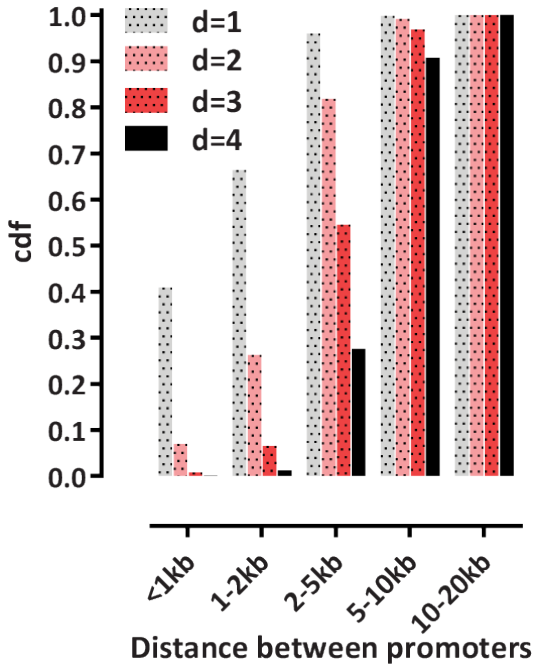

Supplementary Figure 4: Distance between regulatory elements (i.e. promoters in the case of *S. cerevisiae*).

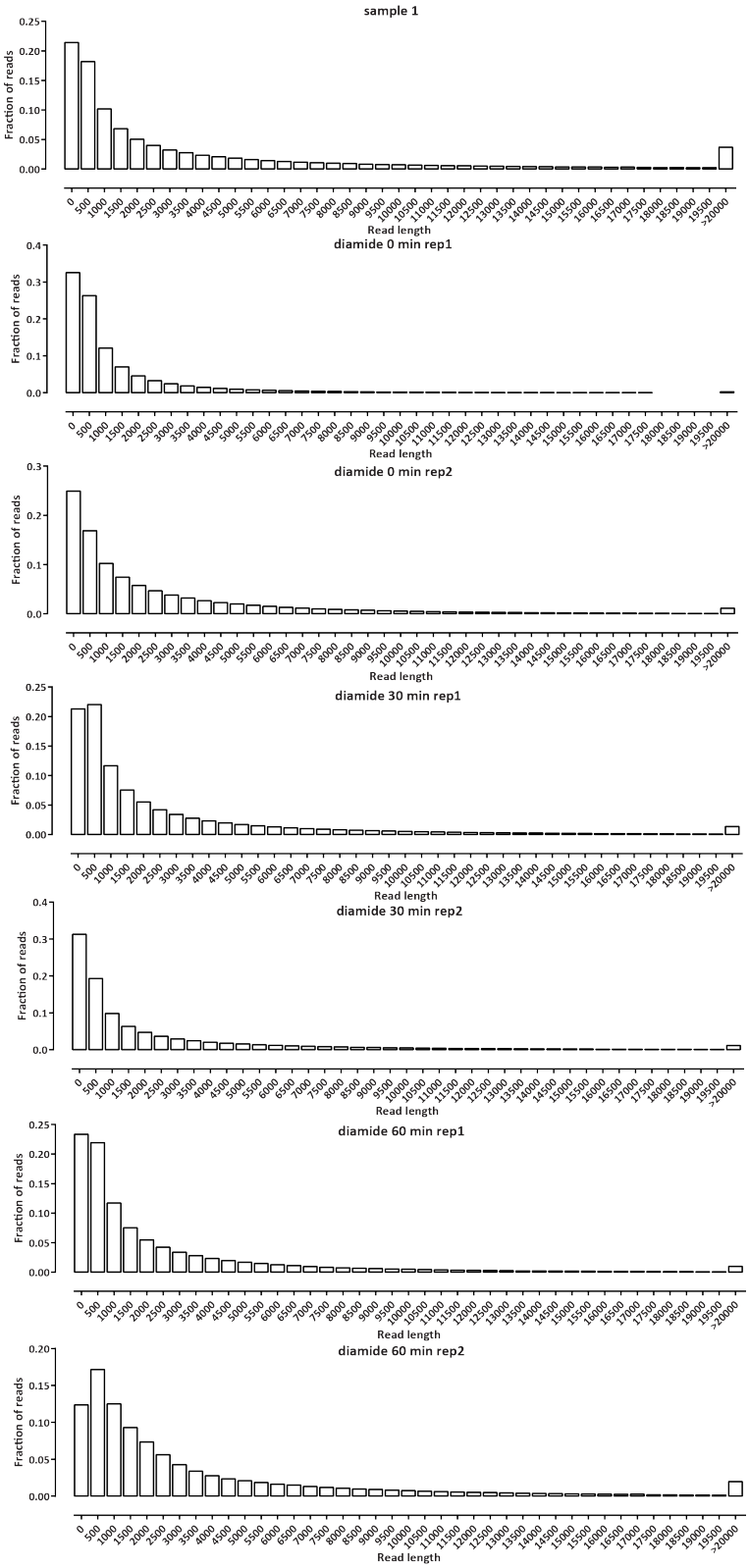

Supplementary Figure 5: Distribution of nanopore read lengths obtained for the experiments described in this study.

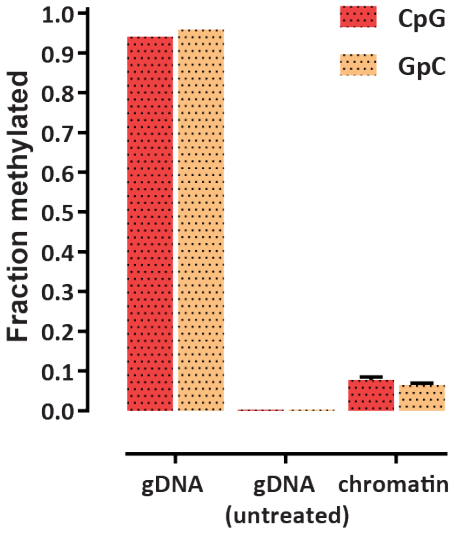

Supplementary Figure 6: Global methylation levels in yeast dSMF experiments and in positive and negative controls (measured by bisulfite sequencing). DNA from SMAC-seq experiments was subjected to Illumina bisulfite sequencing using the PBAT protocol. In parallel, naked genomic DNA (gDNA) was either treated with all three enzymes under the same conditions as in the SMAC-seq protocol or it was left untreated. These samples were also subjected to Illumina PBAT bisulfite sequencing. Shown are the global methylation levels for each sample.

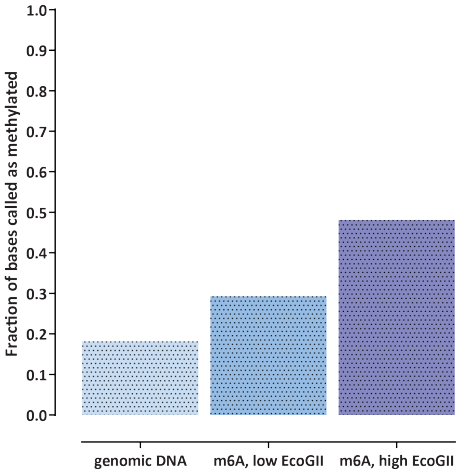

Supplementary Figure 7: Global m^{6}A methylation levels in positive and negative controls (measured by nanopore sequencing). Yeast genomic DNA was incubated with no or a low/high amount of the EcoGII enzyme and then subjected to nanopore sequencing. Shown are the average methylation levels for A nucleotides. Note that completely methylated DNA molecules are not sequenced well on the nanopore platform (See also Supplementary Table 1), thus the methylation estimates in the treated samples are most likely underestimates.

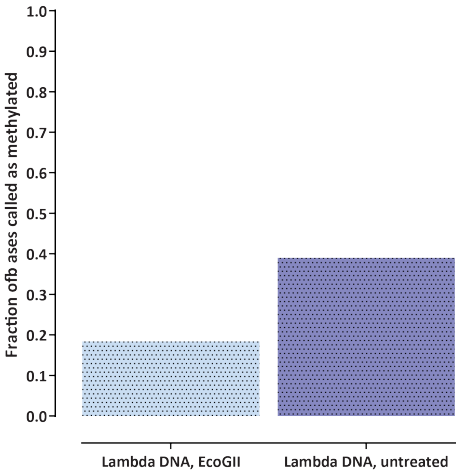

Supplementary Figure 8: Global m^6A methylation levels in positive and negative controls (measured by nanopore sequencing). Unmethylated Lambda DNA was incubated with the EcoGII enzyme and then subjected to nanopore sequencing. Shown are the average methylation levels for A nucleotides. Note that completely methylated DNA molecules are not sequenced well on the nanopore platform, thus the methylation estimates in the treated sample are most likely underestimates.

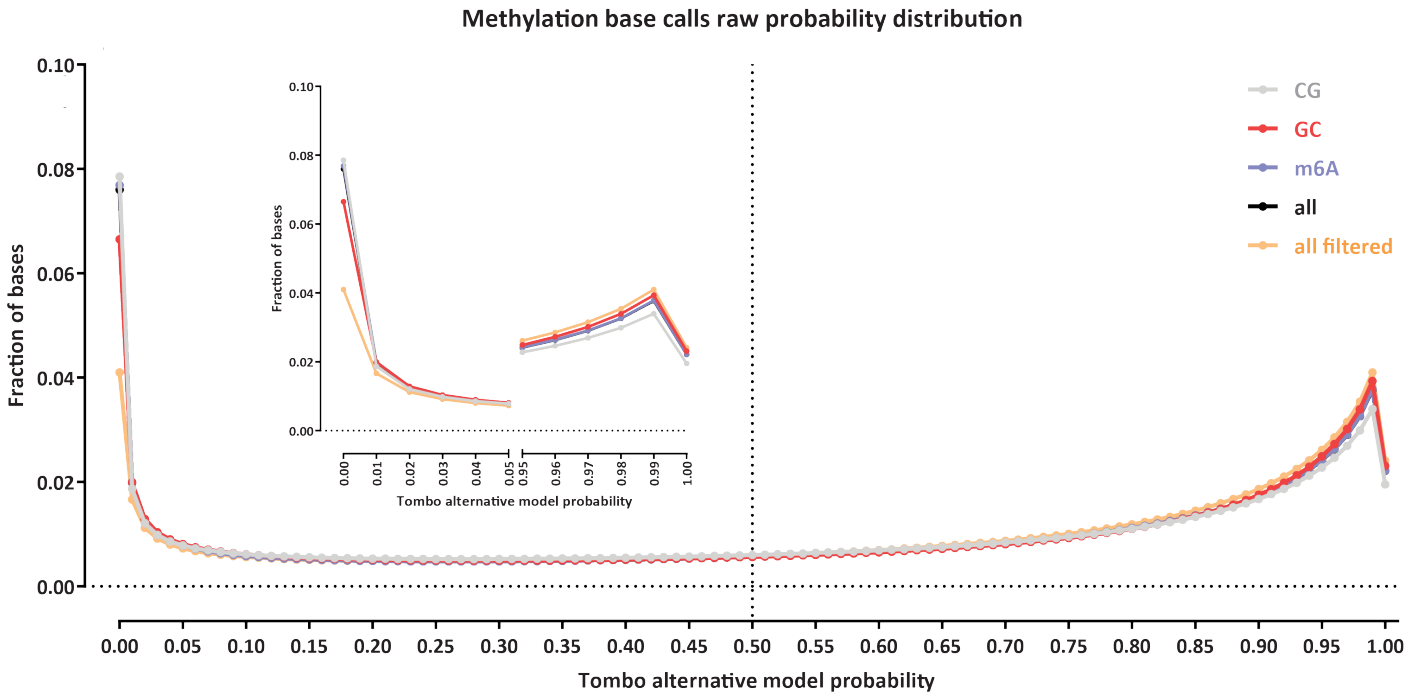

Supplementary Figure 9: Distribution of methylation call probabilities. Shown is the distribution of Tombo "alternative model" probabilities for all positions, and each of the three sequence contexts, as well as the distribution after filtering potential poor quality/non-chromatinized reads (see further below for more details).

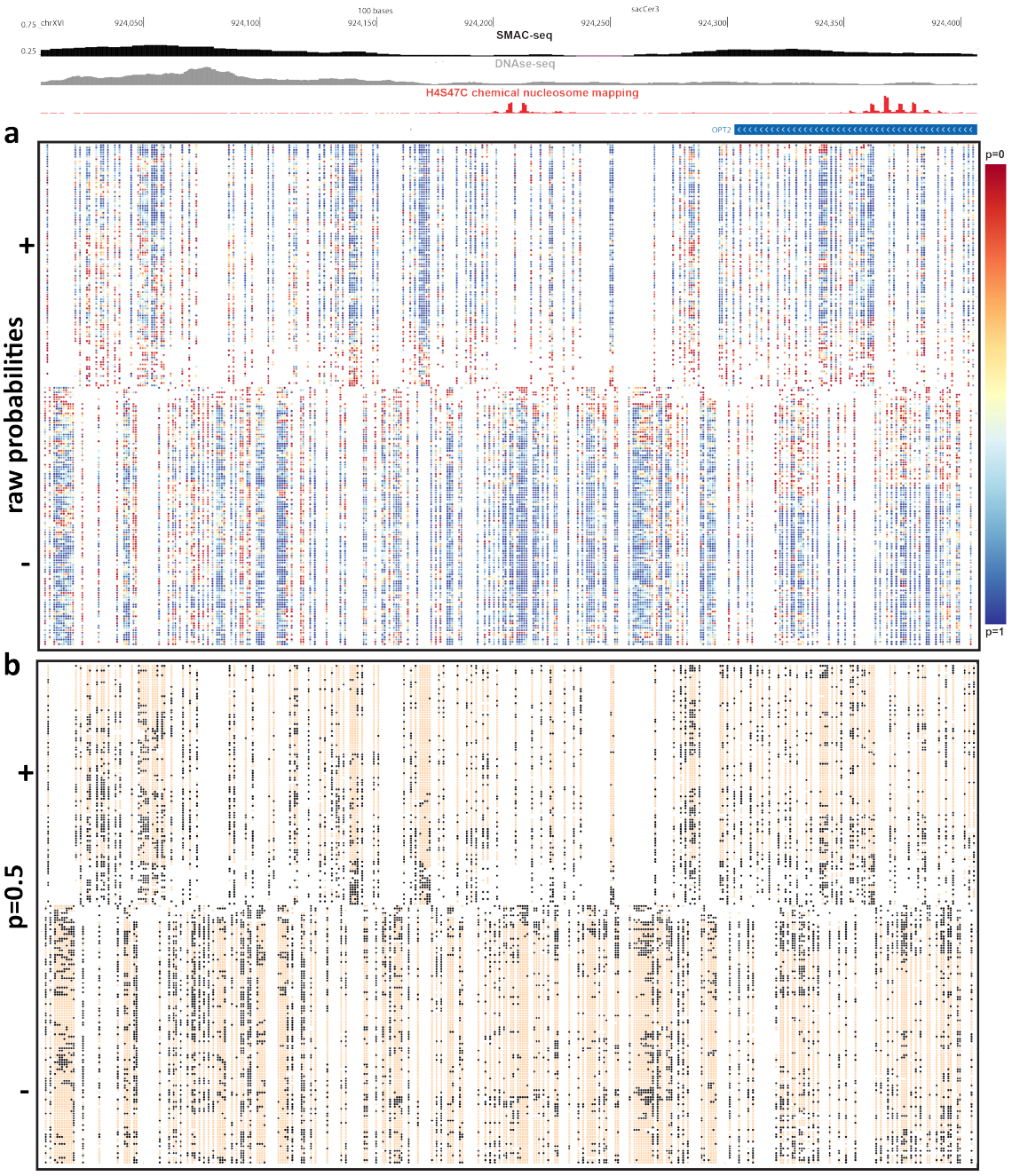
100 bases
sacCer3
0.75
chrXVI
924,050
924,100
924,150
924,200
924,250
924,300
924,350
924,400
SMAC-seq
0.25
DNAse-seq
H4S47C chemical nucleosome mapping
OPT2
a
raw probabilities
+
-
p=0
p=1
b
p=0.5
+
-

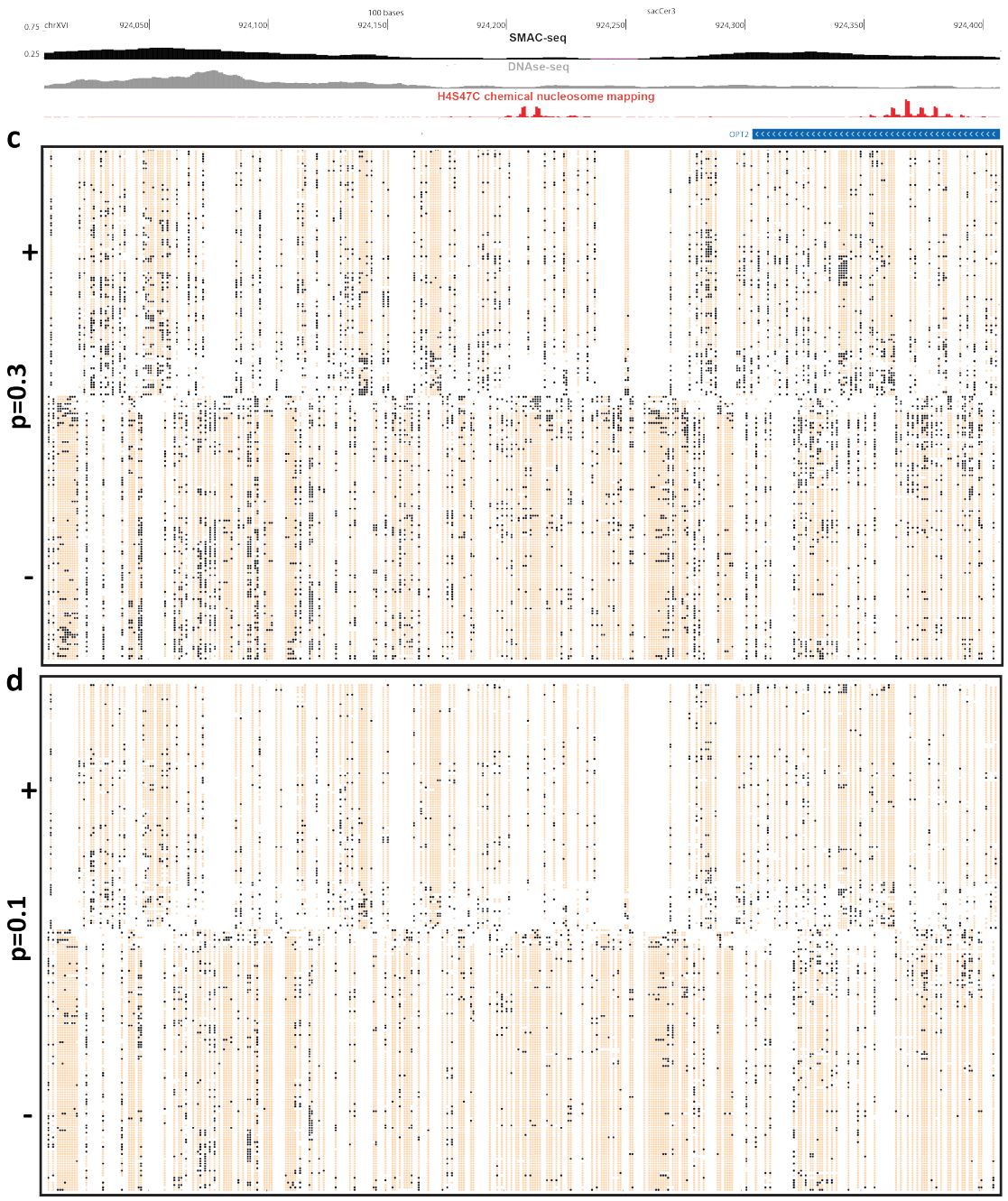

Supplementary Figure 10: Transformation of raw methylation probabilities into binary methylation calls. Shown is raw unfiltered SMAC-seq single-molecule data over a strongly positioned nucleosome on chrXVI (1-bp resolution). White spaces indicate positions for which there is no data (i.e. no CG, GC or A). (a) raw Tombo alternative model methylation probabilities; (b) $p < 0.5$ thresholding; (d) $p < 0.3$ thresholding; (d) $p < 0.1$ thresholding.

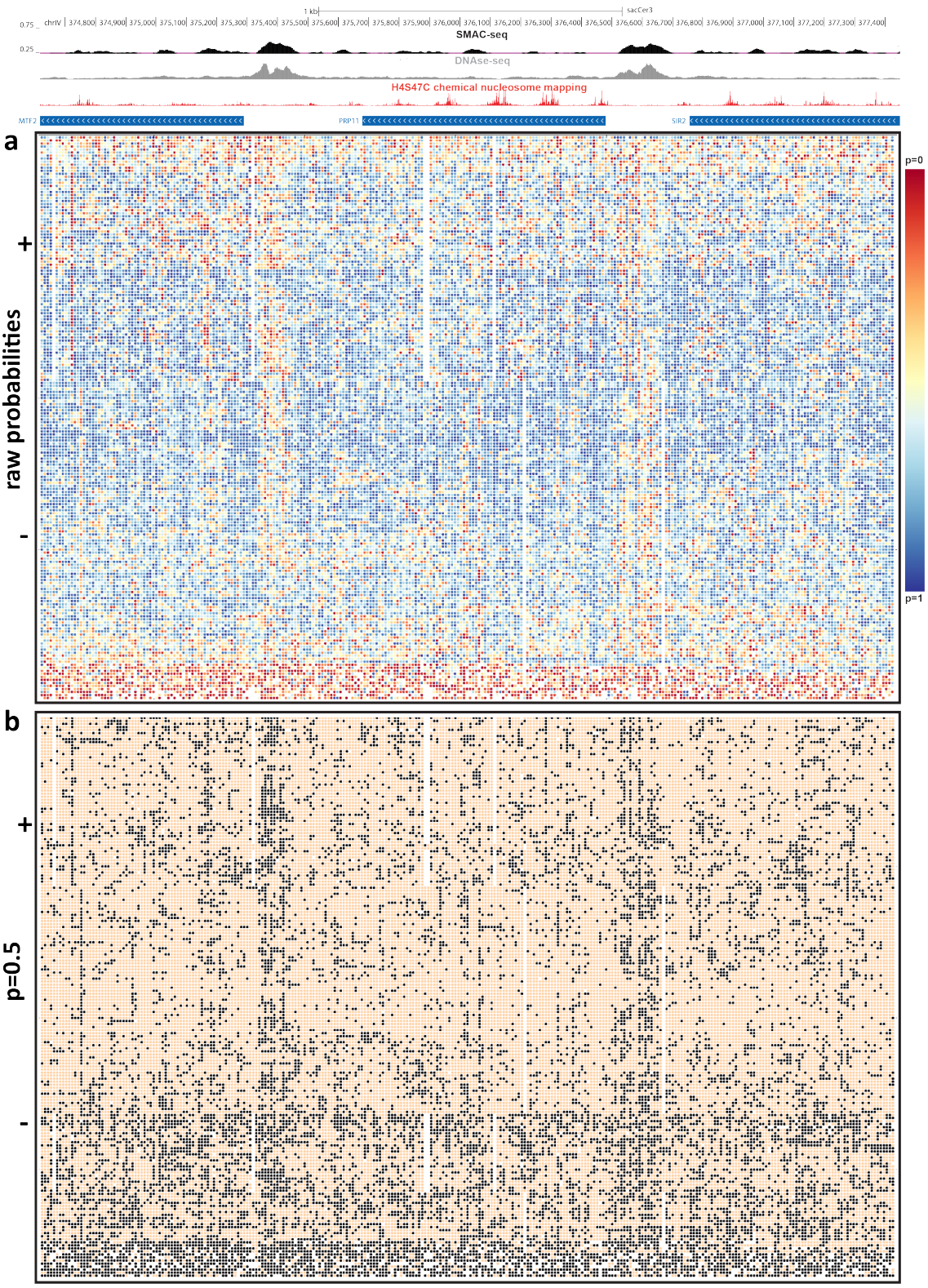
1 kb
sacCer3
chrIV
SMAC-seq
DNAse-seq
H4S47C chemical nucleosome mapping
MTF2
PRP11
SIR2
a
raw probabilities
+
-
p=0
p=1
b
p=0.5
+
-

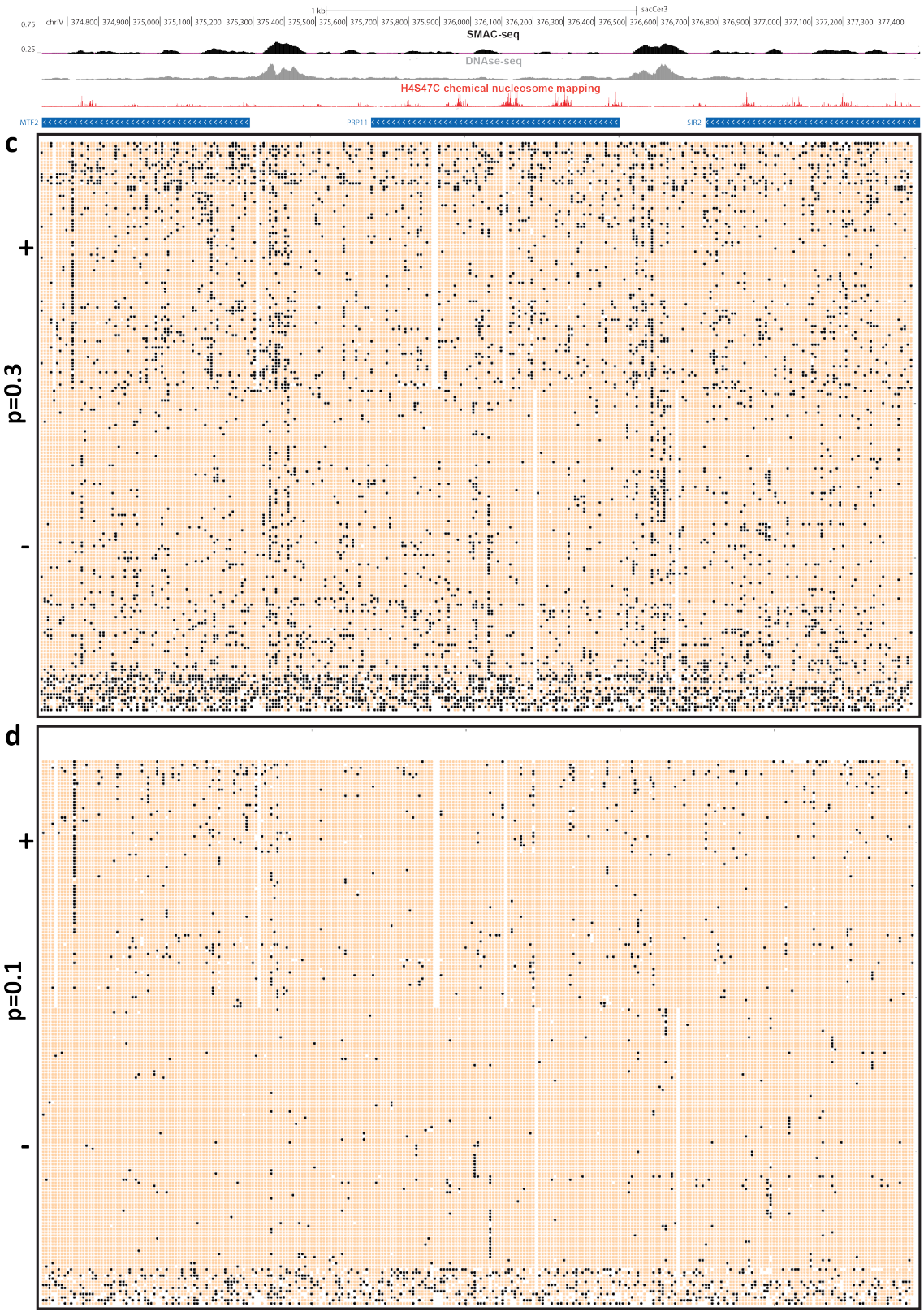

Supplementary Figure 11: Transformation of raw methylation probabilities into binary methylation calls. Shown is raw unfiltered SMAC-seq single-molecule data over a ∼2.8kb locus on chrIV (10-bp average for all panels). White spaces indicate positions for which there is no data (i.e. no CG, GC or A). (a) raw Tombo alternative model methylation probabilities; (b) $p < 0.5$ thresholding; (d) $p < 0.3$ thresholding; (d) $p < 0.1$ thresholding.

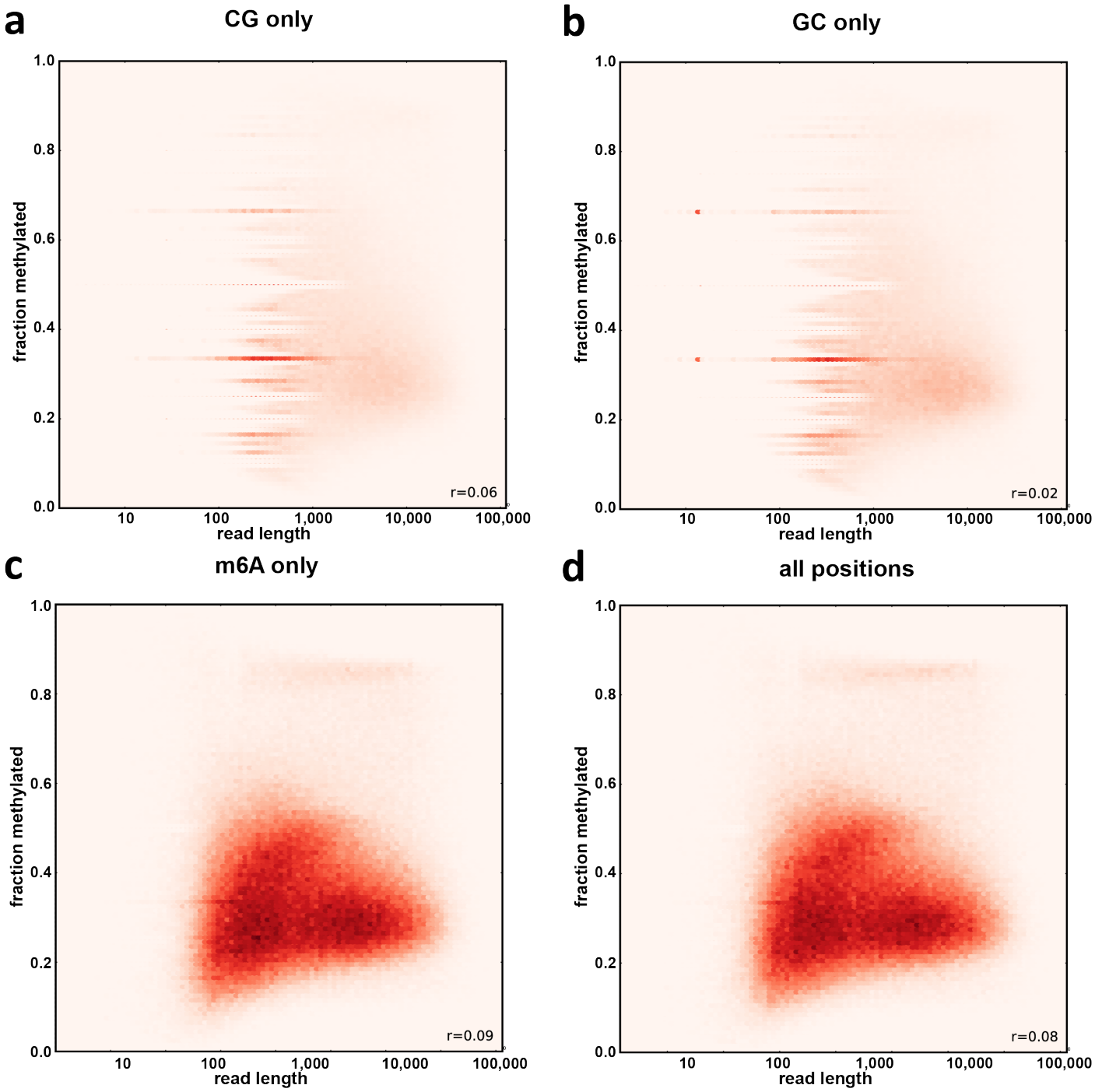

Supplementary Figure 12: Absence of strong correlation between nanopore sequencing read length and methylation status. Shown is the fraction of bases within each read that is scored as methylated. (a) CG positions only. (b) GC positions only. (c) m^6A positions only. (d) All positions.

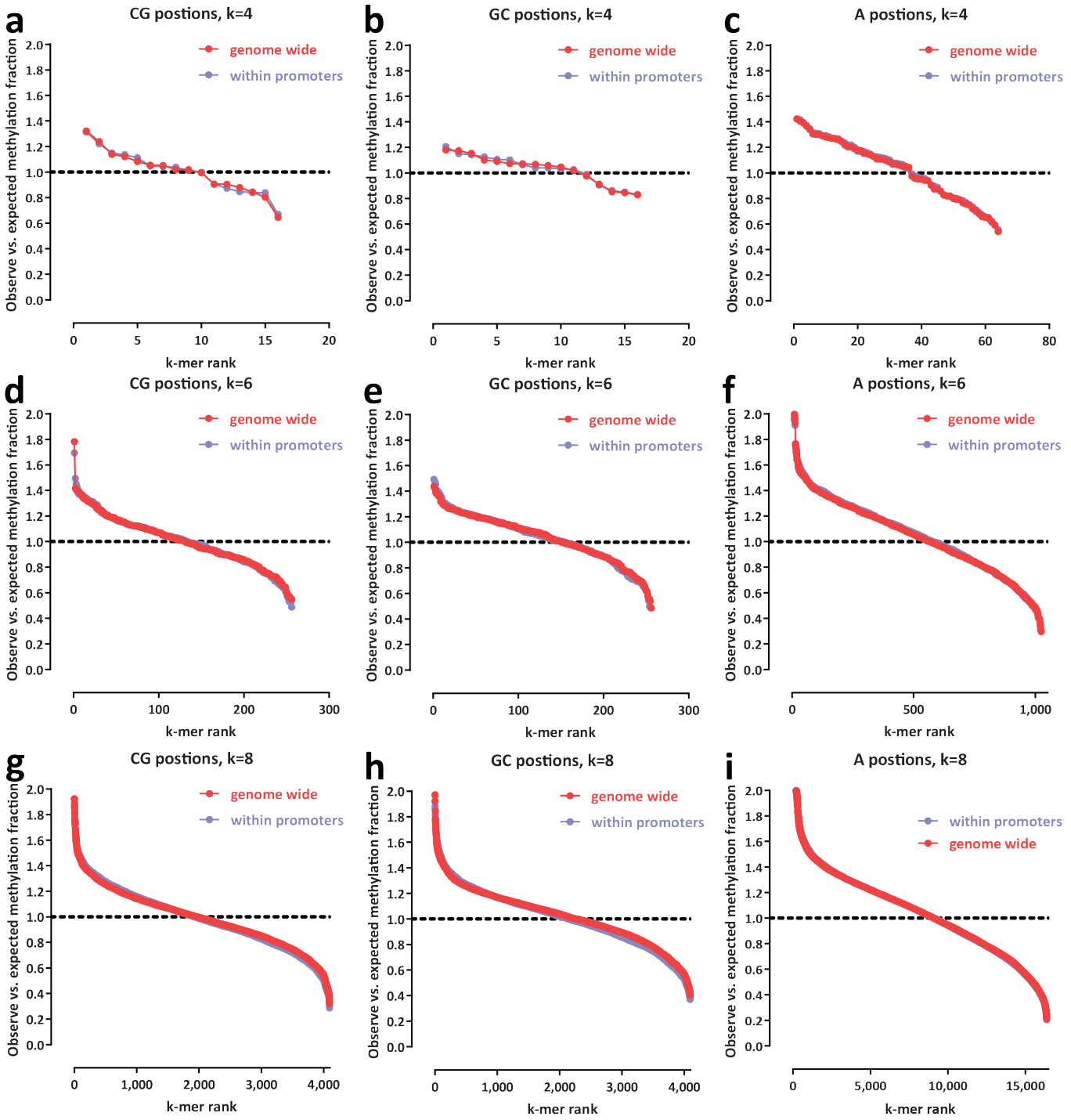

Supplementary Figure 13: Examination of enzymatic/methylated base calling bias. Shown is the ratio of observed versus expected fraction of methylated bases for each sequence context of size k, calculated as follows:

$$f_{\text{obs/exp},k} = \frac{k_m/k_u}{\sum_k k_m / \sum_k k_u}$$

where k_m refers to the number of bases called as methylated across all reads and k_m refers to the number of bases called as unmethylated . (a) CG positions only, $k = 4$. (b) GC positions only, $k = 4$. (c) A positions only, $k = 4$. (d) CG positions only, $k = 6$. (e) GC positions only, $k = 6$. (f) A positions only, $k = 6$. (g) CG positions only, $k = 8$. (h) GC positions only, $k = 8$. (i) A positions only, $k = 8$.

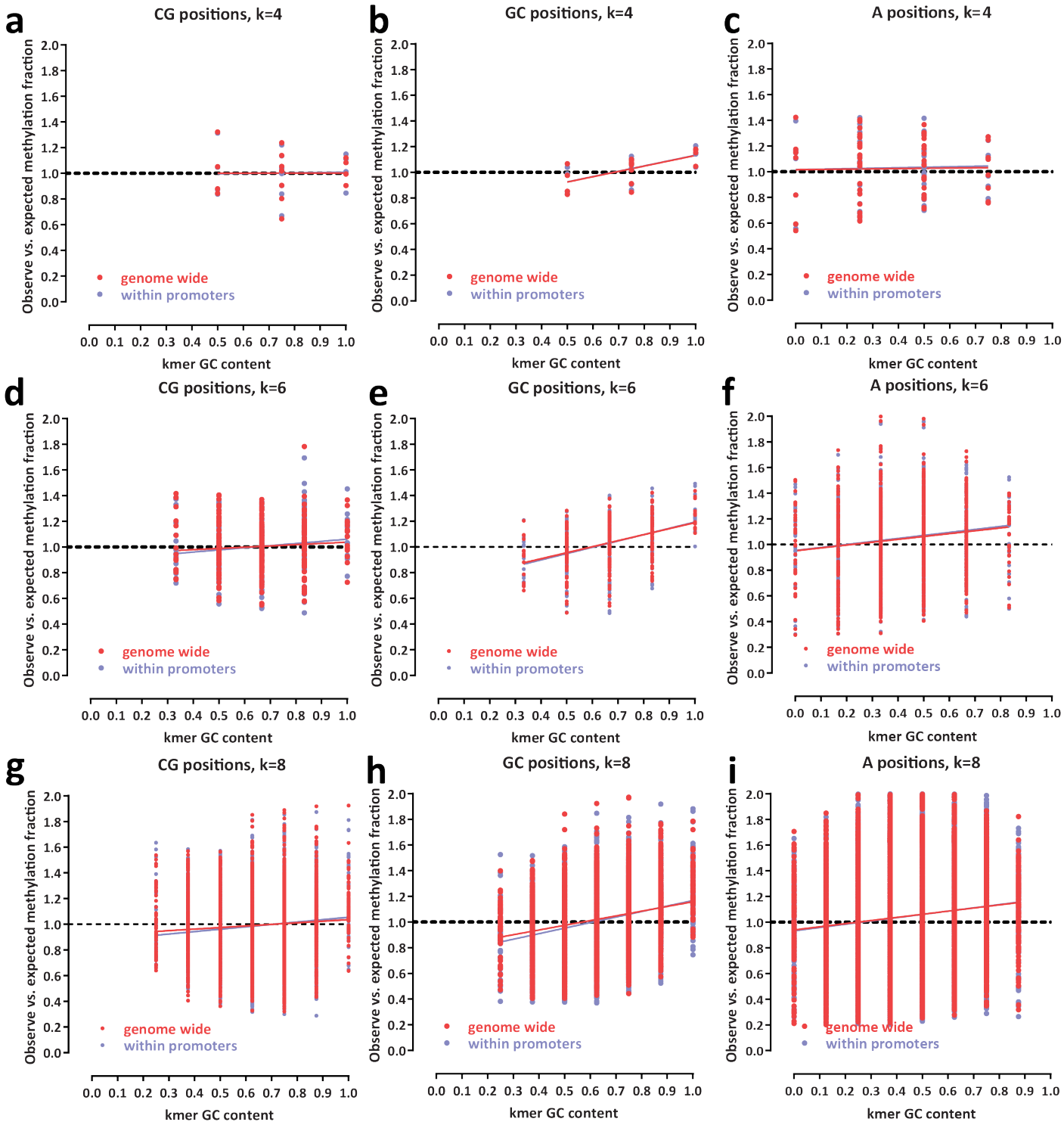

Supplementary Figure 14: Relationship between local GC content and enzymatic/methylated base calling bias. Shown is the ratio of observed versus expected fraction of methylated bases for each sequence context of size k, calculated as follows:

$$f_{\text{obs/exp},k} = \frac{k_m/k_u}{\sum_k k_m / \sum_k k_u}$$

where k_m refers to the number of bases called as methylated across all reads and k_m refers to the number of bases called as unmethylated . (a) CG positions only, $k = 4$. (b) GC positions only, $k = 4$. (c) A positions only, $k = 4$. (d) CG positions only, $k = 6$. (e) GC positions only, $k = 6$. (f) A positions only, $k = 6$. (g) CG positions only, $k = 8$. (h) GC positions only, $k = 8$. (i) A positions only, $k = 8$.

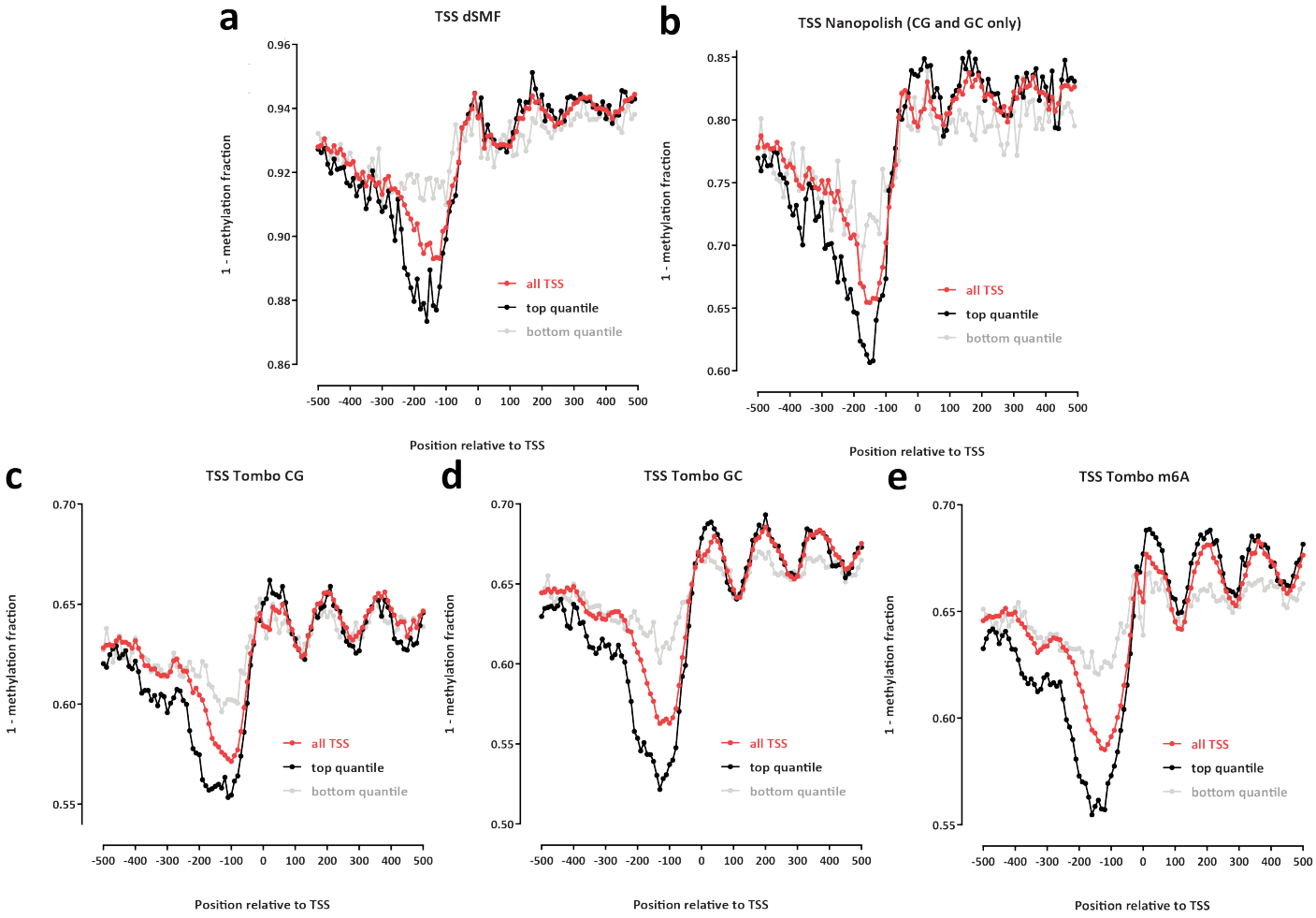

Supplementary Figure 15: Comparison of dSMF results and different approaches to methylation-aware base calling on SMAC-seq data. Shown is the inverse of the methylated fraction of nucleotides around TSSs of all, highly express (top quantile) and low expression-level (bottom quantiles) yeast genes (unfiltered "Sample 1" dataset). Note that the different panels are not drawn to the same scale. (a) dSMF; (b) SMAC-seq data using Nanopolish methylation base-calling on CG and GC nucleotides; (c) SMAC-seq data using Tombo methylation base-calling, CG positions only; (d) SMAC-seq data using Tombo methylation base-calling, GC positions only; (e) SMAC-seq data using Tombo methylation base-calling, m6A positions only.

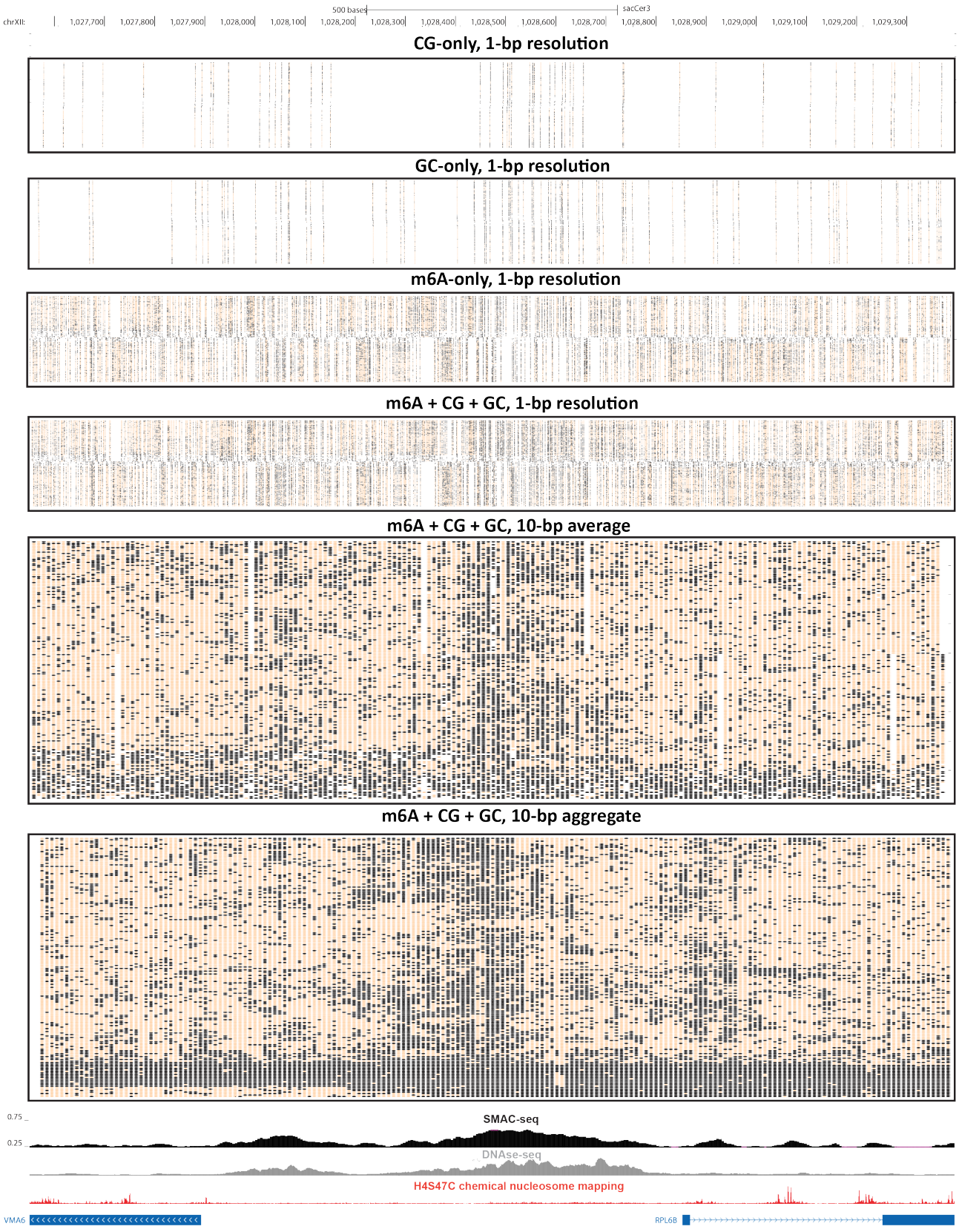

Supplementary Figure 16: Impact of the addition of m^6A on assay resolution. Shown is the raw unfiltered nanopore read coverage around a divergent promoter region on chrXII, considering only CG, only GC, only m^6A, and all bases at 1-bp resolution as well as all bases at averaged and aggregated 10-bp resolution. White spaces indicate positions for which there is no data (i.e. no CG, GC or A).

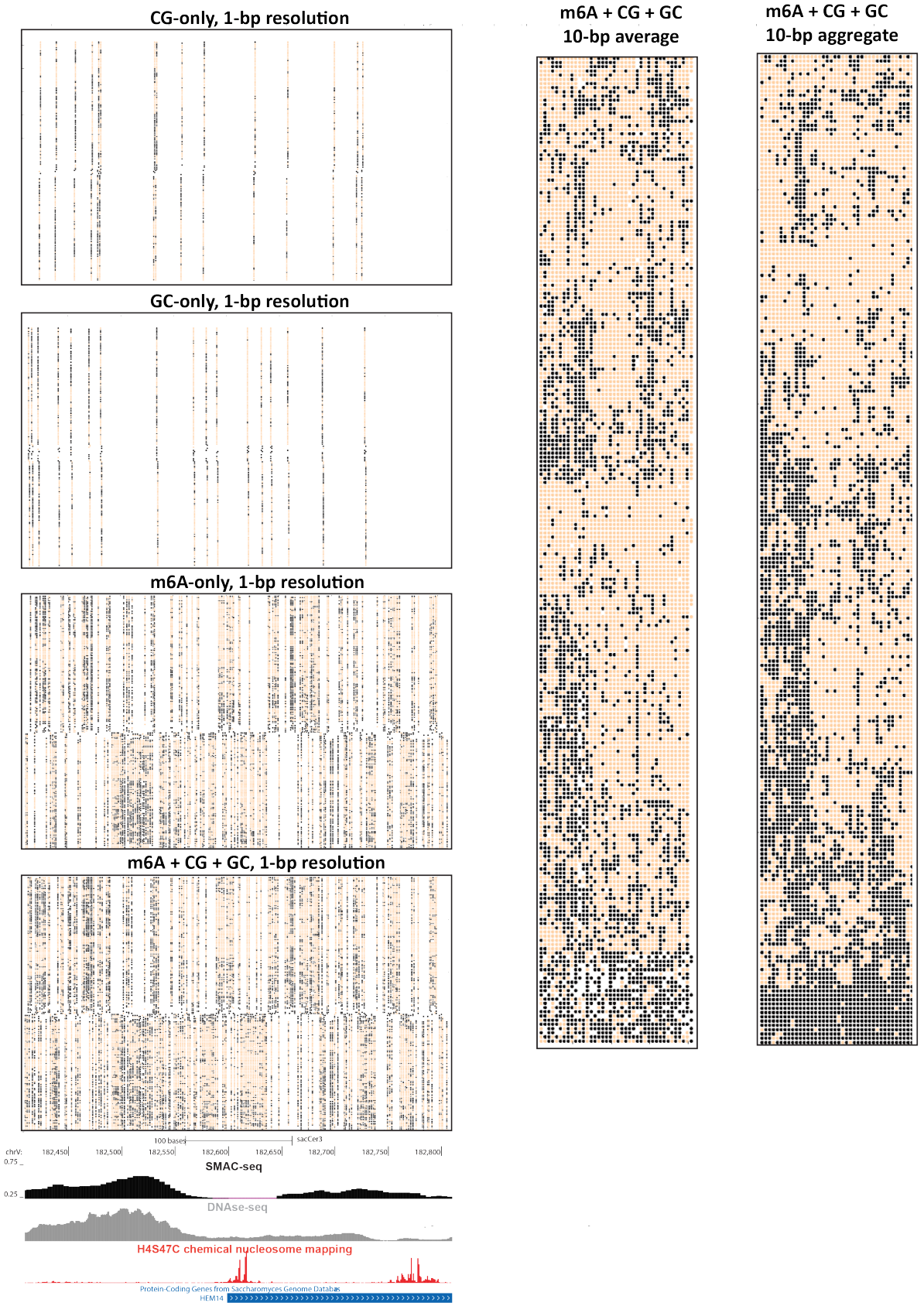

Supplementary Figure 17: Impact of the addition of m^{6}A on assay resolution. Shown is the raw unfiltered nanopore read coverage around a strongly positioned +1 nucleosome, considering only CG, only GC, only m^{6}A, and all bases at 1-bp resolution as well as all bases at averaged and aggregated 10-bp resolution. White spaces indicate positions for which there is no data (i.e. no CG, GC or A).

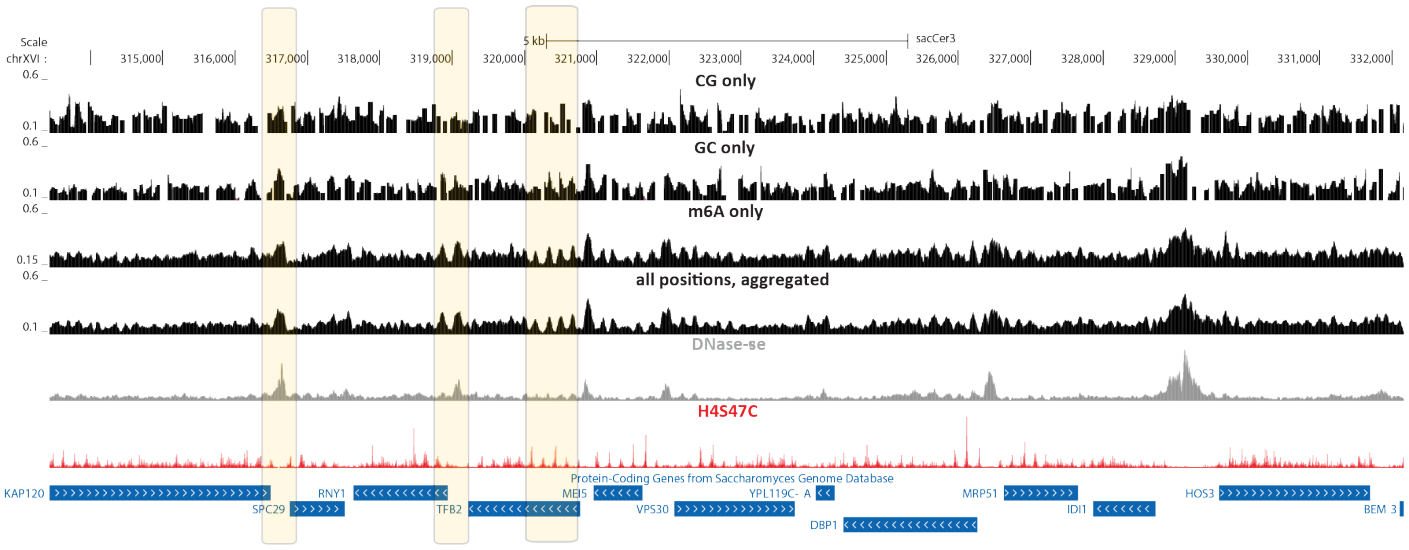

Supplementary Figure 18: Impact of the addition of m^{6}A on assay resolution. Shown is the average accessibility status measured by CG, GC or m^{6}A modifications alone and with all positions aggregated together (calculated over 50bp windows, with a step size of 5, as in Figure 1). The sparseness of CG and GC dinucleotides in the genome results in numerous positions where data is completely missing and to low resolution not allowing the identification of numerous positioned nucleosomes and even entire accessibility peaks.

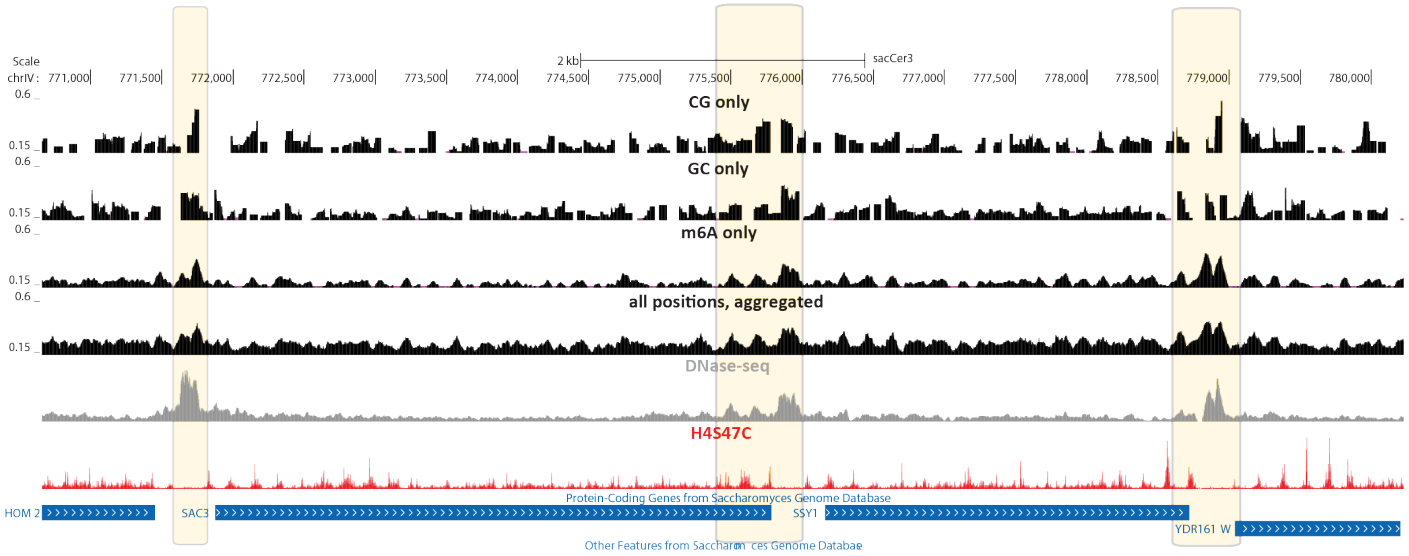

Supplementary Figure 19: Impact of the addition of m^{6}A on assay resolution. Shown is the average accessibility status measured by CG, GC or m^{6}A modifications alone and with all positions aggregated together (calculated over 50bp windows, with a step size of 5, as in Figure 1). The sparseness of CG and GC dinucleotides in the genome results in numerous positions where data is completely missing and to low resolution not allowing the identification of numerous positioned nucleosomes and even entire accessibility peaks.

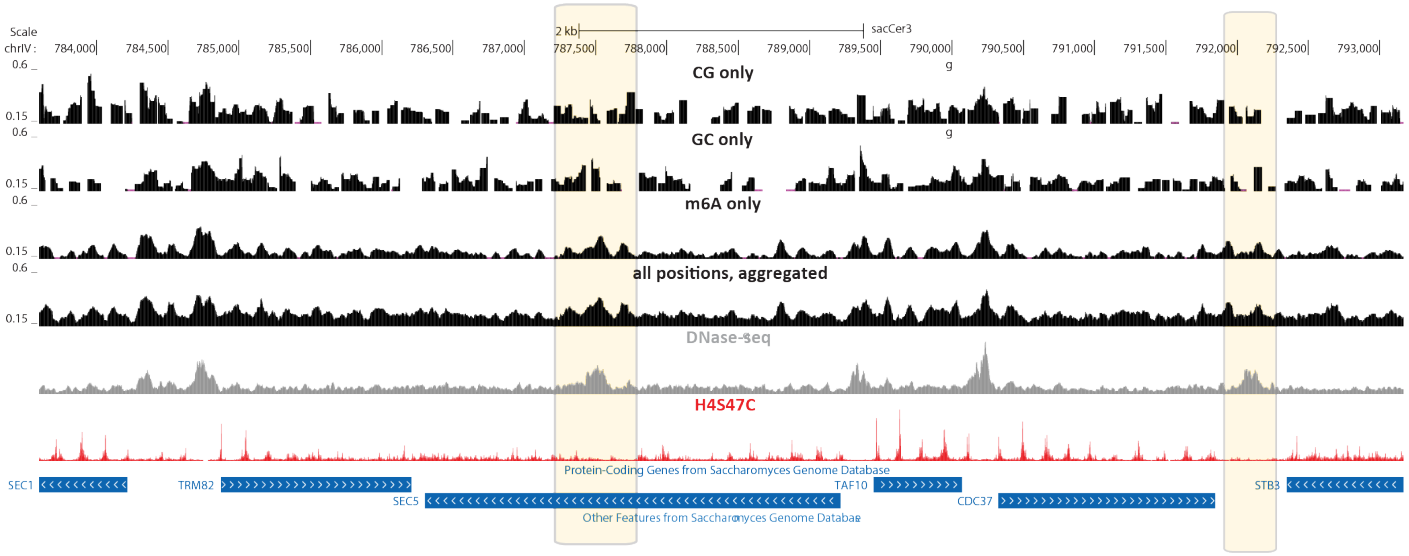

Supplementary Figure 20: Impact of the addition of m^{6}A on assay resolution. Shown is the average accessibility status measured by CG, GC or m^{6}A modifications alone and with all positions aggregated together (calculated over 50bp windows, with a step size of 5, as in Figure 1). The sparseness of CG and GC dinucleotides in the genome results in numerous positions where data is completely missing and to low resolution not allowing the identification of numerous positioned nucleosomes and even entire accessibility peaks.

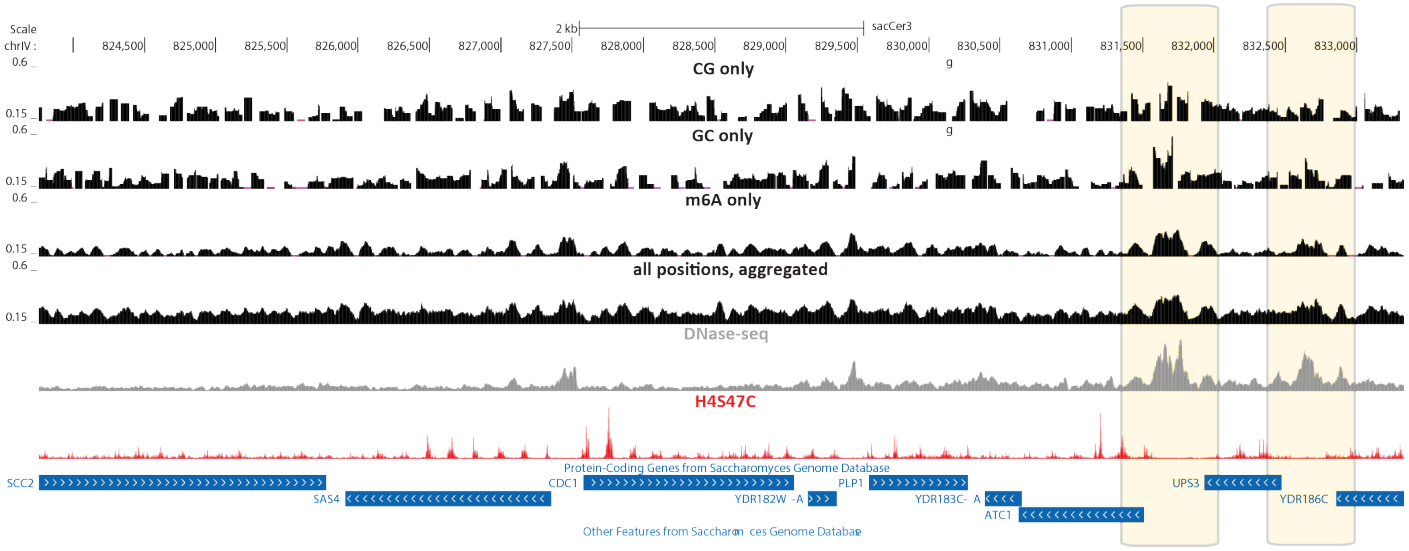

Supplementary Figure 21: Impact of the addition of m^{6}A on assay resolution. Shown is the average accessibility status measured by CG, GC or m^{6}A modifications alone and with all positions aggregated together (calculated over 50bp windows, with a step size of 5, as in Figure 1). The sparseness of CG and GC dinucleotides in the genome results in numerous positions where data is completely missing and to low resolution not allowing the identification of numerous positioned nucleosomes and even entire accessibility peaks.

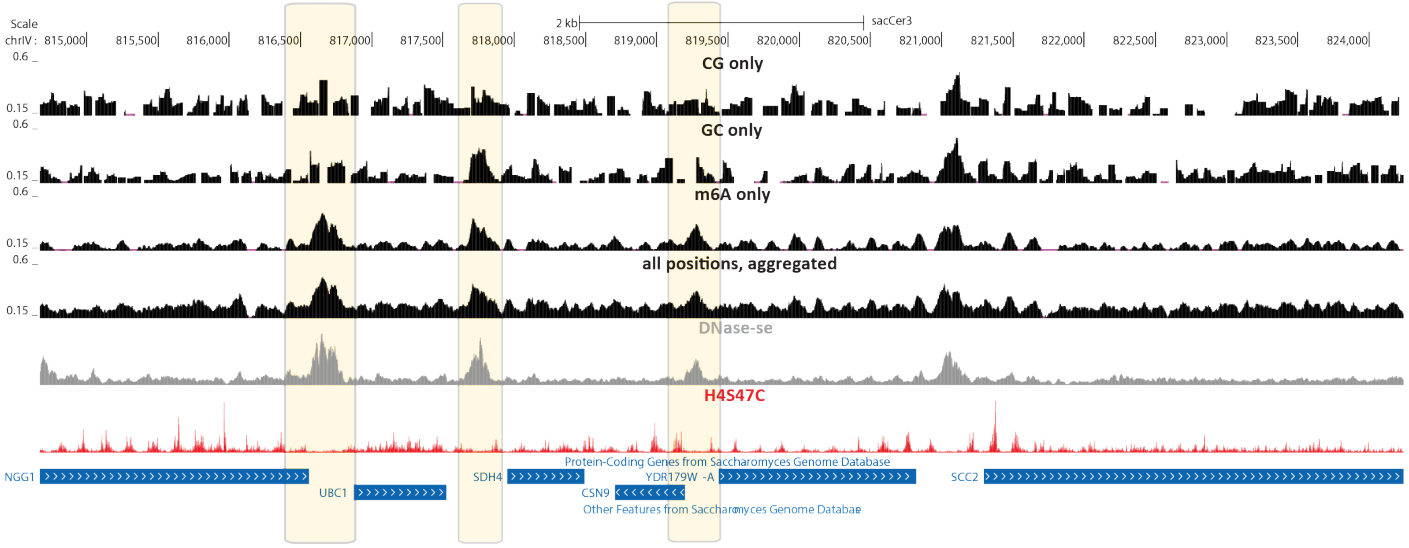

Supplementary Figure 22: Impact of the addition of m^{6}A on assay resolution. Shown is the average accessibility status measured by CG, GC or m^{6}A modifications alone and with all positions aggregated together (calculated over 50bp windows, with a step size of 5, as in Figure 1). The sparseness of CG and GC dinucleotides in the genome results in numerous positions where data is completely missing and to low resolution not allowing the identification of numerous positioned nucleosomes and even entire accessibility peaks.

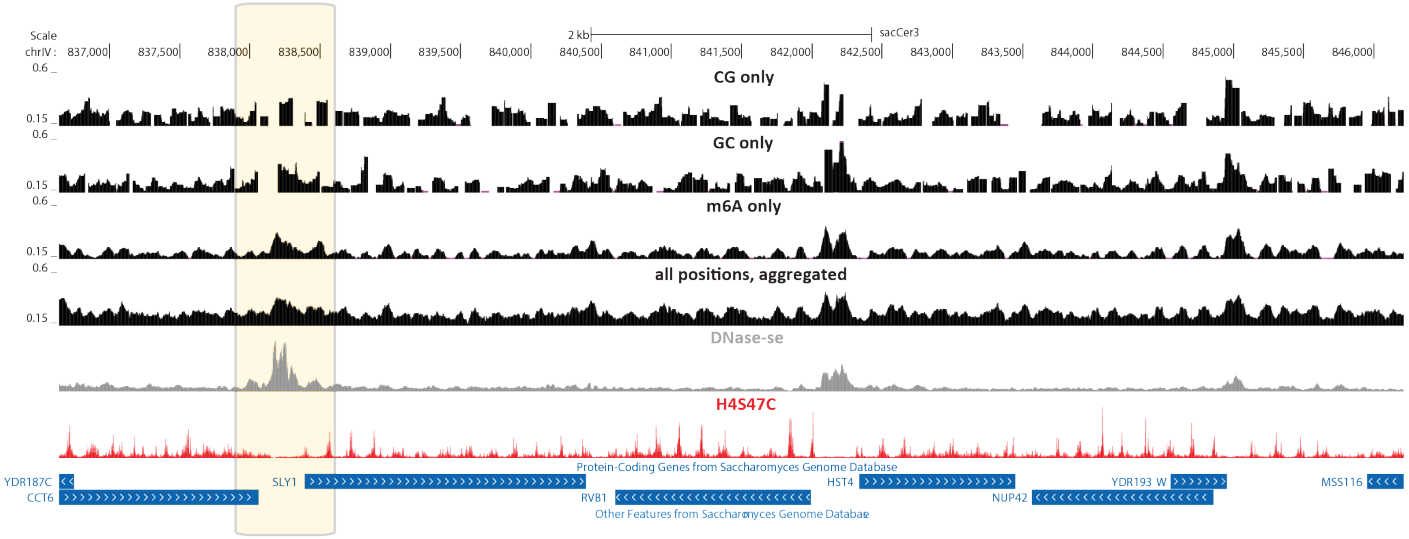

Supplementary Figure 23: Impact of the addition of m^{6}A on assay resolution. Shown is the average accessibility status measured by CG, GC or m^{6}A modifications alone and with all positions aggregated together (calculated over 50bp windows, with a step size of 5, as in Figure 1). The sparseness of CG and GC dinucleotides in the genome results in numerous positions where data is completely missing and to low resolution not allowing the identification of numerous positioned nucleosomes and even entire accessibility peaks.

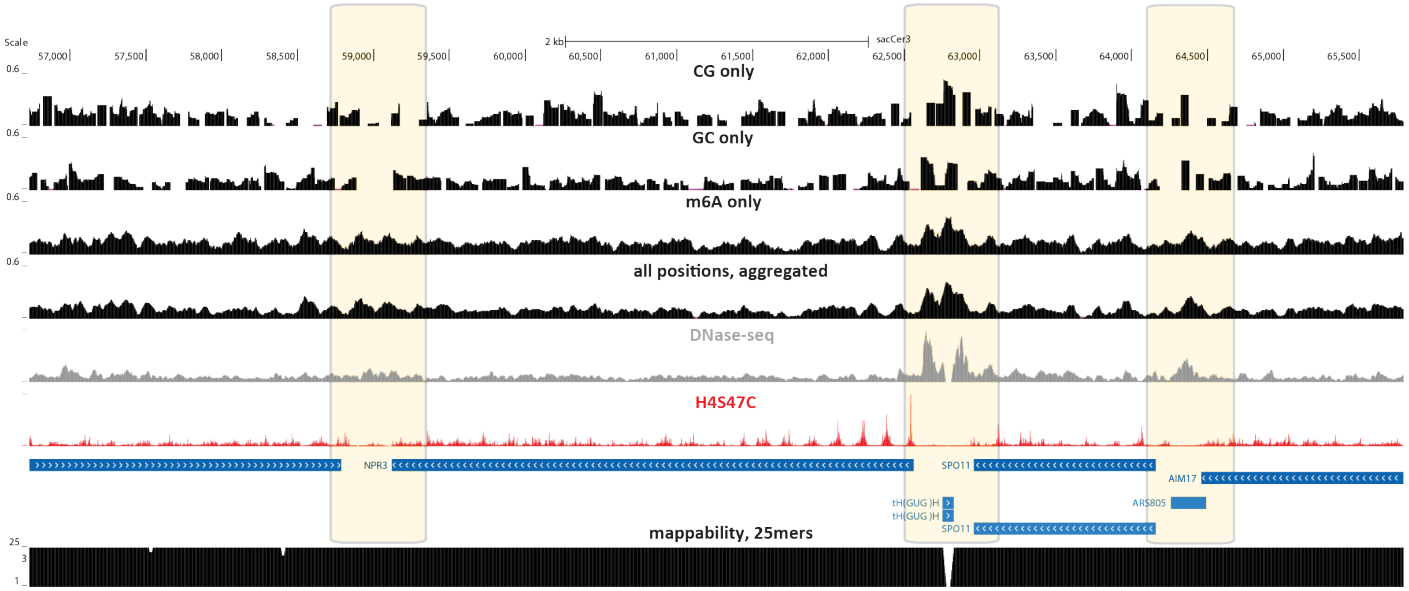

Supplementary Figure 24: Impact of the addition of m^6A on assay resolution. Shown is the average accessibility status measured by CG, GC or m^6A modifications alone and with all positions aggregated together (calculated over 50bp windows, with a step size of 5, as in Figure 1). The sparseness of CG and GC dinucleotides in the genome results in numerous positions where data is completely missing and to low resolution not allowing the identification of numerous positioned nucleosomes and even entire accessibility peaks.

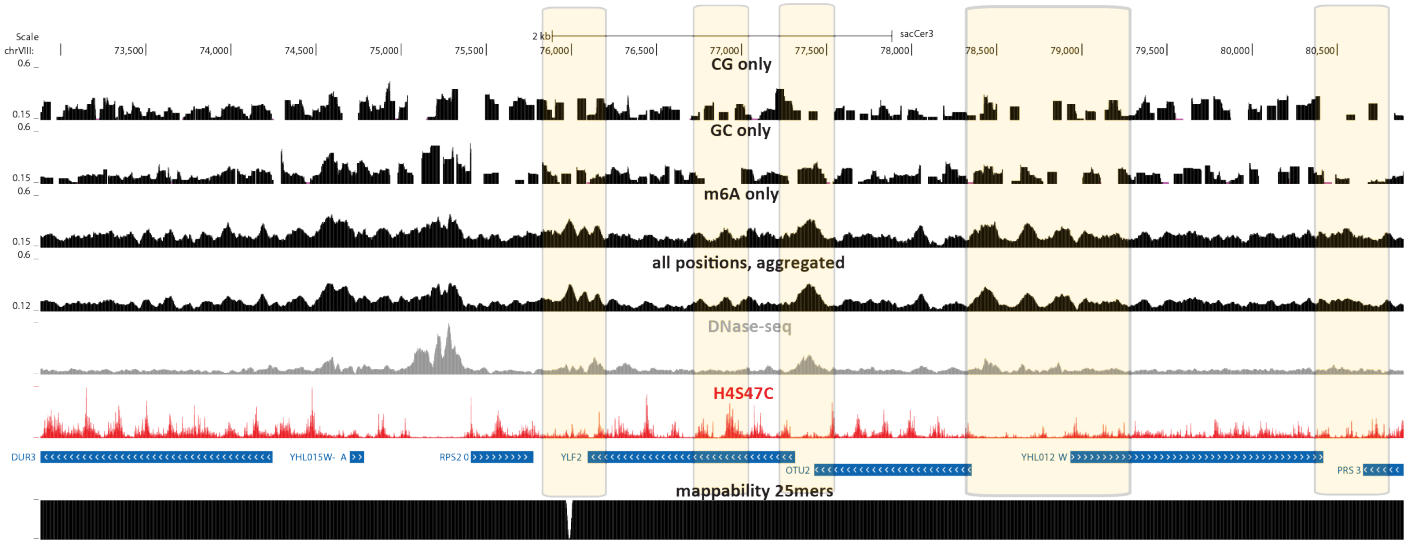

Supplementary Figure 25: Impact of the addition of m^6A on assay resolution. Shown is the average accessibility status measured by CG, GC or m^6A modifications alone and with all positions aggregated together (calculated over 50bp windows, with a step size of 5, as in Figure 1). The sparseness of CG and GC dinucleotides in the genome results in numerous positions where data is completely missing and to low resolution not allowing the identification of numerous positioned nucleosomes and even entire accessibility peaks.

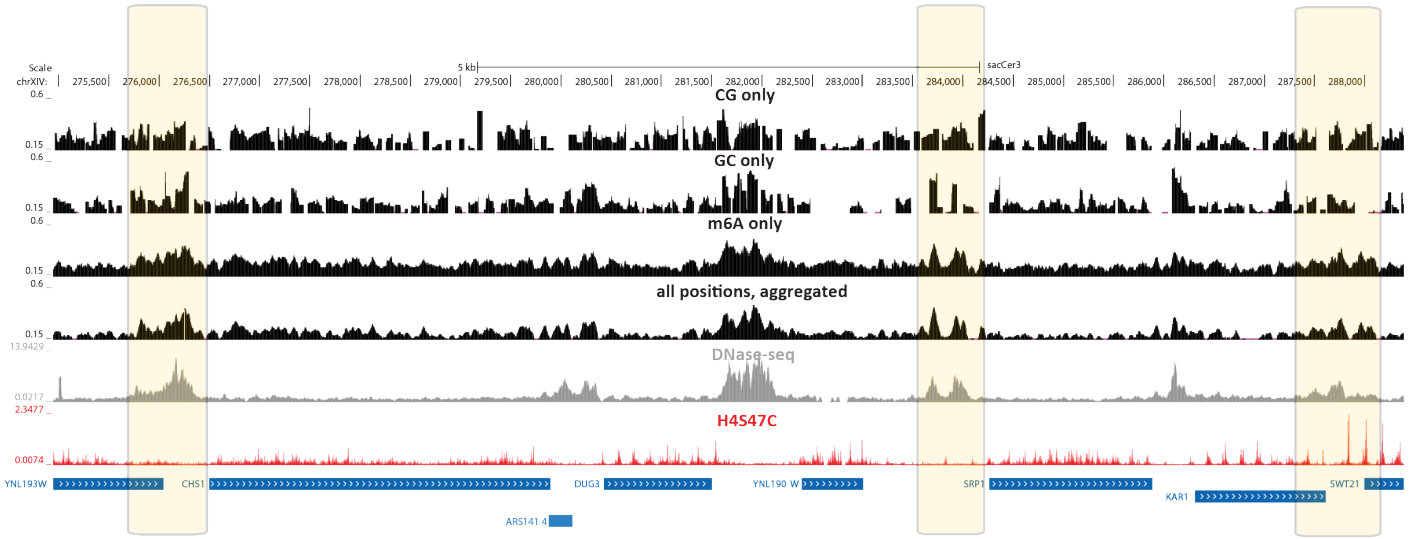

Supplementary Figure 26: Impact of the addition of m^{6}A on assay resolution. Shown is the average accessibility status measured by CG, GC or m^{6}A modifications alone and with all positions aggregated together (calculated over 50bp windows, with a step size of 5, as in Figure 1). The sparseness of CG and GC dinucleotides in the genome results in numerous positions where data is completely missing and to low resolution not allowing the identification of numerous positioned nucleosomes and even entire accessibility peaks.

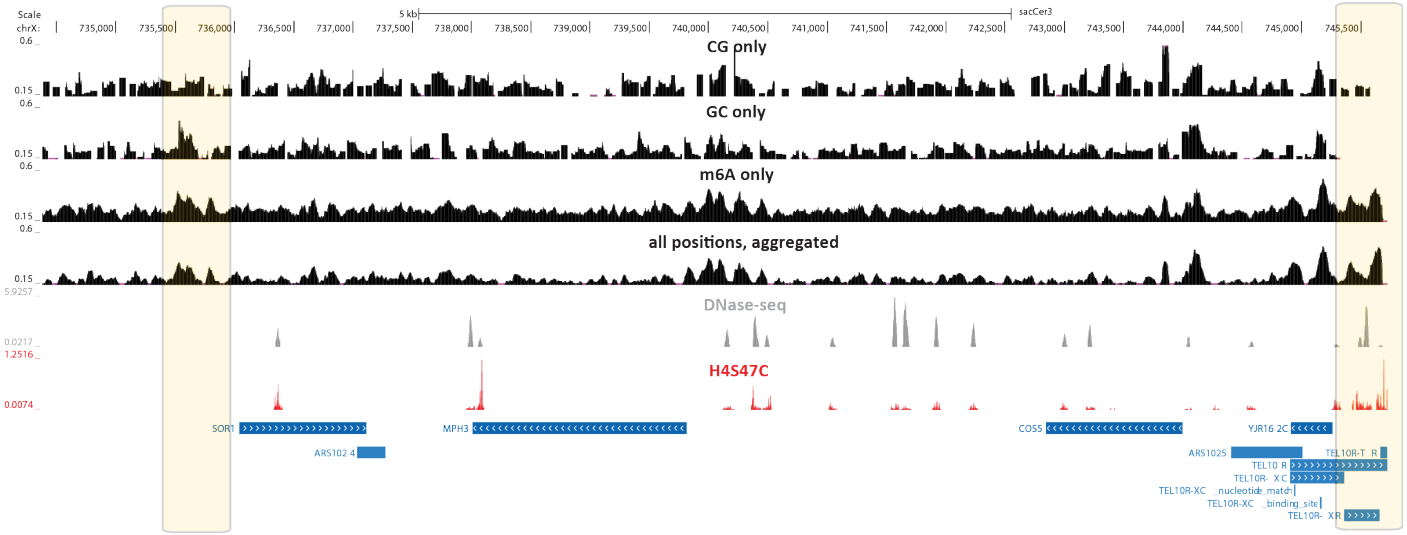

Supplementary Figure 27: Impact of the addition of m^{6}A on assay resolution. Shown is the average accessibility status measured by CG, GC or m^{6}A modifications alone and with all positions aggregated together (calculated over 50bp windows, with a step size of 5, as in Figure 1). The sparseness of CG and GC dinucleotides in the genome results in numerous positions where data is completely missing and to low resolution not allowing the identification of numerous positioned nucleosomes and even entire accessibility peaks.

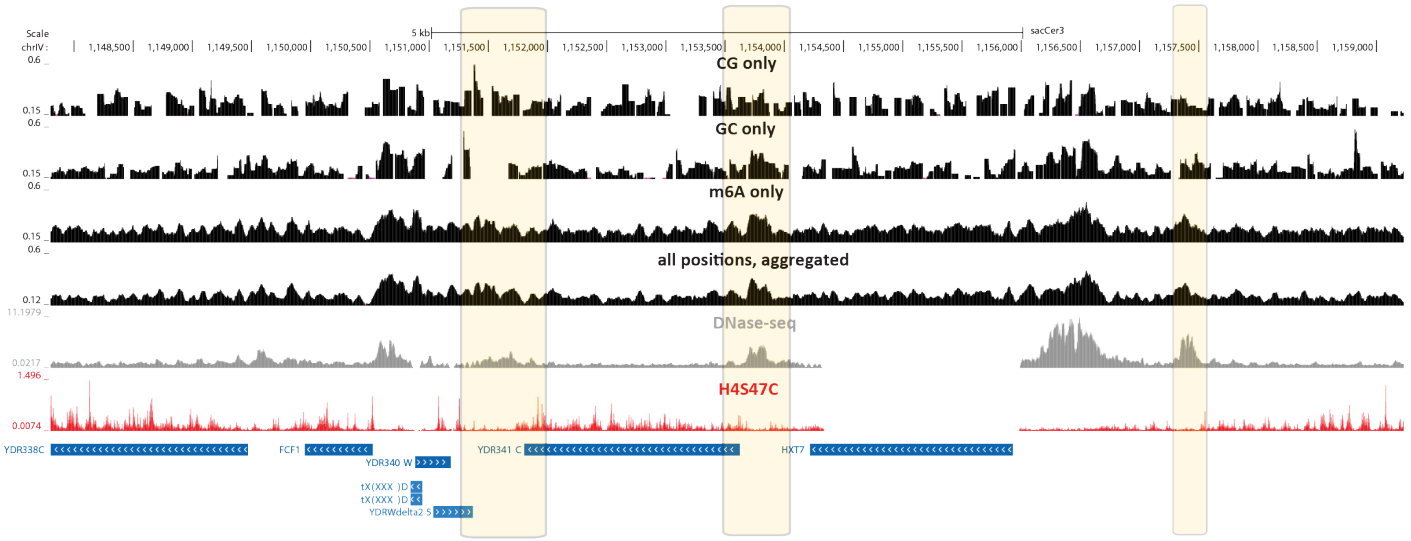

Supplementary Figure 28: Impact of the addition of m^{6}A on assay resolution. Shown is the average accessibility status measured by CG, GC or m^{6}A modifications alone and with all positions aggregated together (calculated over 50bp windows, with a step size of 5, as in Figure 1). The sparseness of CG and GC dinucleotides in the genome results in numerous positions where data is completely missing and to low resolution not allowing the identification of numerous positioned nucleosomes and even entire accessibility peaks.

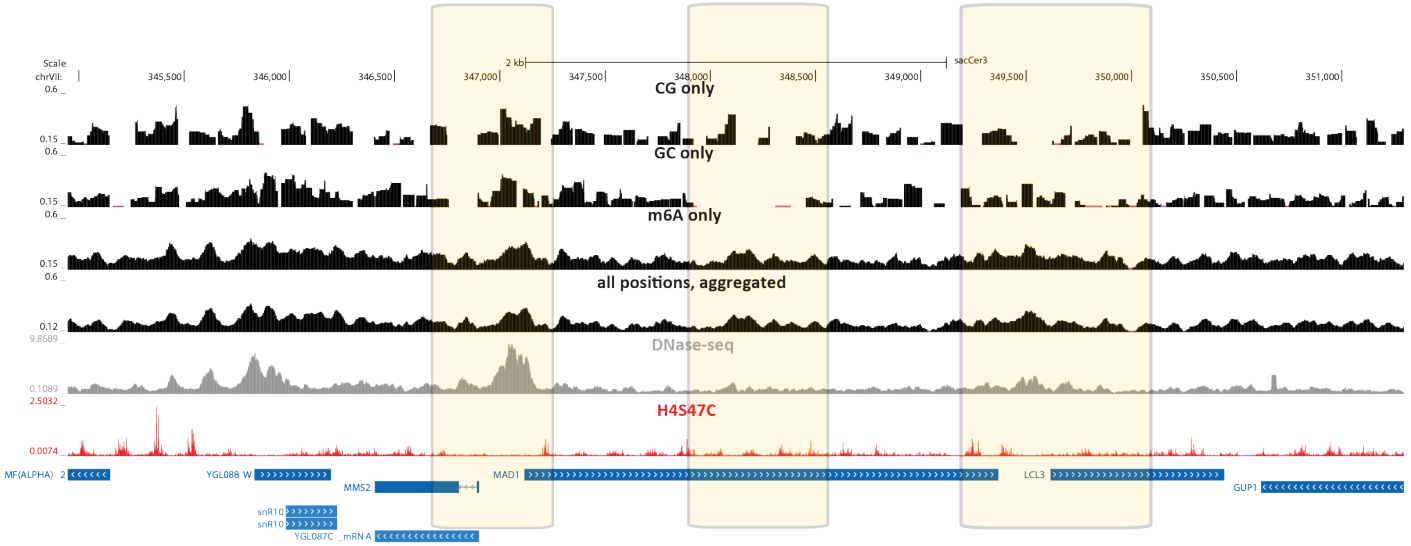

Supplementary Figure 29: Impact of the addition of m^{6}A on assay resolution. Shown is the average accessibility status measured by CG, GC or m^{6}A modifications alone and with all positions aggregated together (calculated over 50bp windows, with a step size of 5, as in Figure 1). The sparseness of CG and GC dinucleotides in the genome results in numerous positions where data is completely missing and to low resolution not allowing the identification of numerous positioned nucleosomes and even entire accessibility peaks.

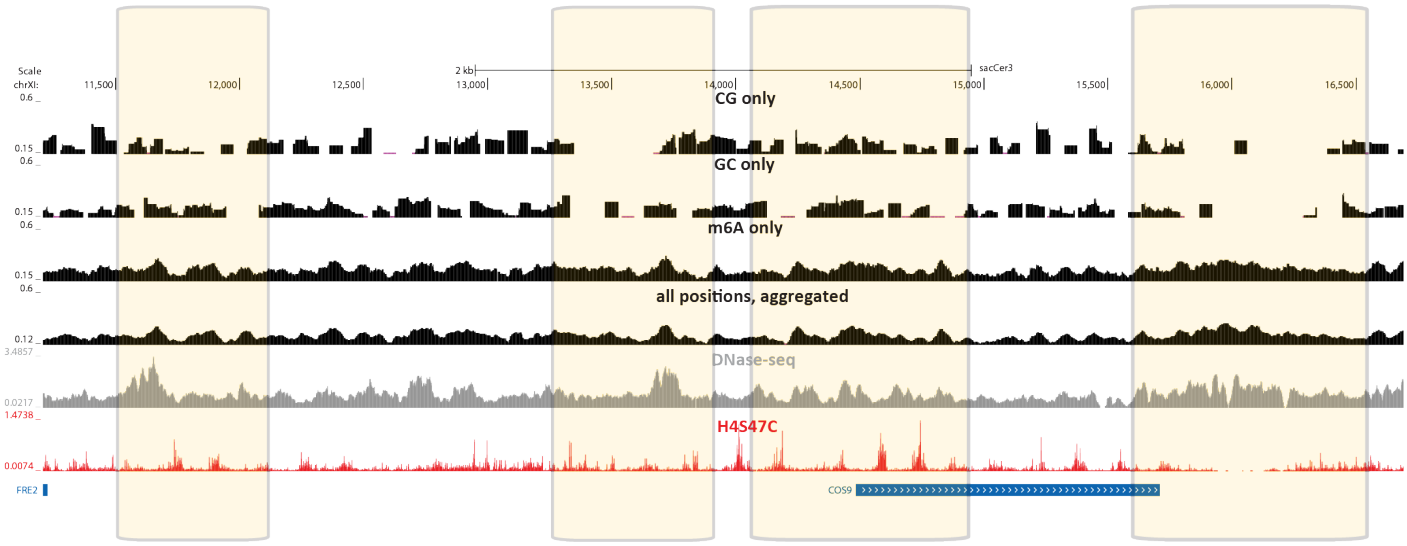

Supplementary Figure 30: Impact of the addition of m^{6}A on assay resolution. Shown is the average accessibility status measured by CG, GC or m^{6}A modifications alone and with all positions aggregated together (calculated over 50bp windows, with a step size of 5, as in Figure 1). The sparseness of CG and GC dinucleotides in the genome results in numerous positions where data is completely missing and to low resolution not allowing the identification of numerous positioned nucleosomes and even entire accessibility peaks.

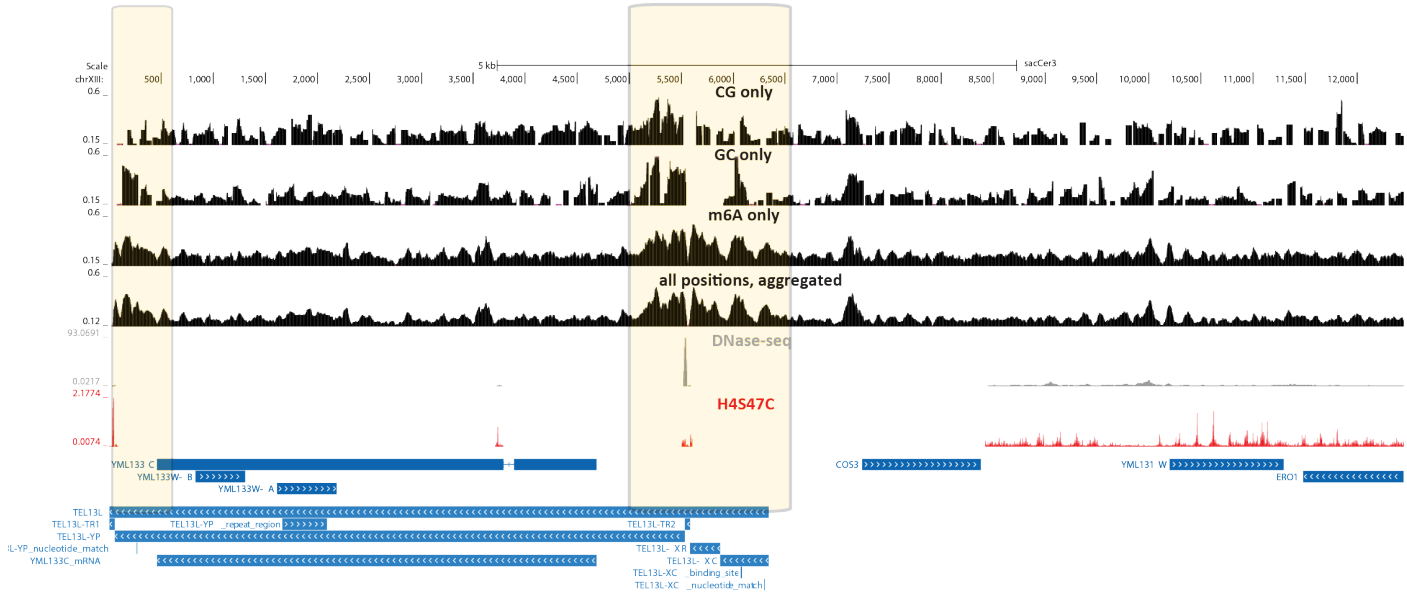

Supplementary Figure 31: Impact of the addition of m^{6}A on assay resolution. Shown is the average accessibility status measured by CG, GC or m^{6}A modifications alone and with all positions aggregated together (calculated over 50bp windows, with a step size of 5, as in Figure 1). The sparseness of CG and GC dinucleotides in the genome results in numerous positions where data is completely missing and to low resolution not allowing the identification of numerous positioned nucleosomes and even entire accessibility peaks.

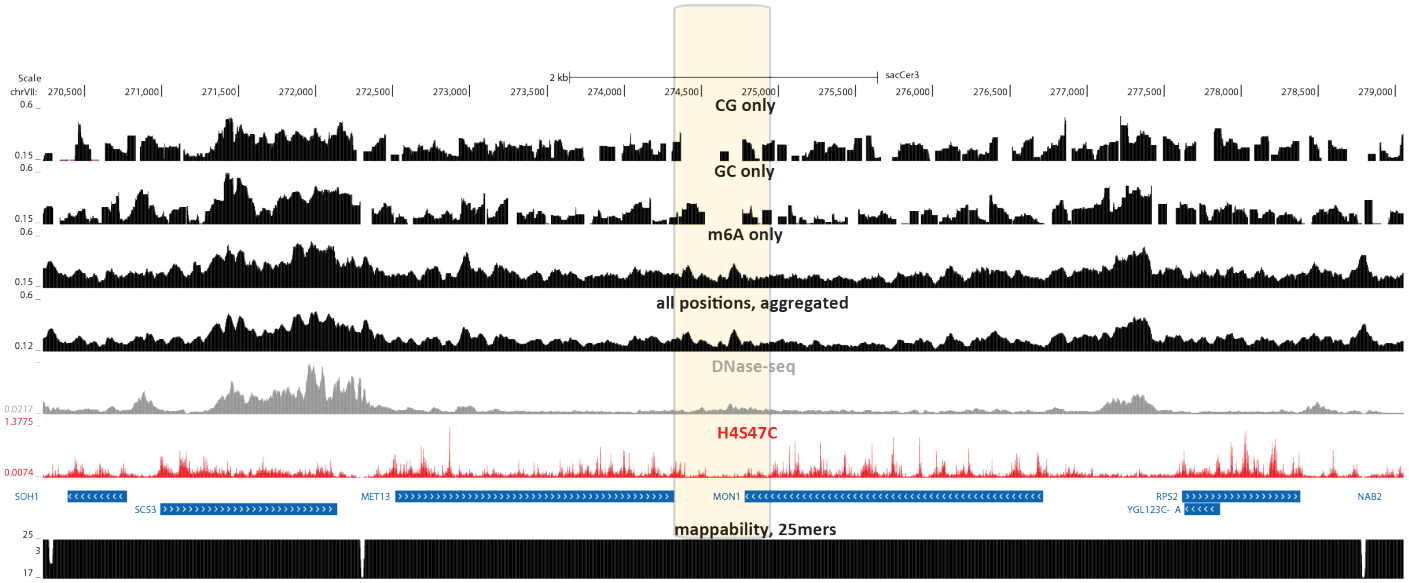

Supplementary Figure 32: Impact of the addition of m^{6}A on assay resolution. Shown is the average accessibility status measured by CG, GC or m^{6}A modifications alone and with all positions aggregated together (calculated over 50bp windows, with a step size of 5, as in Figure 1). The sparseness of CG and GC dinucleotides in the genome results in numerous positions where data is completely missing and to low resolution not allowing the identification of numerous positioned nucleosomes and even entire accessibility peaks.

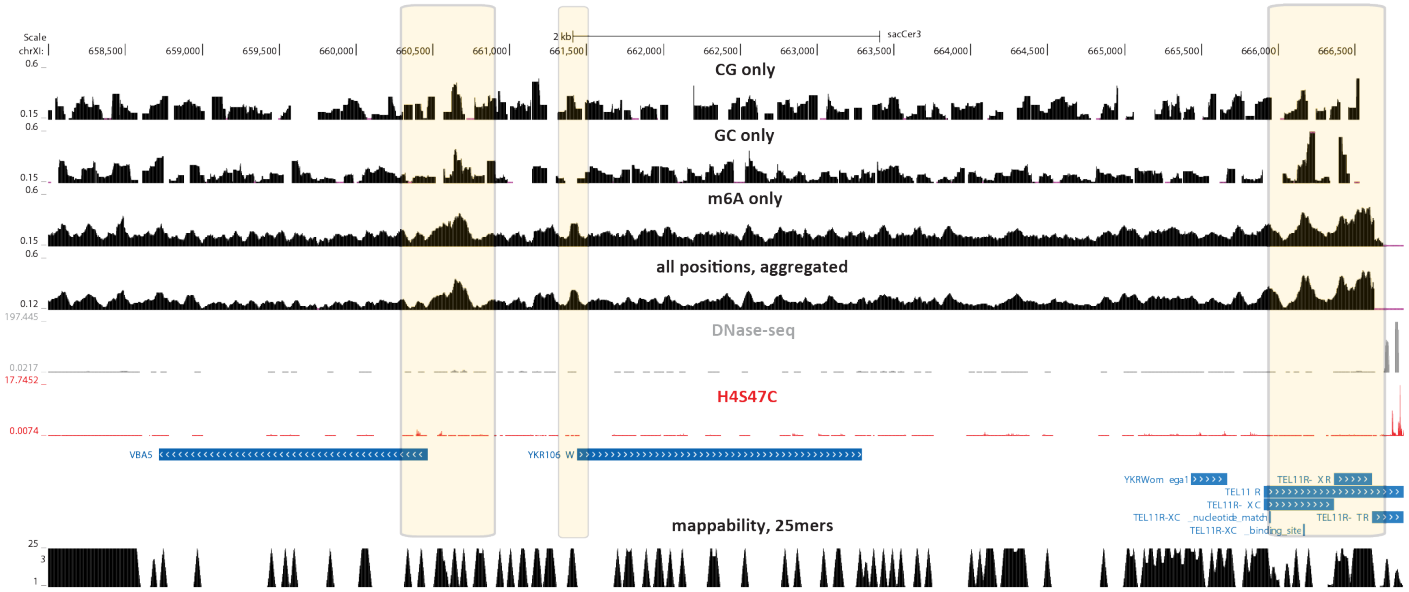

Supplementary Figure 33: Impact of the addition of m^{6}A on assay resolution. Shown is the average accessibility status measured by CG, GC or m^{6}A modifications alone and with all positions aggregated together (calculated over 50bp windows, with a step size of 5, as in Figure 1). The sparseness of CG and GC dinucleotides in the genome results in numerous positions where data is completely missing and to low resolution not allowing the identification of numerous positioned nucleosomes and even entire accessibility peaks.

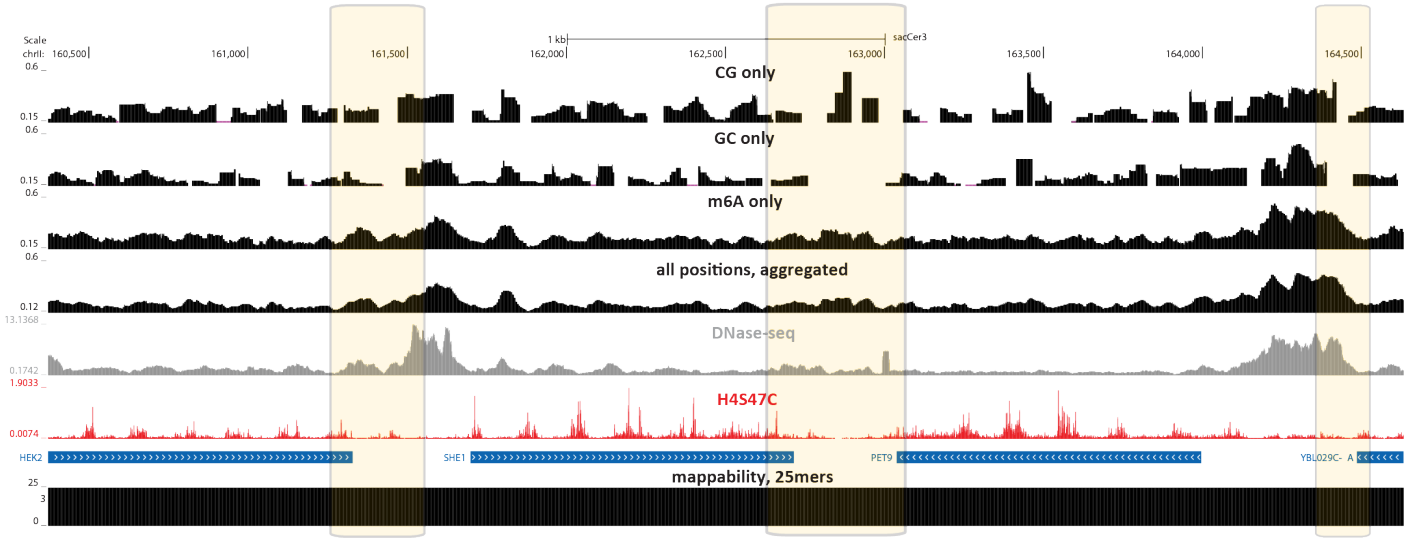

Supplementary Figure 34: Impact of the addition of m^{6}A on assay resolution. Shown is the average accessibility status measured by CG, GC or m^{6}A modifications alone and with all positions aggregated together (calculated over 50bp windows, with a step size of 5, as in Figure 1). The sparseness of CG and GC dinucleotides in the genome results in numerous positions where data is completely missing and to low resolution not allowing the identification of numerous positioned nucleosomes and even entire accessibility peaks.

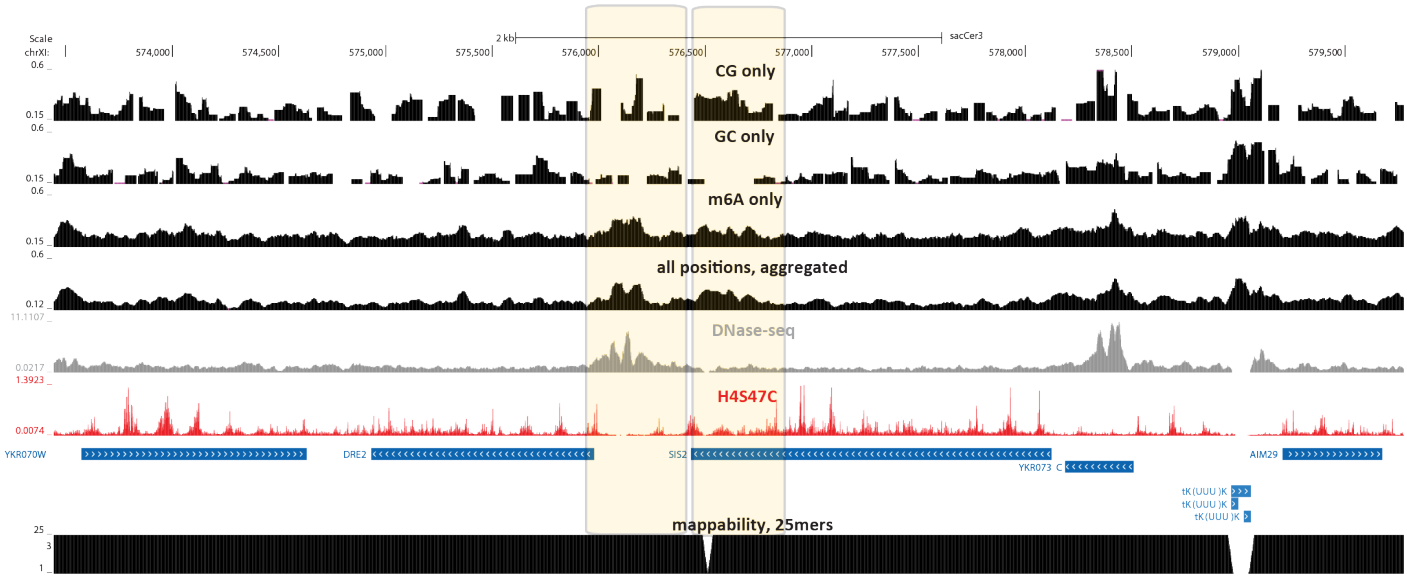

Supplementary Figure 35: Impact of the addition of m^{6}A on assay resolution. Shown is the average accessibility status measured by CG, GC or m^{6}A modifications alone and with all positions aggregated together (calculated over 50bp windows, with a step size of 5, as in Figure 1). The sparseness of CG and GC dinucleotides in the genome results in numerous positions where data is completely missing and to low resolution not allowing the identification of numerous positioned nucleosomes and even entire accessibility peaks.

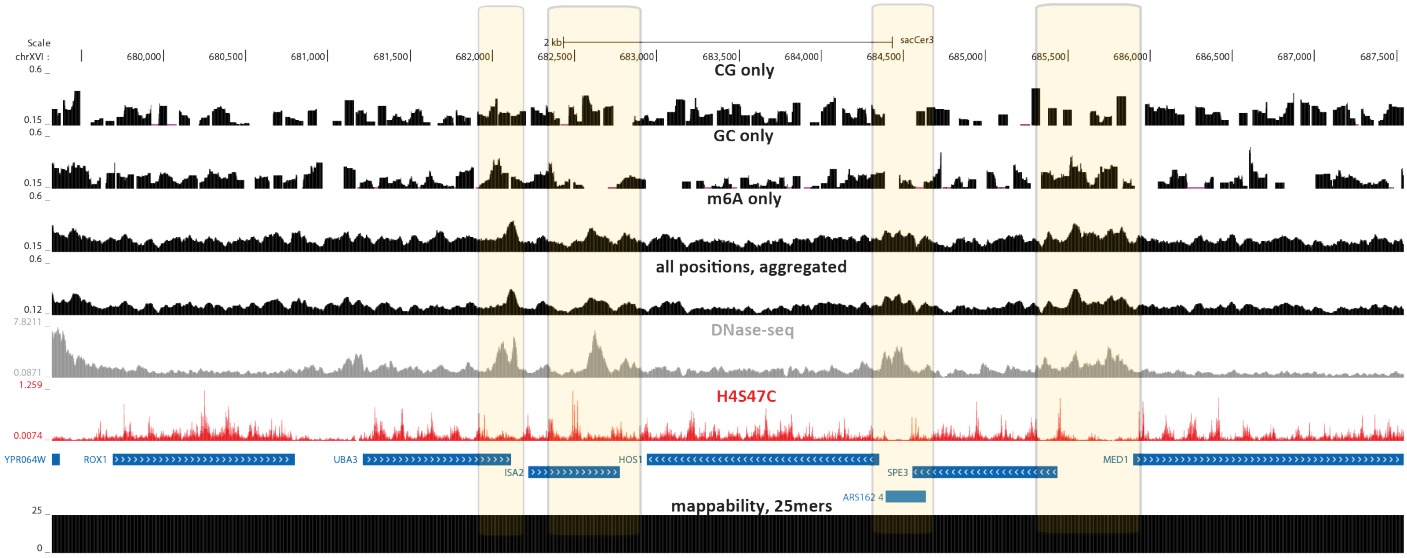

Supplementary Figure 36: Impact of the addition of m^{6}A on assay resolution. Shown is the average accessibility status measured by CG, GC or m^{6}A modifications alone and with all positions aggregated together (calculated over 50bp windows, with a step size of 5, as in Figure 1). The sparseness of CG and GC dinucleotides in the genome results in numerous positions where data is completely missing and to low resolution not allowing the identification of numerous positioned nucleosomes and even entire accessibility peaks.

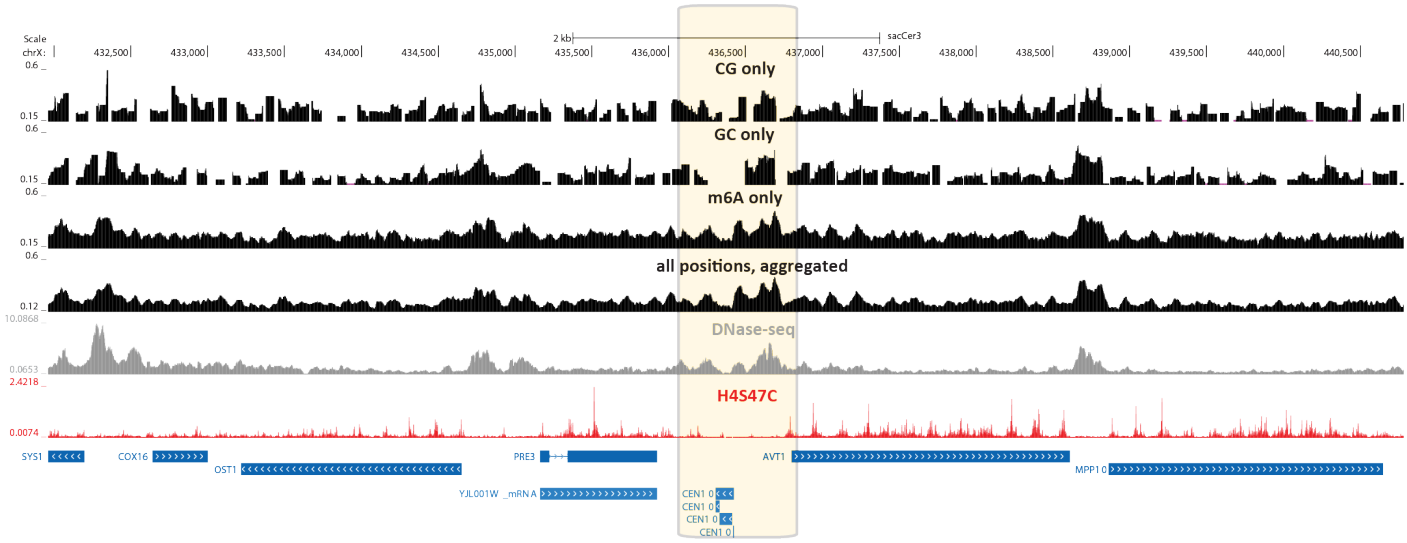

Supplementary Figure 37: Impact of the addition of m^{6}A on assay resolution. Shown is the average accessibility status measured by CG, GC or m^{6}A modifications alone and with all positions aggregated together (calculated over 50bp windows, with a step size of 5, as in Figure 1). The sparseness of CG and GC dinucleotides in the genome results in numerous positions where data is completely missing and to low resolution not allowing the identification of numerous positioned nucleosomes and even entire accessibility peaks.

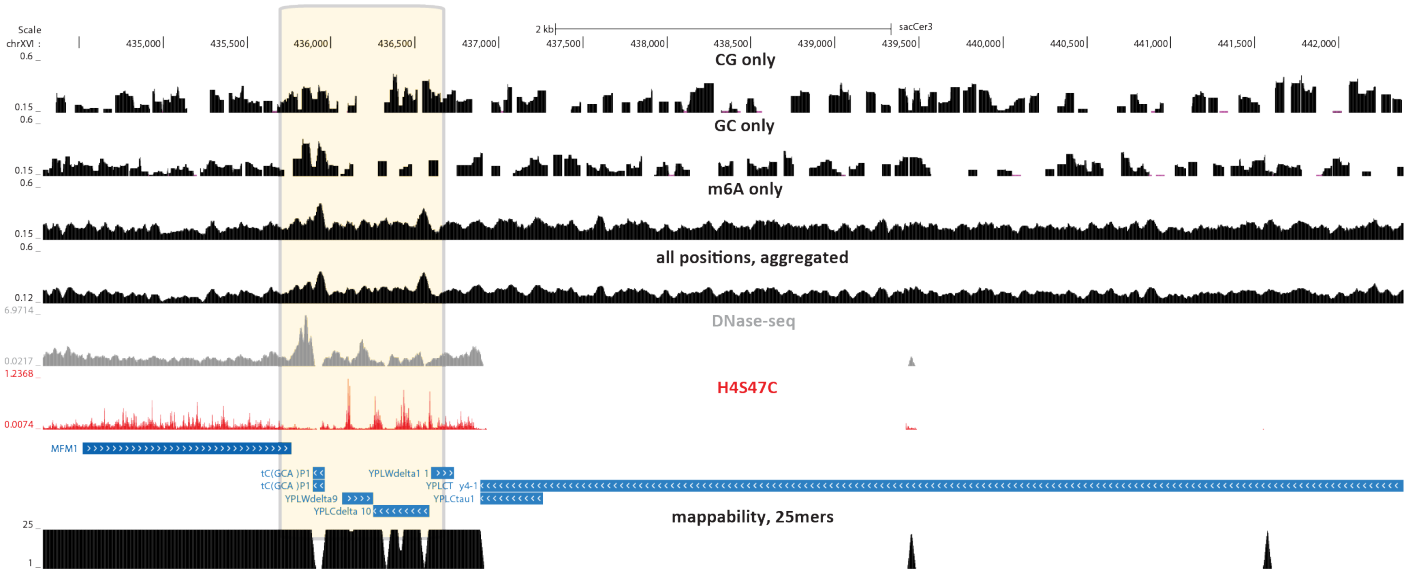

Supplementary Figure 38: Impact of the addition of m^{6}A on assay resolution. Shown is the average accessibility status measured by CG, GC or m^{6}A modifications alone and with all positions aggregated together (calculated over 50bp windows, with a step size of 5, as in Figure 1). The sparseness of CG and GC dinucleotides in the genome results in numerous positions where data is completely missing and to low resolution not allowing the identification of numerous positioned nucleosomes and even entire accessibility peaks.

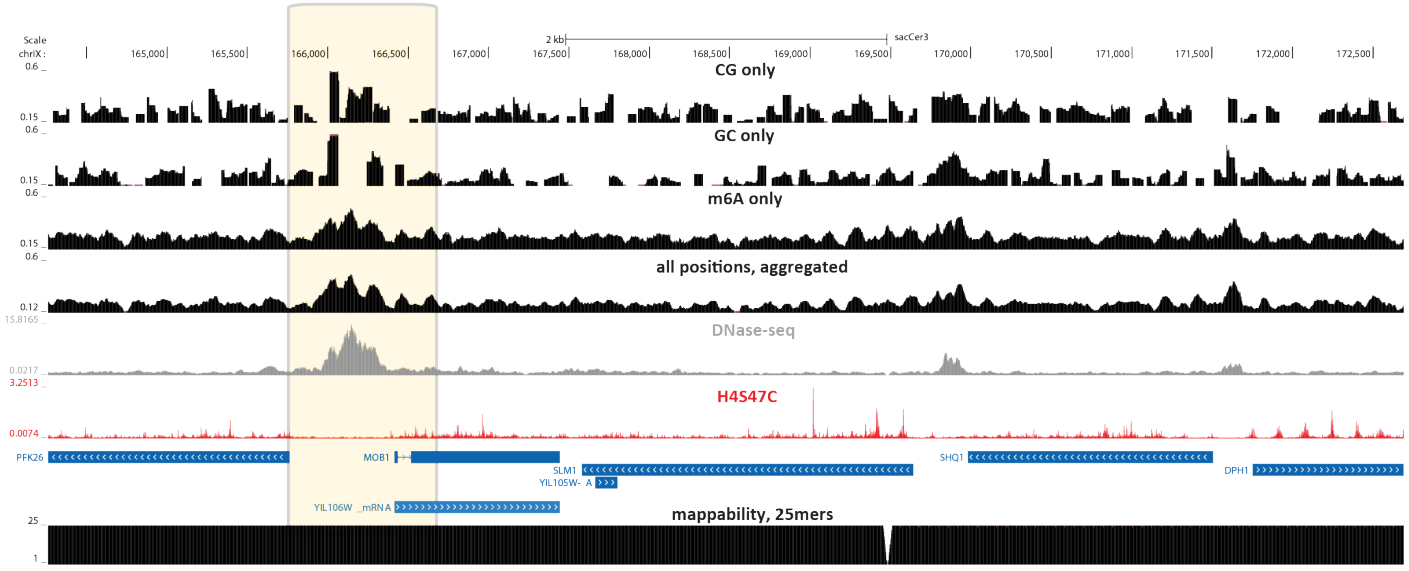

Supplementary Figure 39: Impact of the addition of m^{6}A on assay resolution. Shown is the average accessibility status measured by CG, GC or m^{6}A modifications alone and with all positions aggregated together (calculated over 50bp windows, with a step size of 5, as in Figure 1). The sparseness of CG and GC dinucleotides in the genome results in numerous positions where data is completely missing and to low resolution not allowing the identification of numerous positioned nucleosomes and even entire accessibility peaks.

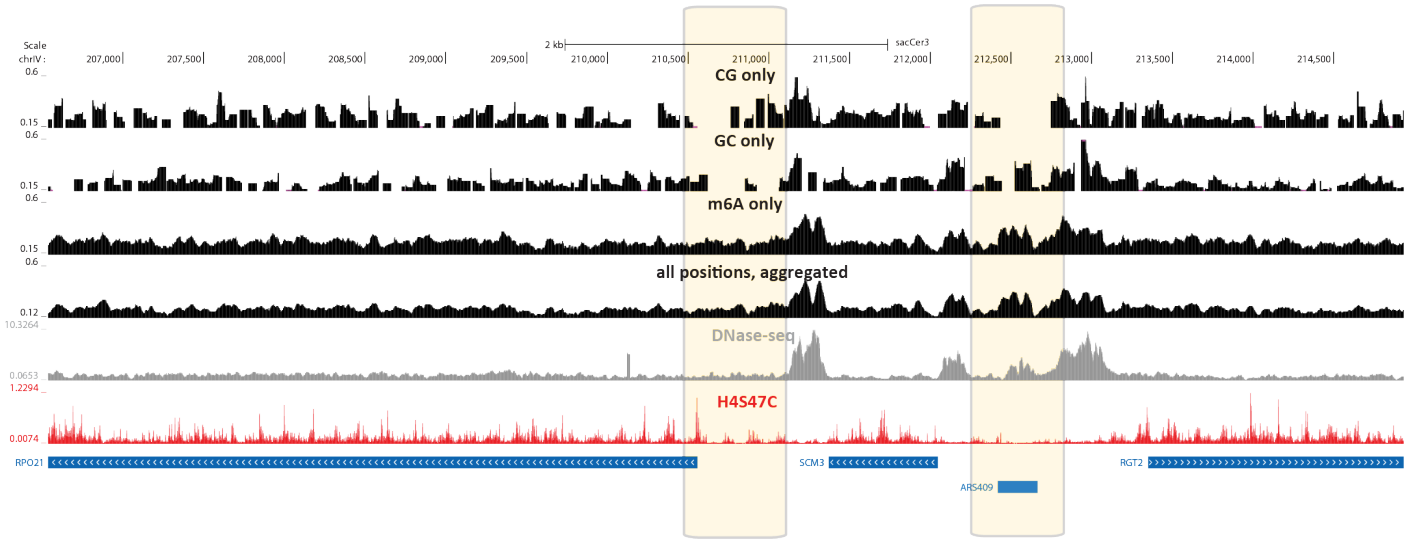

Supplementary Figure 40: Impact of the addition of m^6A on assay resolution. Shown is the average accessibility status measured by CG, GC or m^6A modifications alone and with all positions aggregated together (calculated over 50bp windows, with a step size of 5, as in Figure 1). The sparseness of CG and GC dinucleotides in the genome results in numerous positions where data is completely missing and to low resolution not allowing the identification of numerous positioned nucleosomes and even entire accessibility peaks.

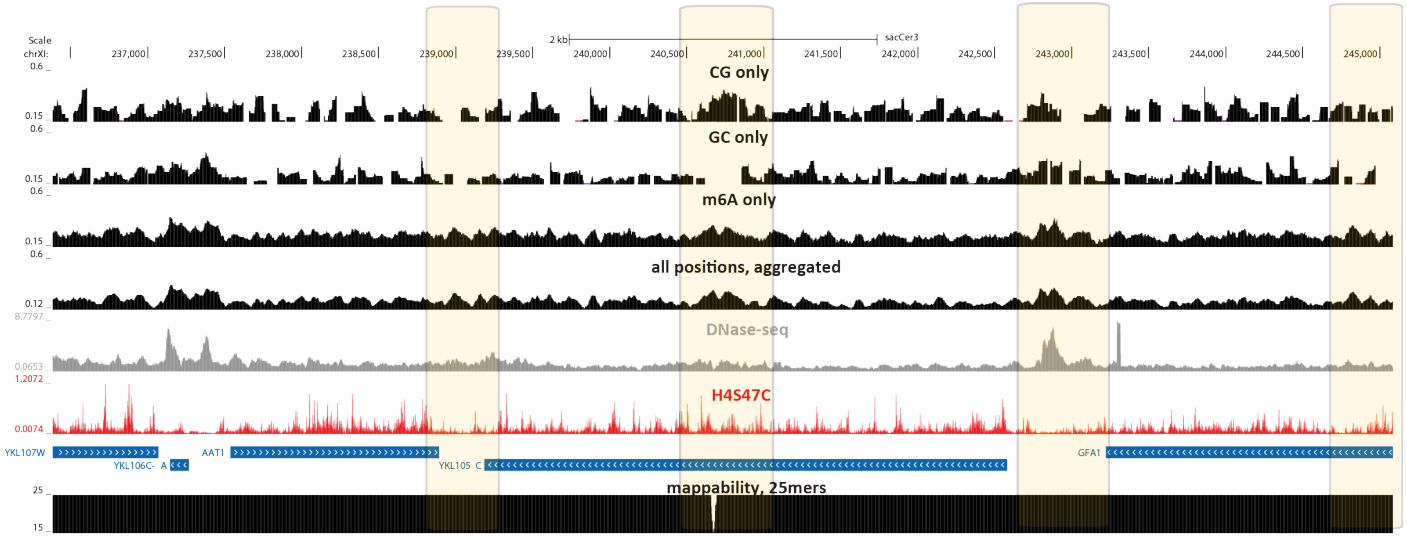

Supplementary Figure 41: Impact of the addition of m^6A on assay resolution. Shown is the average accessibility status measured by CG, GC or m^6A modifications alone and with all positions aggregated together (calculated over 50bp windows, with a step size of 5, as in Figure 1). The sparseness of CG and GC dinucleotides in the genome results in numerous positions where data is completely missing and to low resolution not allowing the identification of numerous positioned nucleosomes and even entire accessibility peaks.

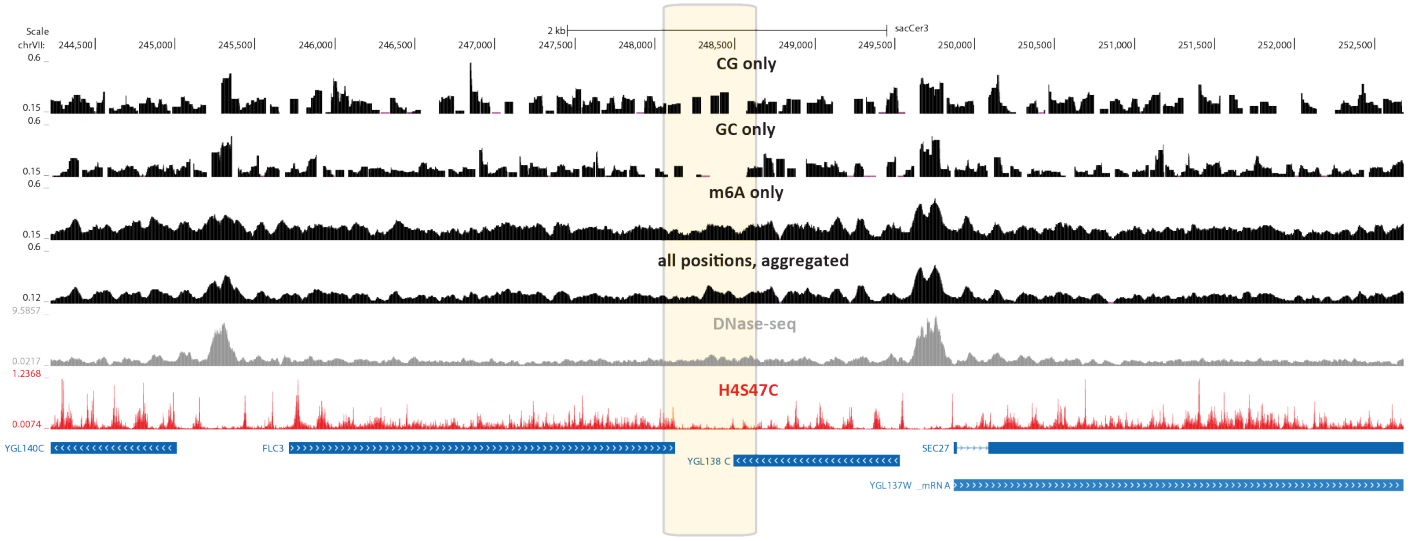

Supplementary Figure 42: Impact of the addition of m^{6}A on assay resolution. Shown is the average accessibility status measured by CG, GC or m^{6}A modifications alone and with all positions aggregated together (calculated over 50bp windows, with a step size of 5, as in Figure 1). The sparseness of CG and GC dinucleotides in the genome results in numerous positions where data is completely missing and to low resolution not allowing the identification of numerous positioned nucleosomes and even entire accessibility peaks.

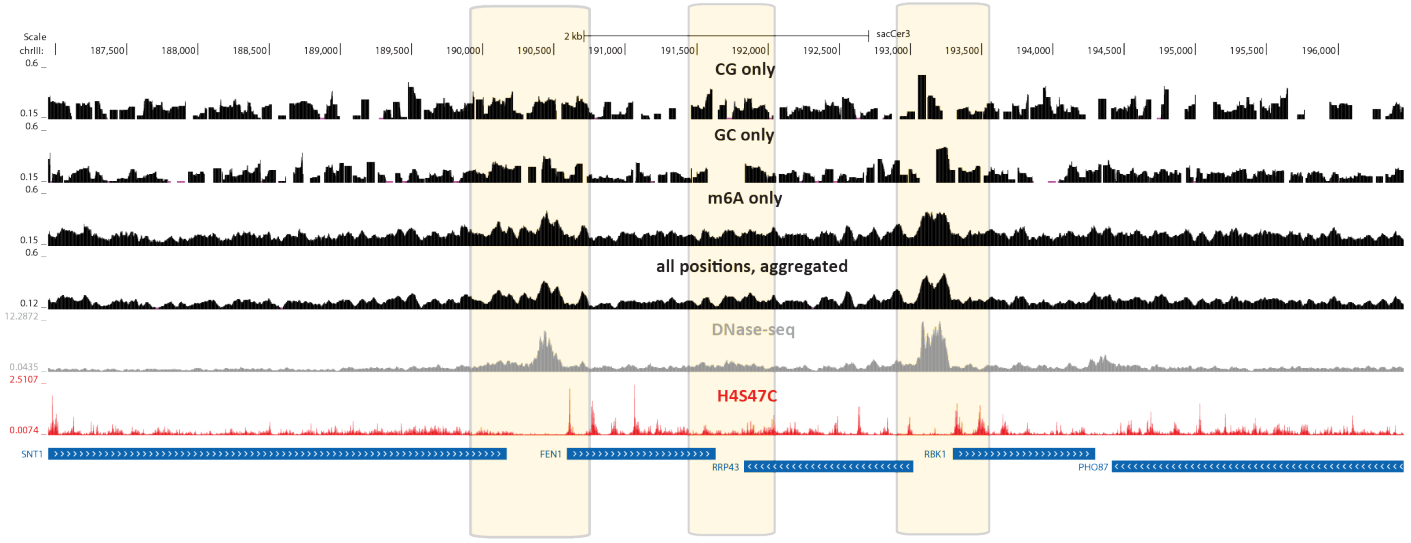

Supplementary Figure 43: Impact of the addition of m^{6}A on assay resolution. Shown is the average accessibility status measured by CG, GC or m^{6}A modifications alone and with all positions aggregated together (calculated over 50bp windows, with a step size of 5, as in Figure 1). The sparseness of CG and GC dinucleotides in the genome results in numerous positions where data is completely missing and to low resolution not allowing the identification of numerous positioned nucleosomes and even entire accessibility peaks.

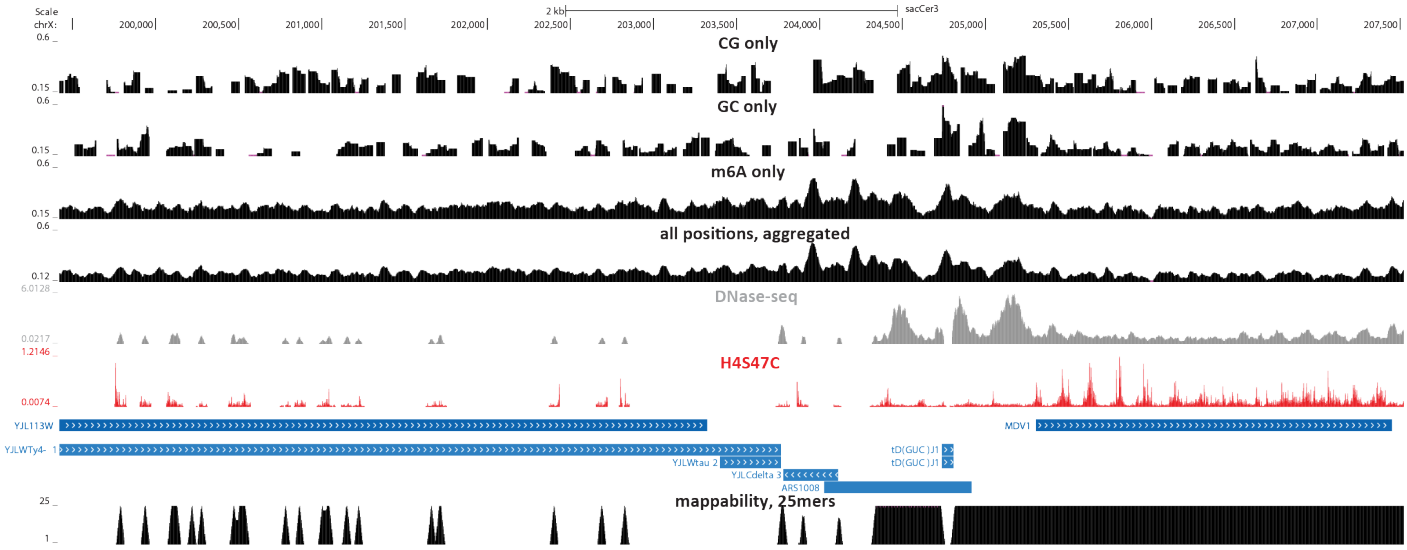

Supplementary Figure 44: Impact of the addition of m^6A on assay resolution. Shown is the average accessibility status measured by CG, GC or m^6A modifications alone and with all positions aggregated together (calculated over 50bp windows, with a step size of 5, as in Figure 1). The sparseness of CG and GC dinucleotides in the genome results in numerous positions where data is completely missing and to low resolution not allowing the identification of numerous positioned nucleosomes and even entire accessibility peaks.

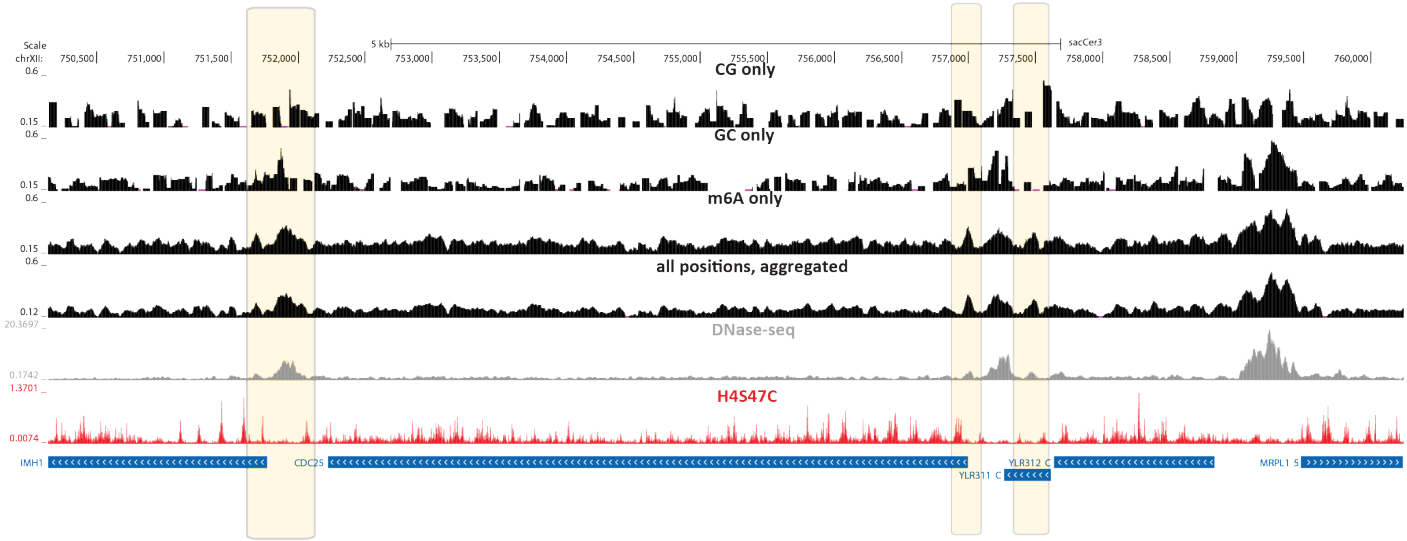

Supplementary Figure 45: Impact of the addition of m^6A on assay resolution. Shown is the average accessibility status measured by CG, GC or m^6A modifications alone and with all positions aggregated together (calculated over 50bp windows, with a step size of 5, as in Figure 1). The sparseness of CG and GC dinucleotides in the genome results in numerous positions where data is completely missing and to low resolution not allowing the identification of numerous positioned nucleosomes and even entire accessibility peaks.

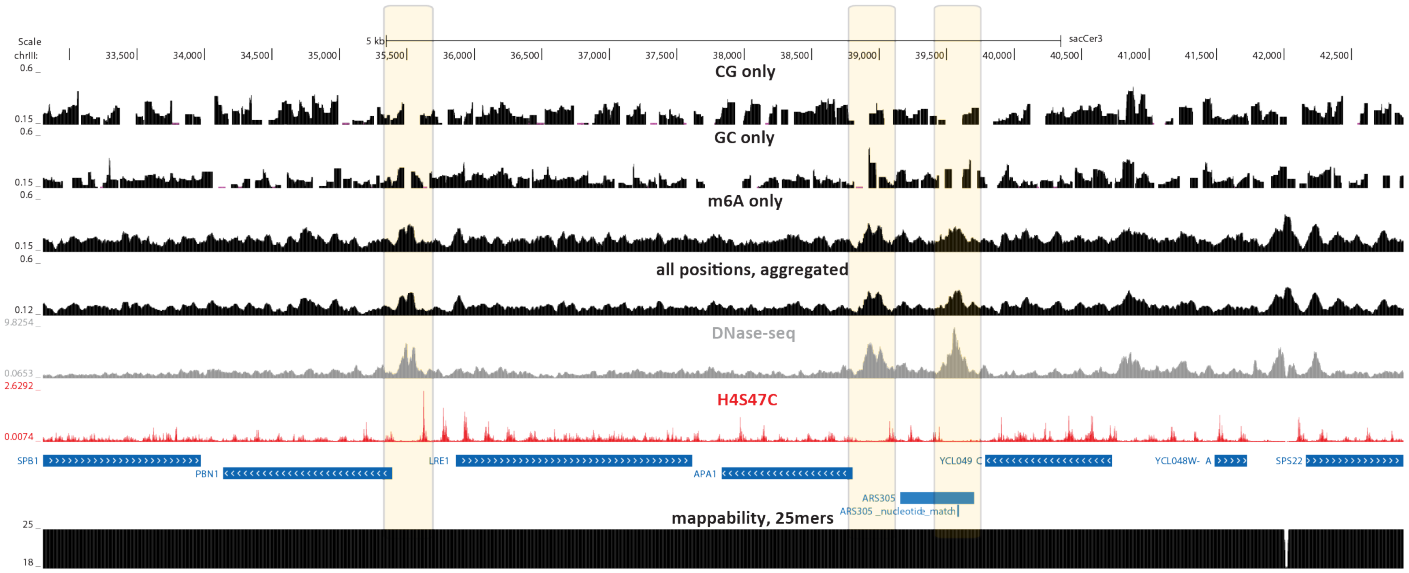

Supplementary Figure 46: Impact of the addition of m^6A on assay resolution. Shown is the average accessibility status measured by CG, GC or m^6A modifications alone and with all positions aggregated together (calculated over 50bp windows, with a step size of 5, as in Figure 1). The sparseness of CG and GC dinucleotides in the genome results in numerous positions where data is completely missing and to low resolution not allowing the identification of numerous positioned nucleosomes and even entire accessibility peaks.

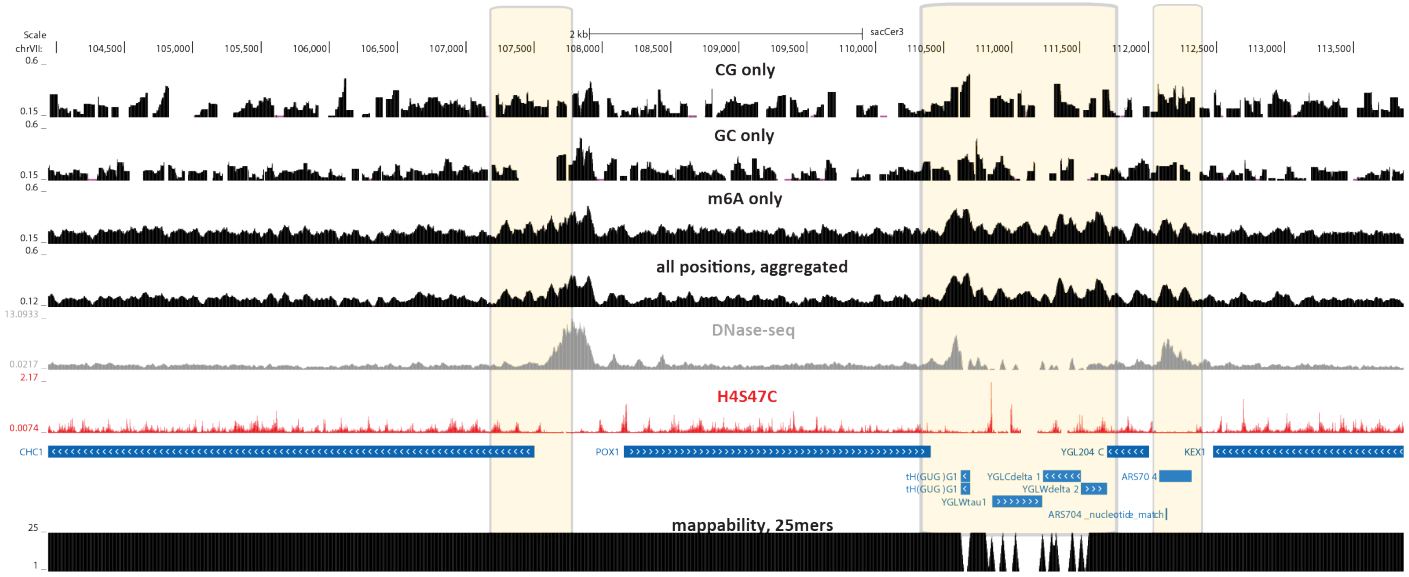

Supplementary Figure 47: Impact of the addition of m^6A on assay resolution. Shown is the average accessibility status measured by CG, GC or m^6A modifications alone and with all positions aggregated together (calculated over 50bp windows, with a step size of 5, as in Figure 1). The sparseness of CG and GC dinucleotides in the genome results in numerous positions where data is completely missing and to low resolution not allowing the identification of numerous positioned nucleosomes and even entire accessibility peaks.

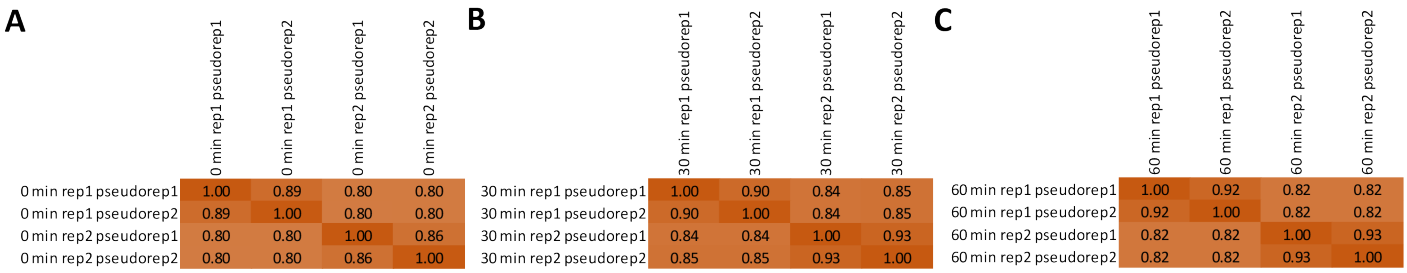

Supplementary Figure 48: Correlation at the base pair level between replicates and pseudoreplicates. Shown are the Pearson r^2 values for the average methylation calls for each position in the yeast genome between pseudoreplicates (generated by randomly splitting reads in two halves) of the same and different biological replicates (tracks generated as shown in Figure 1).

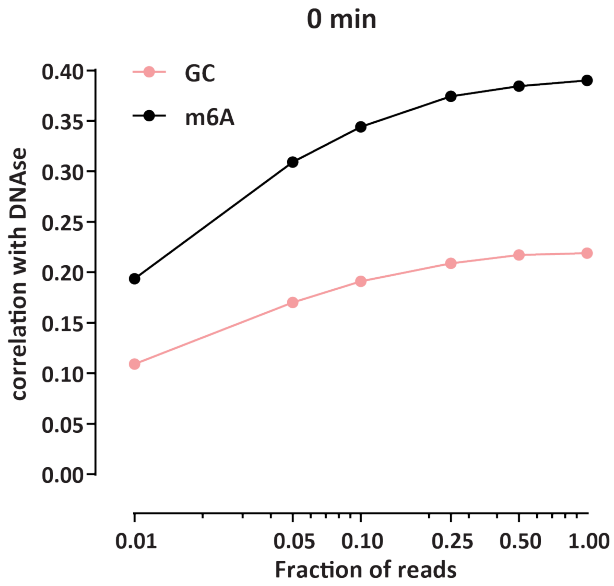

Supplementary Figure 49: Impact of the addition of m^{6}A on assay resolution. Shown are Spearman correlation values between average methylation calls and smoothed (over 10bp) DNAse-seq tracks for each position in the yeast genome (without filtering out positions that are not uniquely mappable) for different subsamplings of SMAC-seq reads. Due to the sparseness of GC dinucleotides in the genome results, using GC methylation alone captures the accessibility signal much more poorly than what is enabled by the dense coverage provided by m^{6}A, as also shown above in Supplementary Figures 19–47

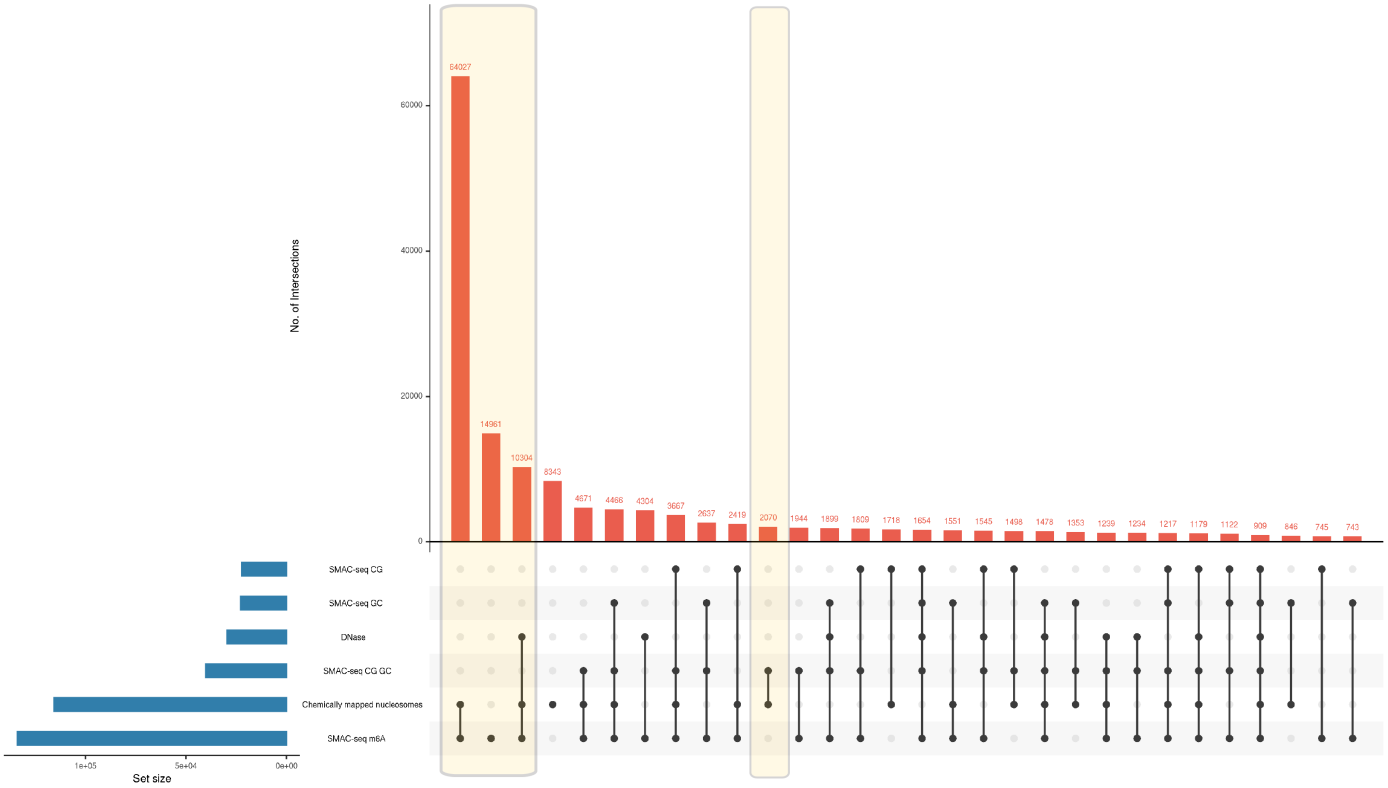

Supplementary Figure 50: Impact of the addition of m^{6}A on assay resolution. Accessible chromatin peaks and positioned nucleosomes are accurately called only using m^{6}A while CG/GC dinucleotides provide insufficient such information. Peaks were called from signal tracks using gNOMePeaks (`https://github.com/karl616/gNOMePeaks`) with default settings. Peaks smaller than 5bp were filtered out and peaks $\leq$25bp apart each other were merged.

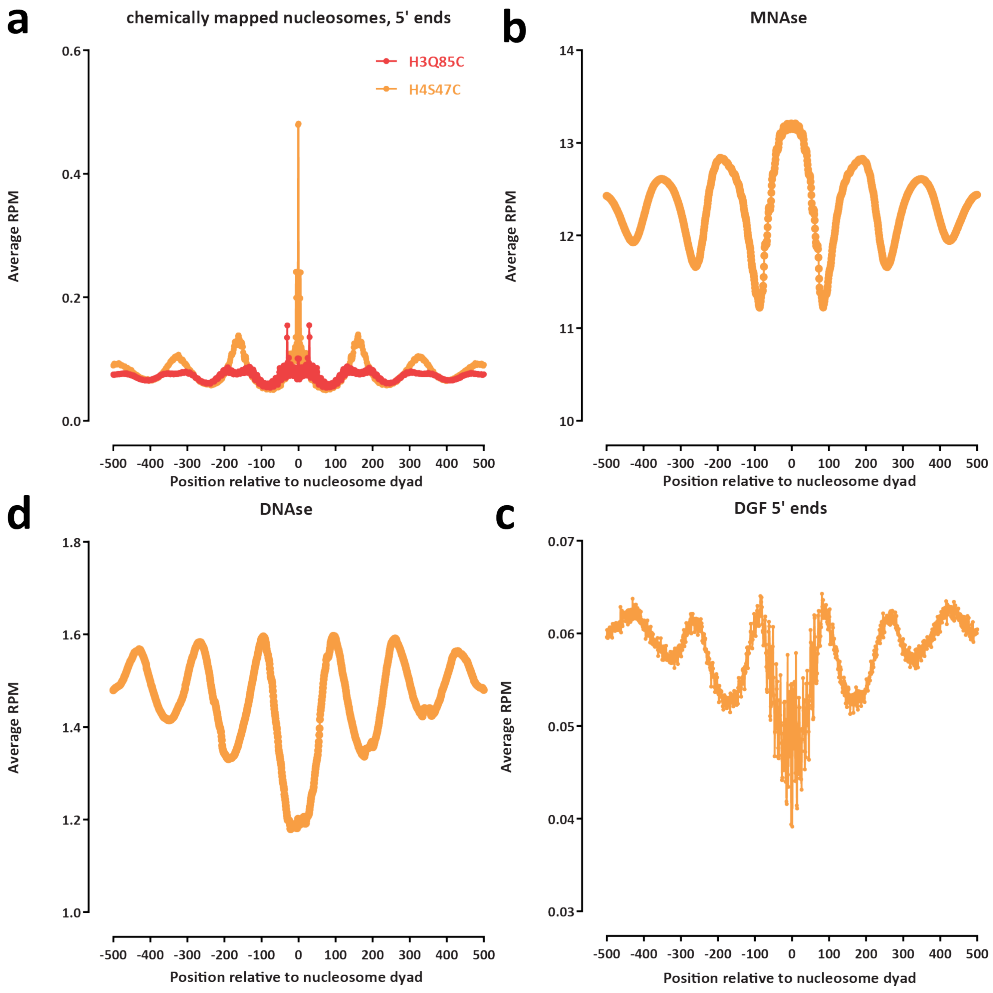

Supplementary Figure 51: Correlation of SMAC-seq (Figure 1e) with other measures of chromatin structure around the dyad centers of positioned nucleosomes in the *S. cerevisiae* genome. (a) H4S47C and H3Q85C nucleosome chemical mapping; (b) MNaseq-seq; (c) DNase-seq; (d) Digital Genomic Footprinting (DGF, 5′ ends of deeply sequenced DNAseq-seq data).

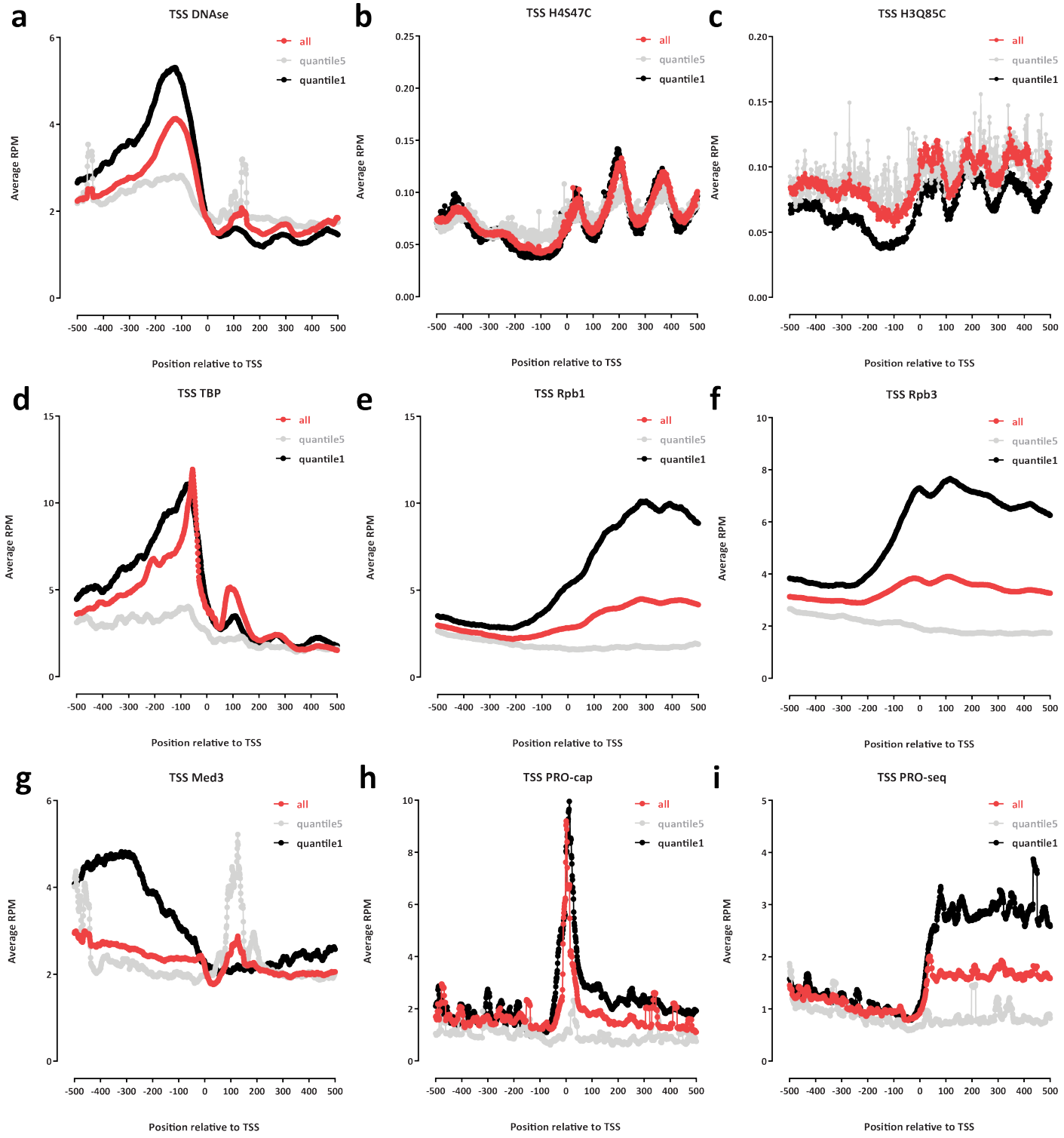

Supplementary Figure 52: Correlation of SMAC-seq (Figure 1f and g) with other types of functional genomic measurements of chromatin structure, protein occupancy and transcriptional activity around TSSs. Shown is average coverage over all *S. cerevisiae* genes, for the most highly expressed 20% of genes ("quantile1"), and for the bottom 20% of genes ("quantile5"). (a) DNase-seq; (b) H4S47C nucleosome chemical mapping; (c) H3Q85C nucleosome chemical mapping; (d) TBP ChIP-seq; (e) Rpb1 ChIP-seq; (f) Rpb3 ChIP-seq; (g) Med3 ChIP-seq; (h) PRO-cap; (i) PRO-seq.

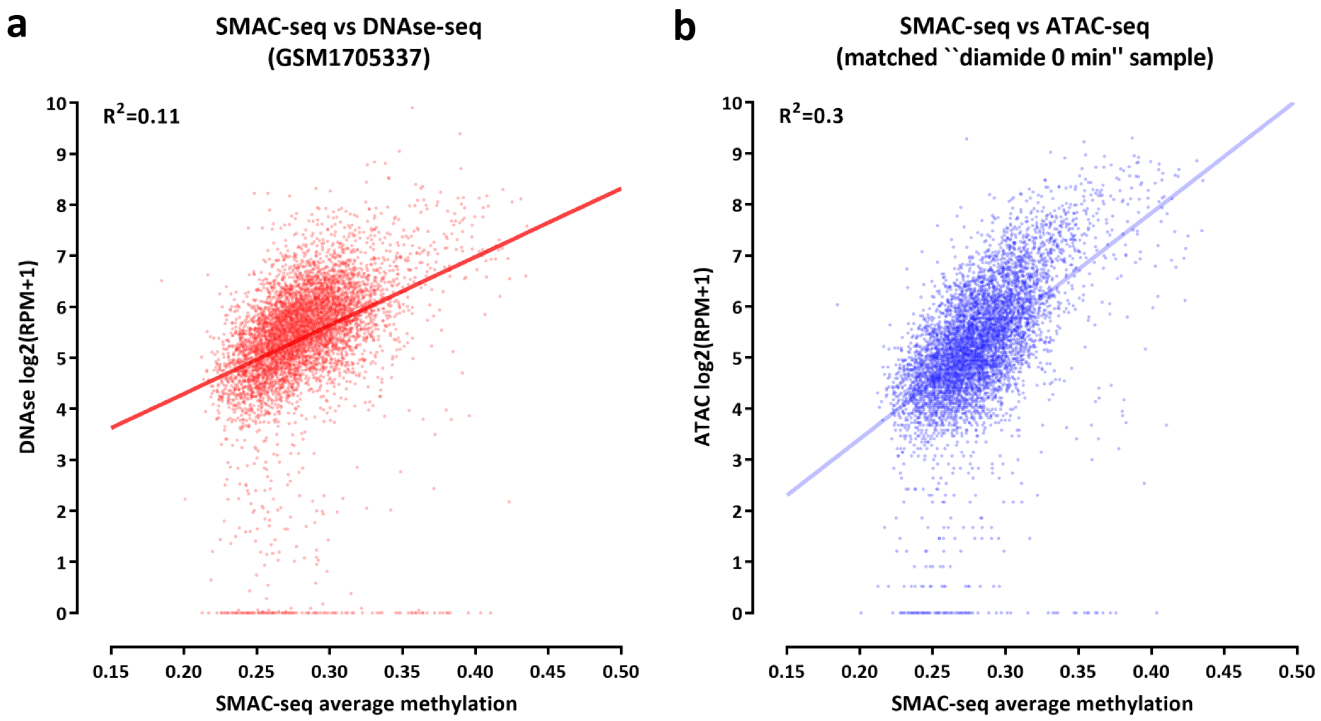

Supplementary Figure 53: Correlation of SMAC-seq signal with ATAC-seq and DNA-seq signal over yeast promoters. Shown is the average methylation over the TSS ± 200 bp for SMAC-seq and RPM (Reads Per Million mapped reads) values for DNase-seq (a) and ATAC-seq (b). Note that the DNase-seq dataset is obtained from an external study while the SMAC-seq and ATAC-seq ones are from the same sample ("diamide 0 min rep1").

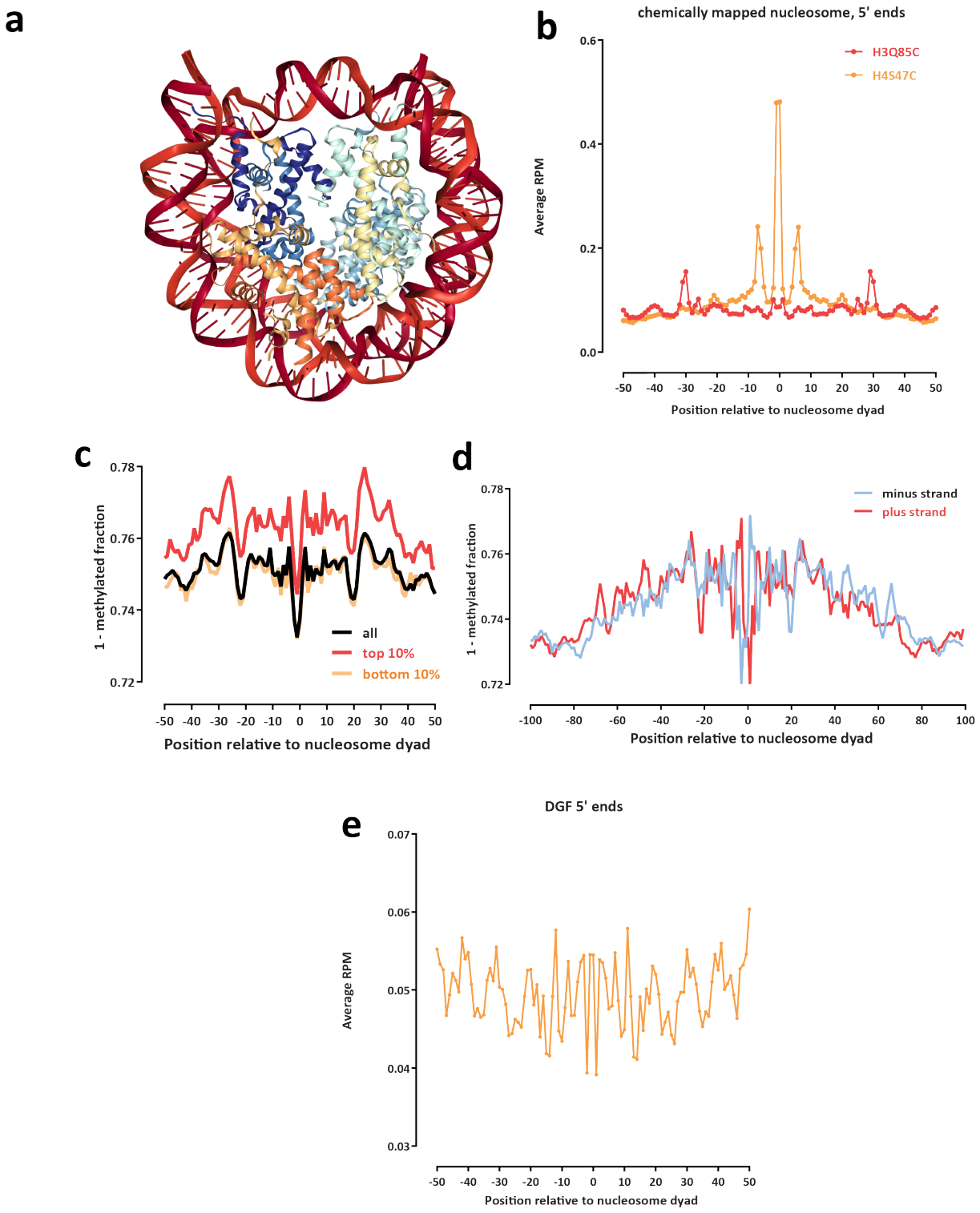

Supplementary Figure 54: SMAC-seq data displays higher methylation propensity in more exposed parts of the nucleosomal particle. (a) Structure of the eukaryotic nucleosome; (b) High-resolution (50-bp radius) view of chemical nucleosome mapping data relative to nucleosome dyads; (c) High-resolution (50-bp radius) view of SMAC-seq data relative to nucleosome dyads; (d) Strand-specific (100-bp radius) view of SMAC-seq data relative to nucleosome dyads; (e) High-resolution (50-bp radius) view of DGF cleavage profiles relative to nucleosome dyads.

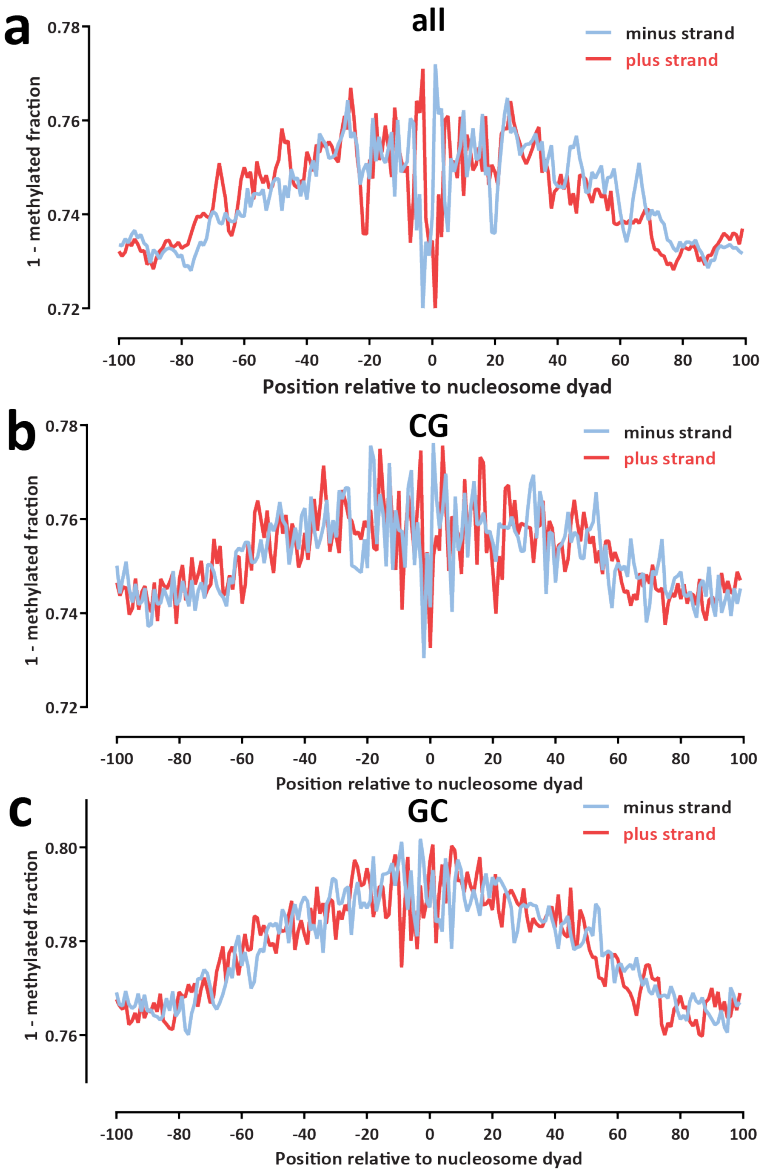

Supplementary Figure 55: Strand-specific nucleosome accessibility/occupancy is most clearly revealed by m^{6}A methylation using EcoGII. (a) Strand-specific (100-bp radius) view of SMAC-seq data relative to nucleosome dyads using all positions; (b) Strand-specific (100-bp radius) view of SMAC-seq data relative to nucleosome dyads using CG positions; (c) Strand-specific (100-bp radius) view of SMAC-seq data relative to nucleosome dyads using GC positions.

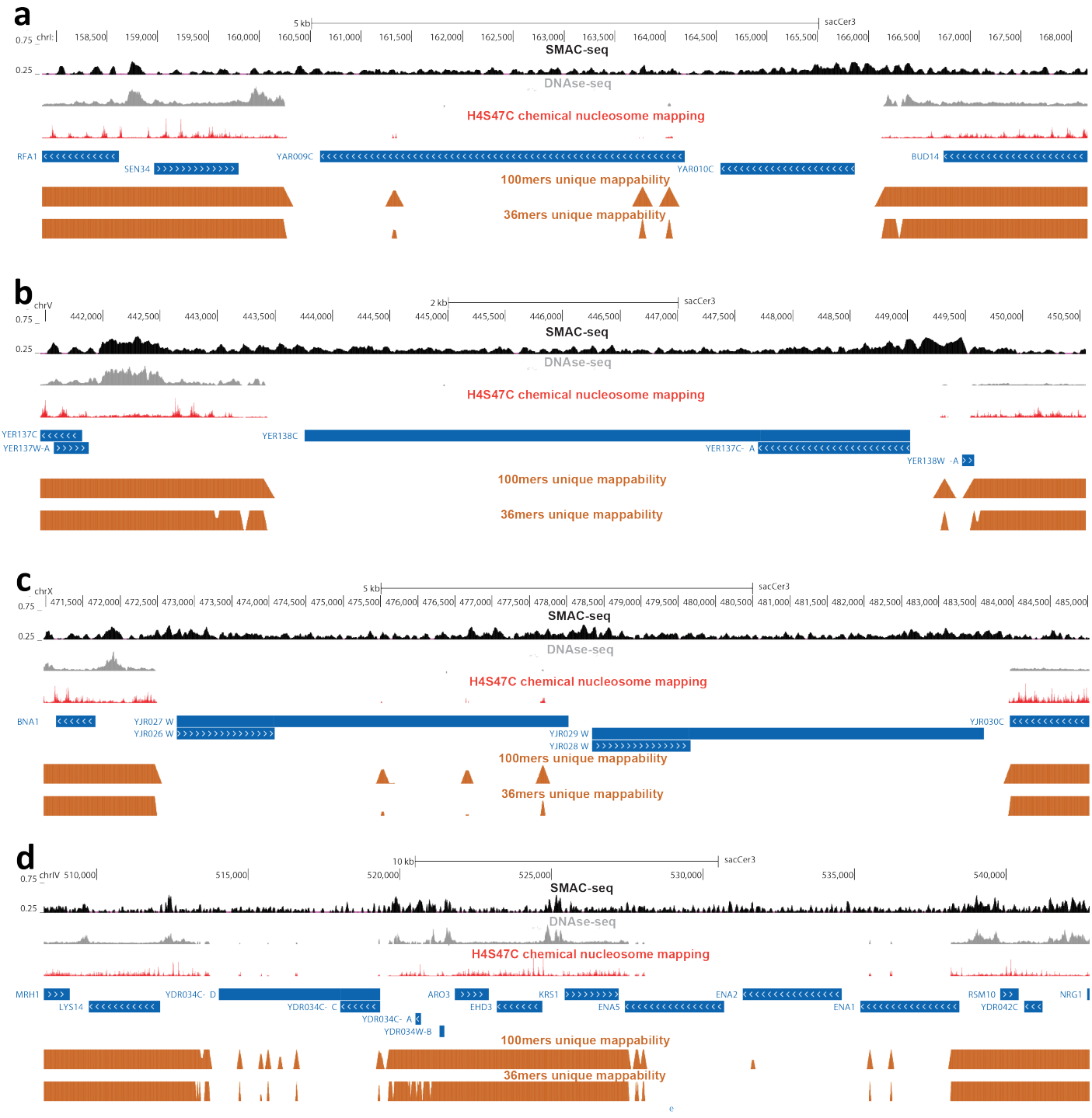

Supplementary Figure 56: SMAC-seq provides coverage of areas of the genome that cannot be uniquely mapped using short reads. Four different repetitive regions are shown (a, b, c and d) together with short read coverage for DNase-seq and chemical nucleosome mapping data and unique mappability tracks for 36mers and 100mers.

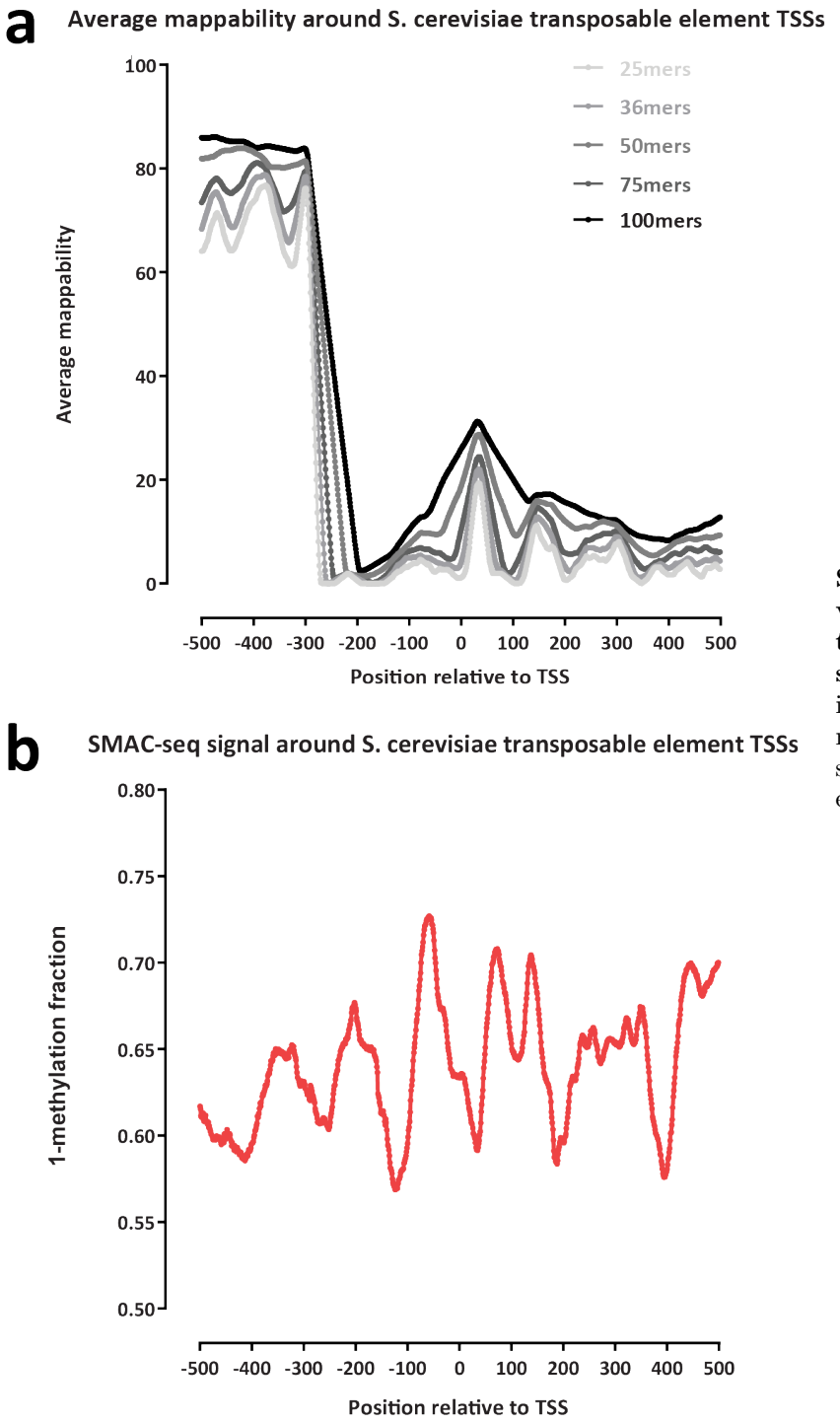

Supplementary Figure 57: SMAC-seq provides coverage of areas of the genome that cannot be uniquely mapped using short reads. (a) Average short-read mappability around TSSs of annotated transposable elements in the *S. cerevisiae* genome; (b) SMAC-seq signal around TSSs of annotated transposable elements in the *S. cerevisiae* genome.

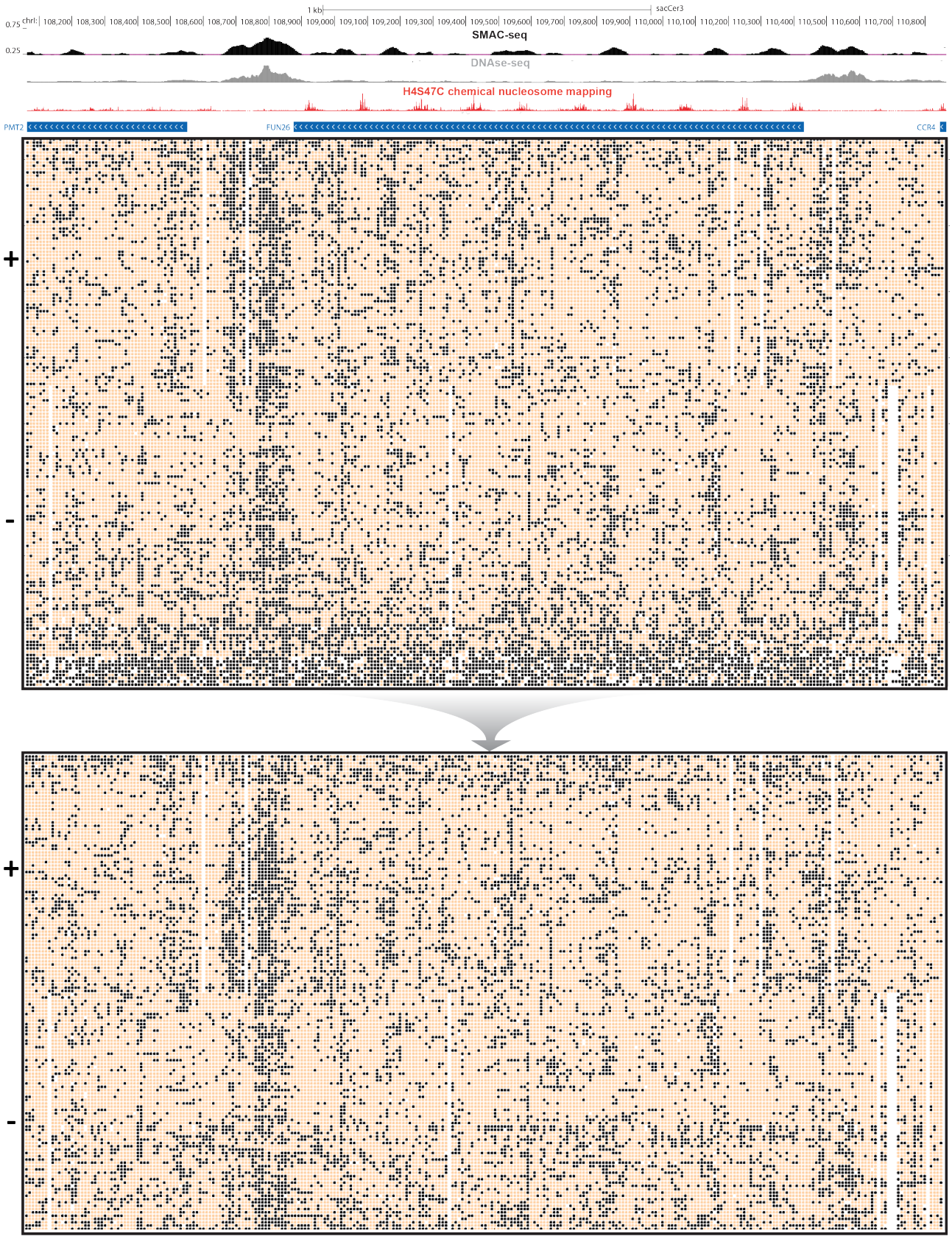

Supplementary Figure 58: Removal of potentially artifactual high-methylation reads. Shown is unfiltered SMAC-seq data and the same locus after removal of all reads containing a 1-kb ≥75% methylated stretch (average accessibility over 10 bp).

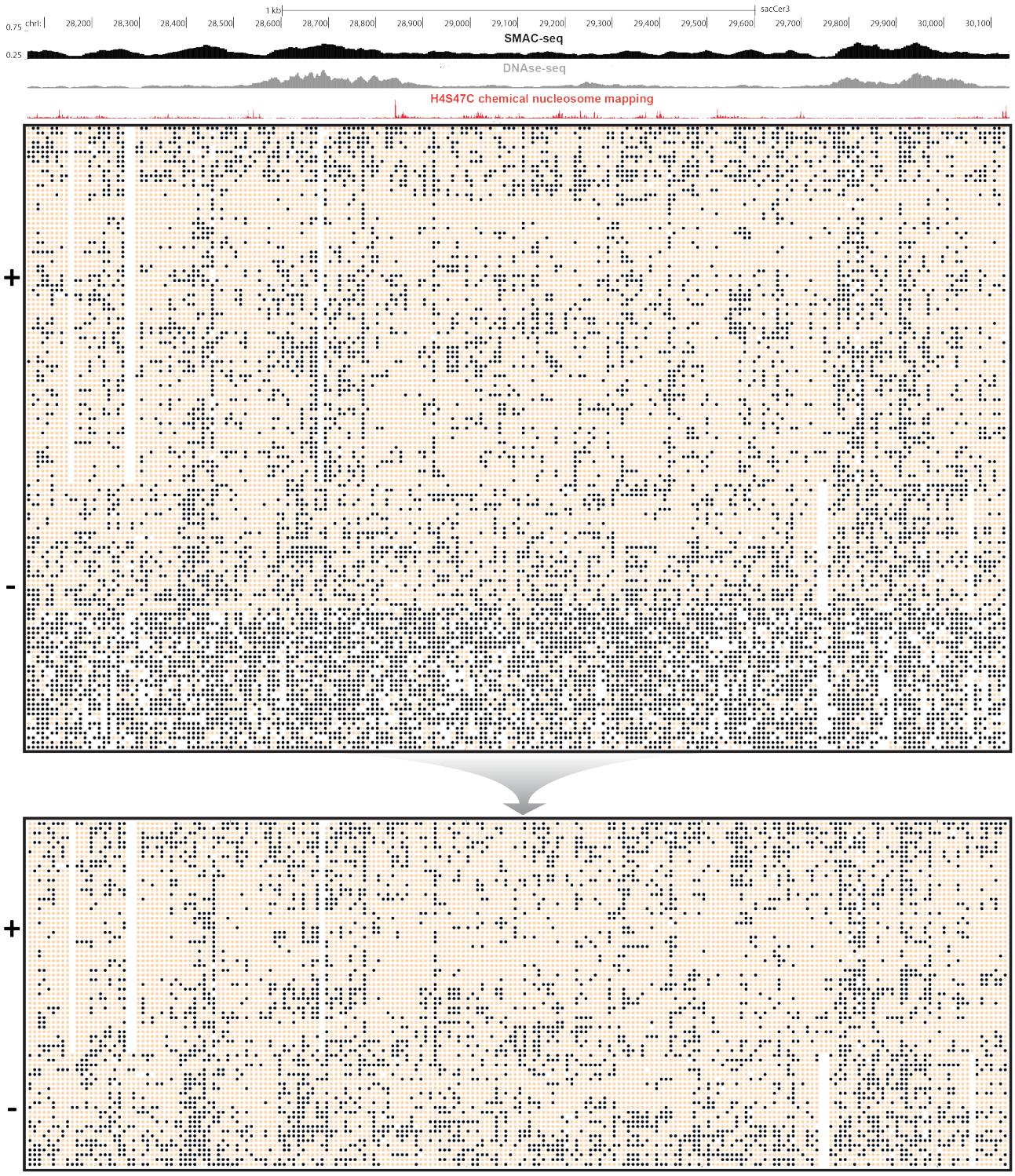

Supplementary Figure 59: Removal of potentially artifactual high-methylation reads. Shown is unfiltered SMAC-seq data and the same locus after removal of all reads containing a 1-kb ≥75% methylated stretch (average accessibility over 10 bp).

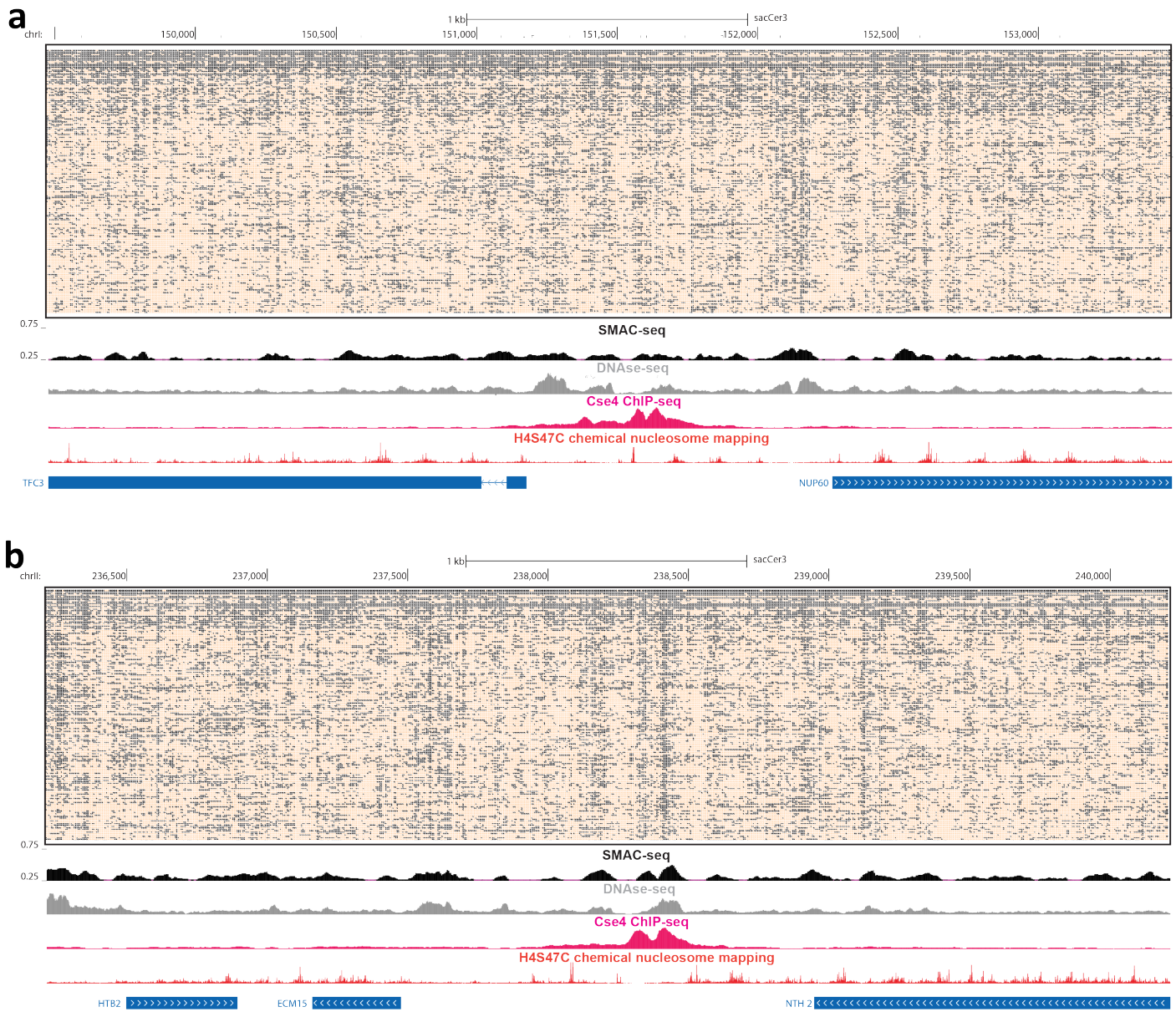

Supplementary Figure 60: Single-molecule long-read accessibility around well positioned centromeres. (a) Raw unfiltered nanopore reads fully spanning the 4-kilobase neighborhood of the centromere of *S. cerevisiae* chrI; (b) Raw unfiltered nanopore reads fully spanning the 4-kilobase neighborhood of the centromere of *S. cerevisiae* chrII. In both cases, accessibility is shown at aggregated 10-bp resolution (see Methods section for details) for the single-molecule display, and aggregated over sliding (every 5 bases) 50-bp windows for the genome browser SMAC-seq track.

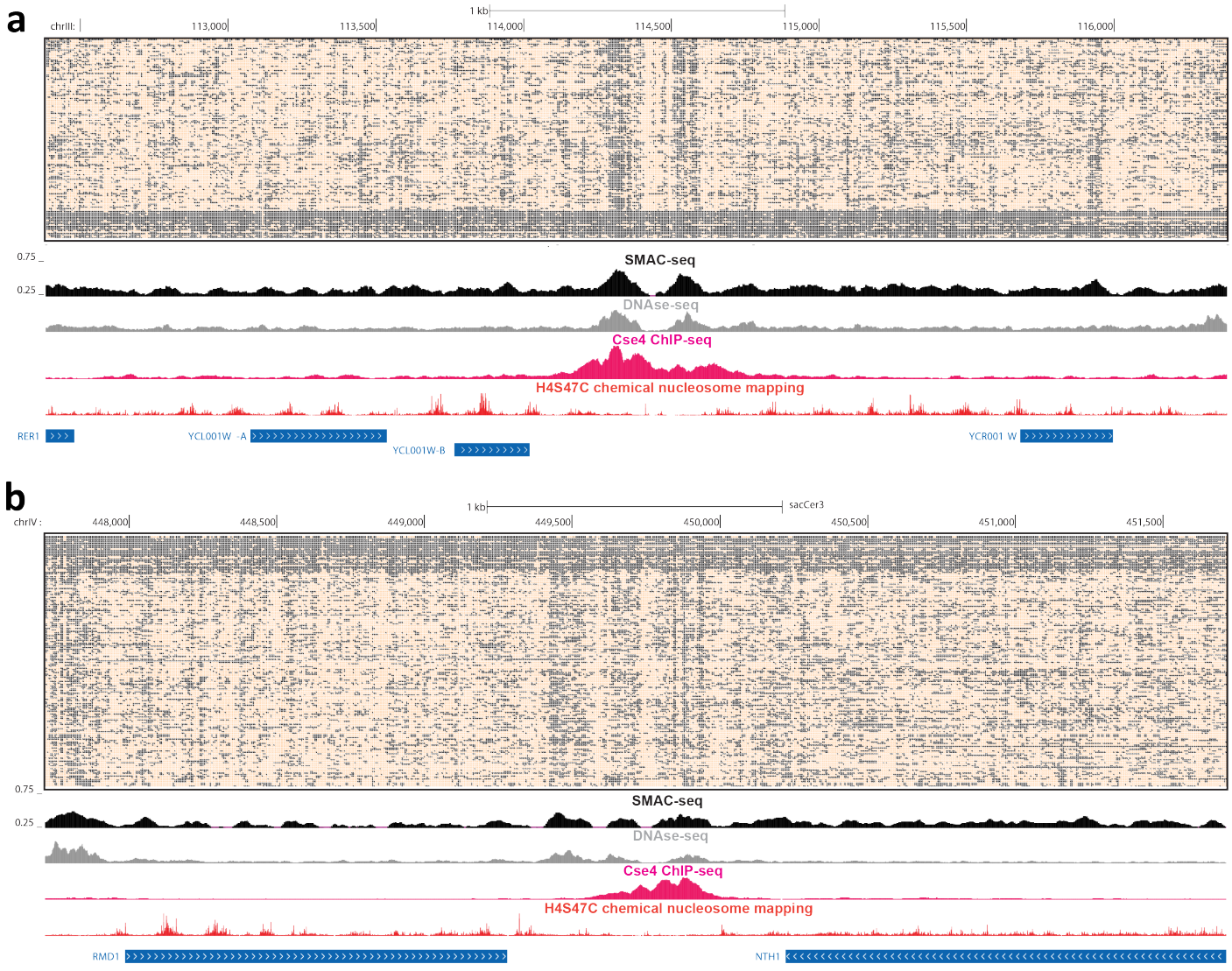

Supplementary Figure 61: Single-molecule long-read accessibility around well positioned centromeres. (a) Raw unfiltered nanopore reads fully spanning the 4-kilobase neighborhood of the centromere of *S. cerevisiae* chrIII; (b) Raw unfiltered nanopore reads fully spanning the 4-kilobase neighborhood of the centromere of *S. cerevisiae* chrIV. In both cases, accessibility is shown at aggregated 10-bp resolution (see Methods section for details) for the single-molecule display, and aggregated over sliding (every 5 bases) 50-bp windows for the genome browser SMAC-seq track.

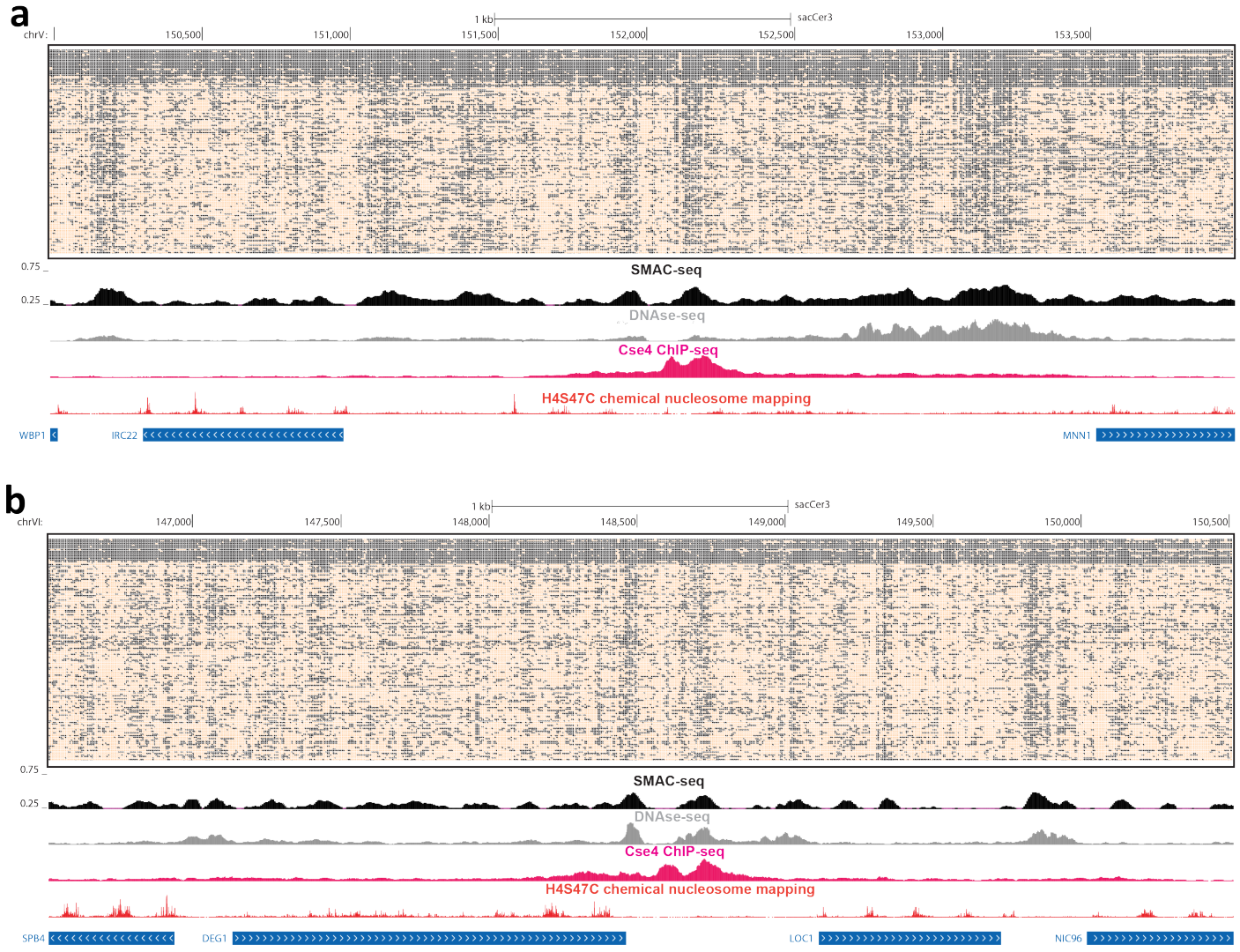

Supplementary Figure 62: Single-molecule long-read accessibility around well positioned centromeres. (a) Raw unfiltered nanopore reads fully spanning the 4-kilobase neighborhood of the centromere of *S. cerevisiae* chrV; (b) Raw unfiltered nanopore reads fully spanning the 4-kilobase neighborhood of the centromere of *S. cerevisiae* chrVI. In both cases, accessibility is shown at aggregated 10-bp resolution (see Methods section for details) for the single-molecule display, and aggregated over sliding (every 5 bases) 50-bp windows for the genome browser SMAC-seq track.

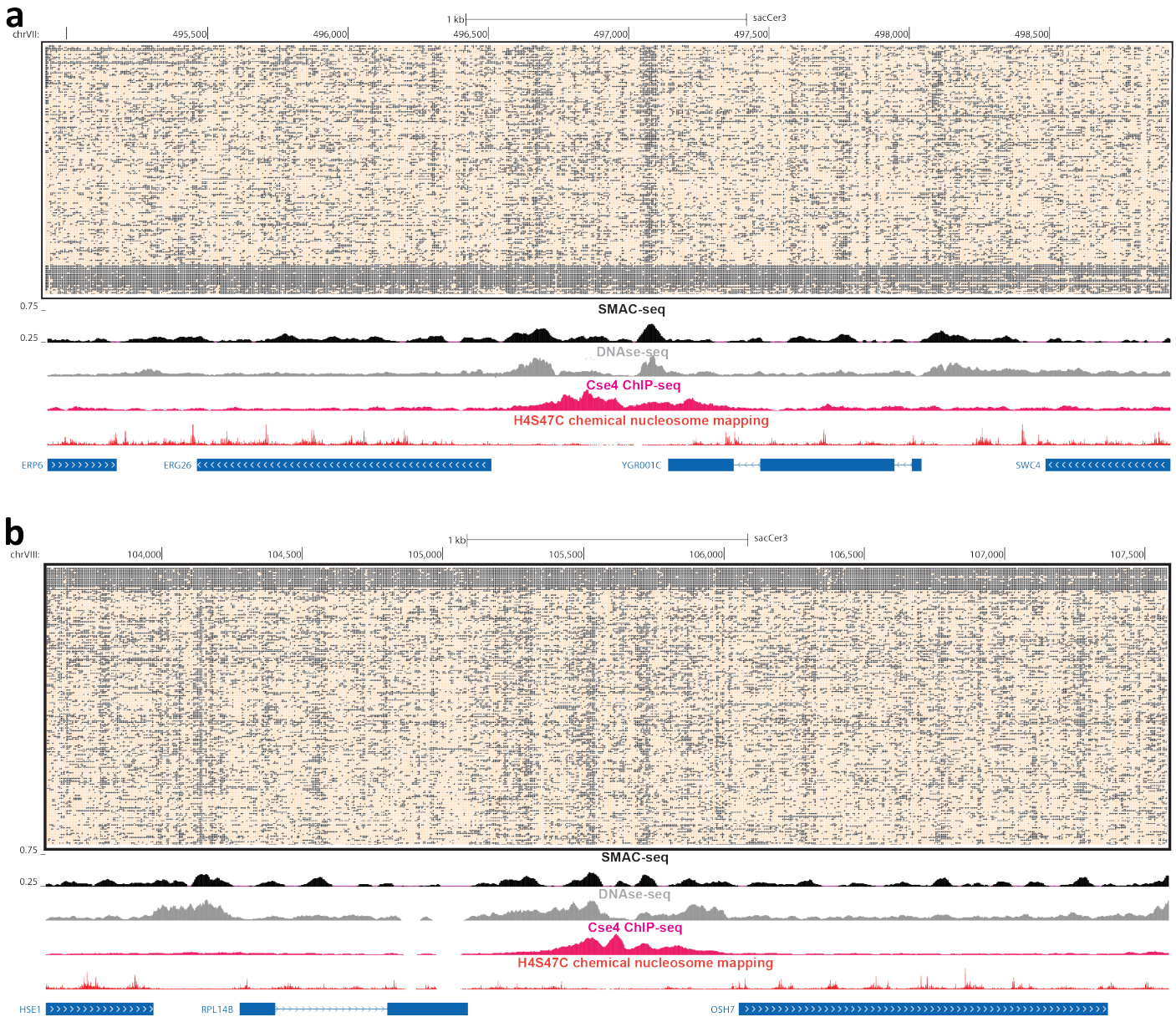

Supplementary Figure 63: Single-molecule long-read accessibility around well positioned centromeres. (a) Raw unfiltered nanopore reads fully spanning the 4-kilobase neighborhood of the centromere of *S. cerevisiae* chrVII; (b) Raw unfiltered nanopore reads fully spanning the 4-kilobase neighborhood of the centromere of *S. cerevisiae* chrVIII. In both cases, accessibility is shown at aggregated 10-bp resolution (see Methods section for details) for the single-molecule display, and aggregated over sliding (every 5 bases) 50-bp windows for the genome browser SMAC-seq track.

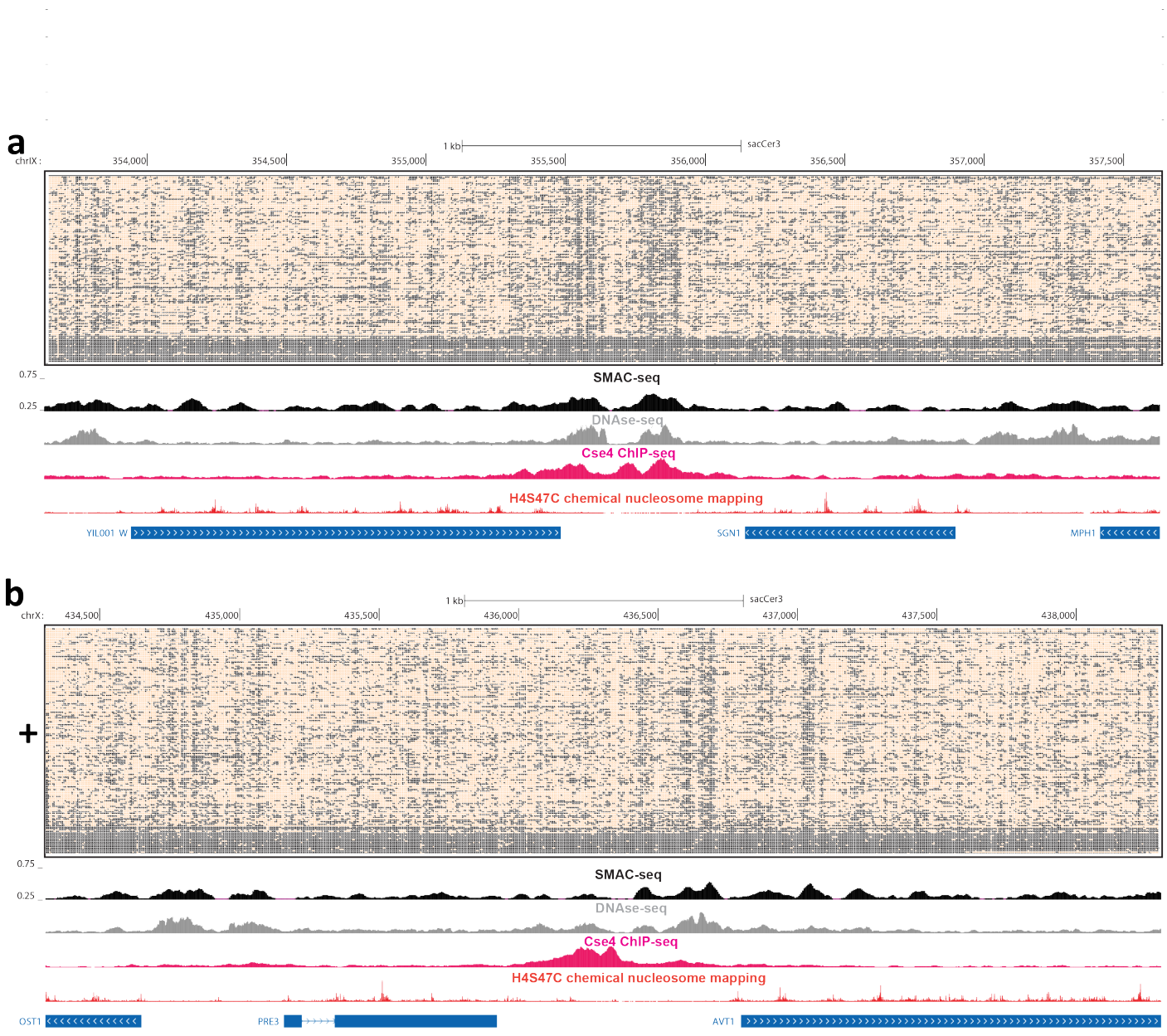

Supplementary Figure 64: Single-molecule long-read accessibility around well positioned centromeres. (a) Raw unfiltered nanopore reads fully spanning the 4-kilobase neighborhood of the centromere of *S. cerevisiae* chrIX; (b) Raw unfiltered nanopore reads fully spanning the 4-kilobase neighborhood of the centromere of *S. cerevisiae* chrX. In both cases, accessibility is shown at aggregated 10-bp resolution (see Methods section for details) for the single-molecule display, and aggregated over sliding (every 5 bases) 50-bp windows for the genome browser SMAC-seq track.

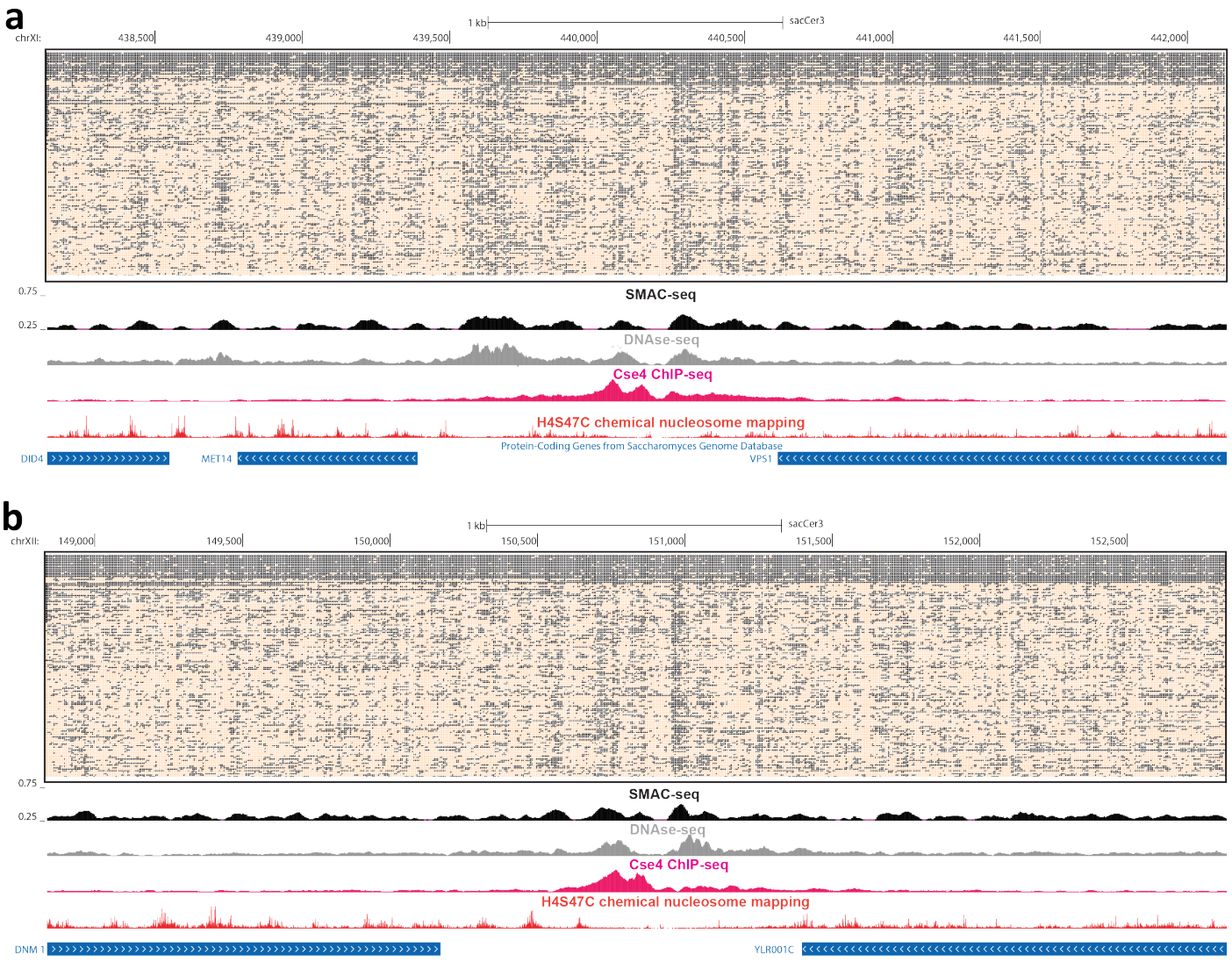

Supplementary Figure 65: Single-molecule long-read accessibility around well positioned centromeres. (a) Raw unfiltered nanopore reads fully spanning the 4-kilobase neighborhood of the centromere of *S. cerevisiae* chrXI; (b) Raw unfiltered nanopore reads fully spanning the 4-kilobase neighborhood of the centromere of *S. cerevisiae* chrXII. In both cases, accessibility is shown at aggregated 10-bp resolution (see Methods section for details) for the single-molecule display, and aggregated over sliding (every 5 bases) 50-bp windows for the genome browser SMAC-seq track.

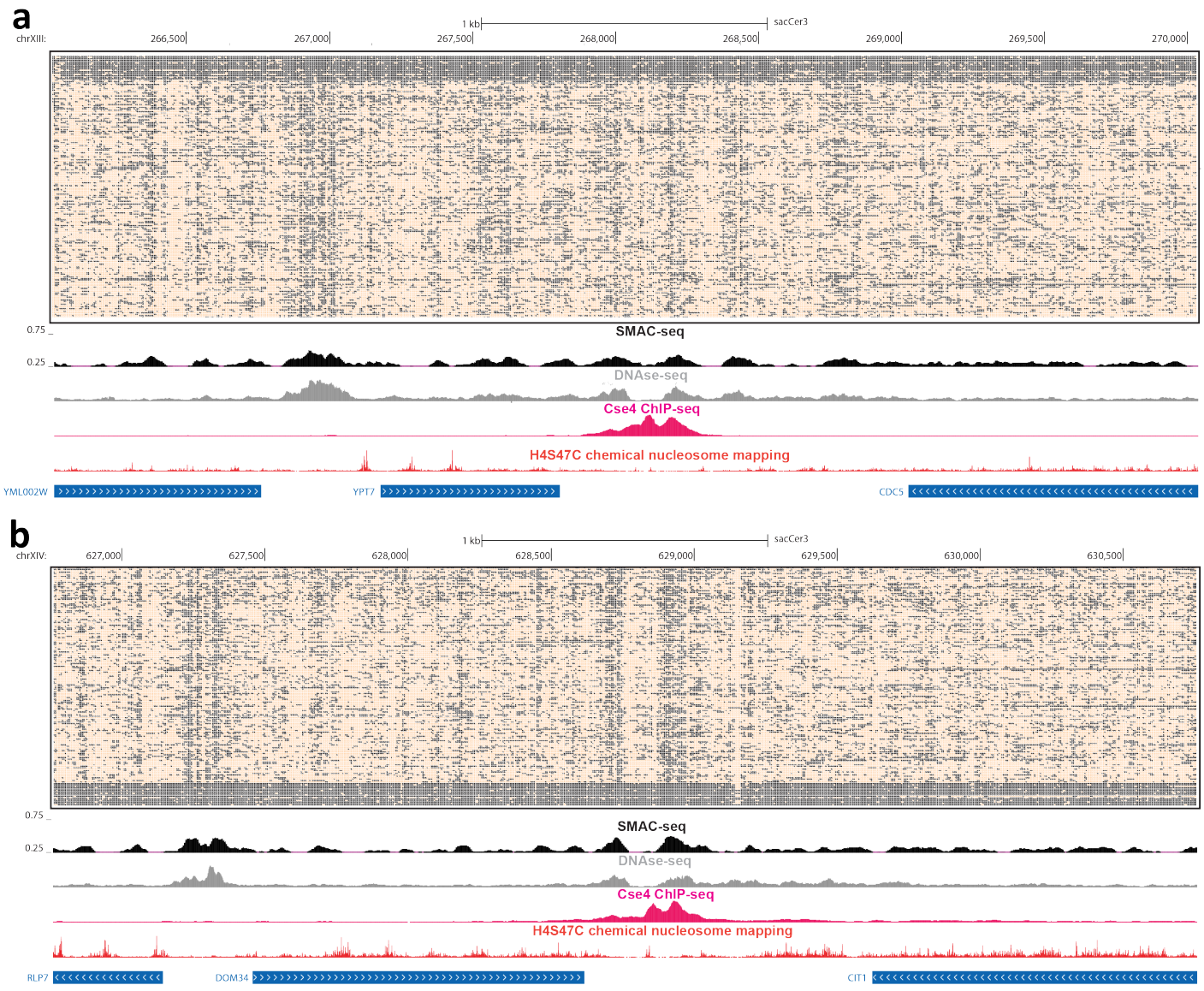

Supplementary Figure 66: Single-molecule long-read accessibility around well positioned centromeres. (a) Raw unfiltered nanopore reads fully spanning the 4-kilobase neighborhood of the centromere of *S. cerevisiae* chrXIII; (b) Raw unfiltered nanopore reads fully spanning the 4-kilobase neighborhood of the centromere of *S. cerevisiae* chrXIV. In both cases, accessibility is shown at aggregated 10-bp resolution (see Methods section for details) for the single-molecule display, and aggregated over sliding (every 5 bases) 50-bp windows for the genome browser SMAC-seq track.

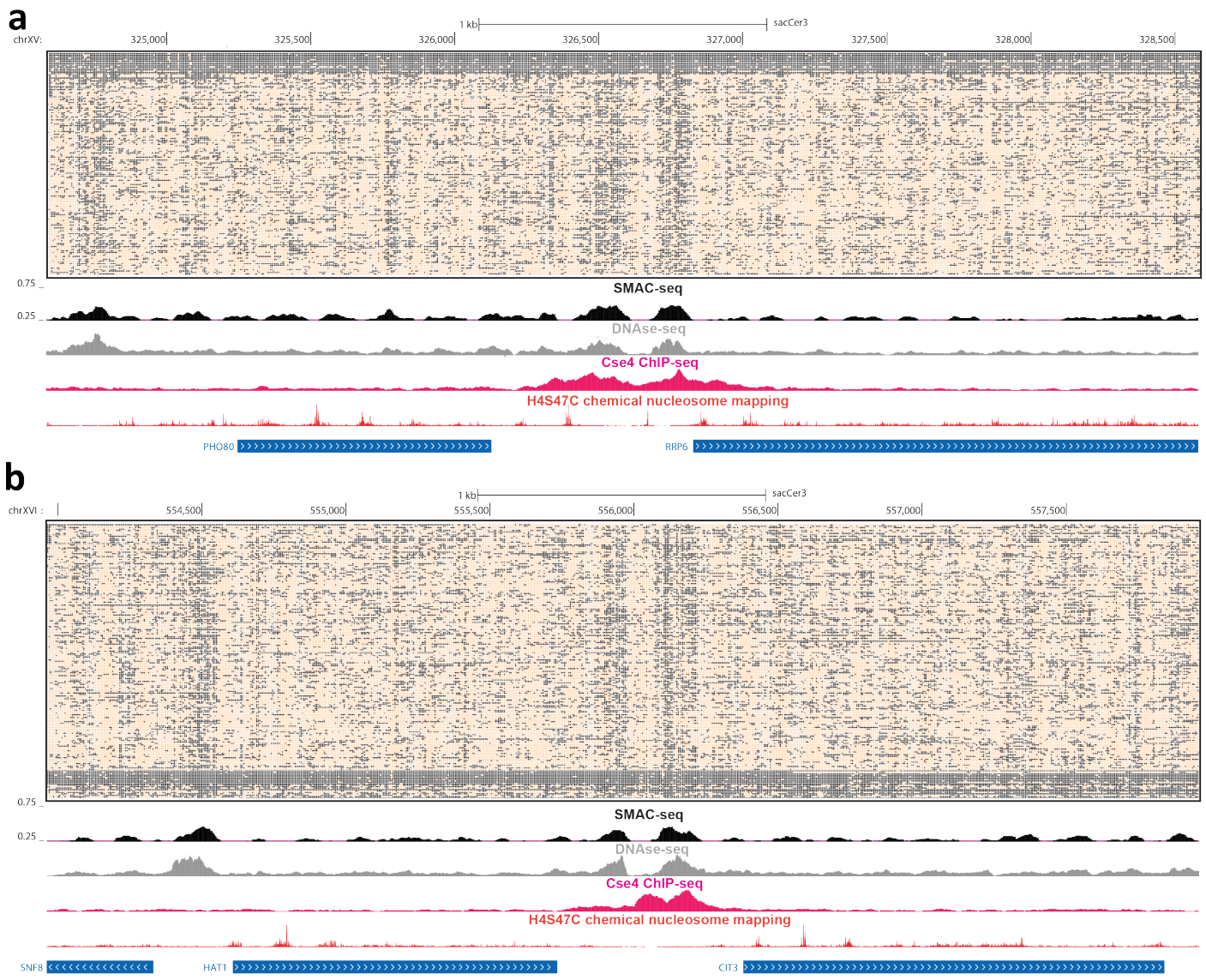

Supplementary Figure 67: Single-molecule long-read accessibility around well positioned centromeres. (a) Raw unfiltered nanopore reads fully spanning the 4-kilobase neighborhood of the centromere of *S. cerevisiae* chrXV; (b) Raw unfiltered nanopore reads fully spanning the 4-kilobase neighborhood of the centromere of *S. cerevisiae* chrXVI. In both cases, accessibility is shown at aggregated 10-bp resolution (see Methods section for details) for the single-molecule display, and aggregated over sliding (every 5 bases) 50-bp windows for the genome browser SMAC-seq track.

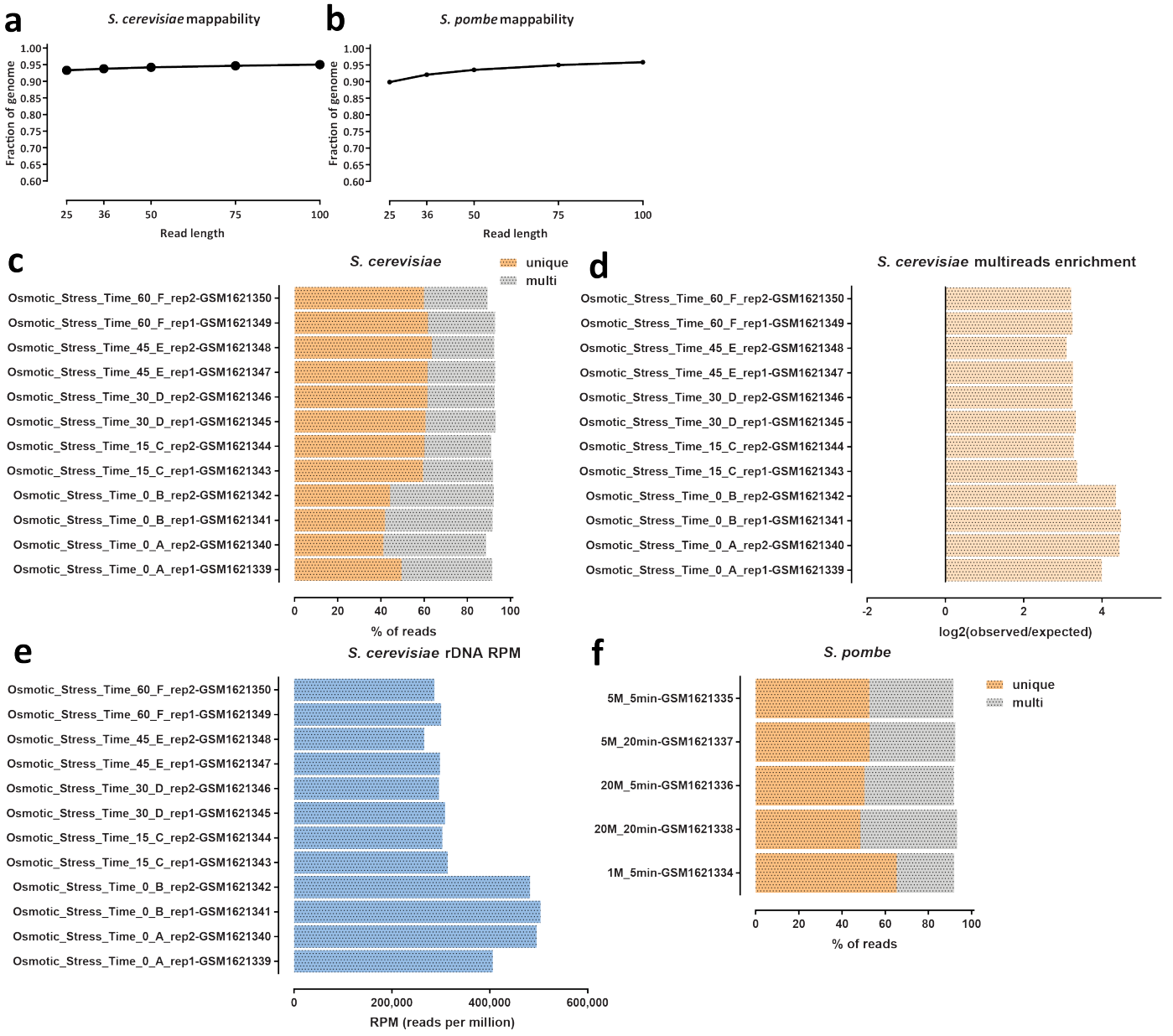

Supplementary Figure 68: Ribosomal DNA arrays are highly enriched for chromatin accessibility as measured by ATAC-seq. (a) Unique read mappability of the *Saccharomyces cerevisiae* genome as a function of read length (b) Unique read mappability of the *Schizosaccharomyces pombe* genome as a function of read length (c and d) Enrichment of multimapping reads in *Saccharomyces cerevisiae* ATAC-seq datasets (e) ATAC-seq multireads are highly enriched for rDNA-mapping reads (f) Enrichment of multimapping reads in *Schizosaccharomyces pombe* ATAC-seq datasets ATAC-seq datasets were obtained from Schep et al. 2015 [53]

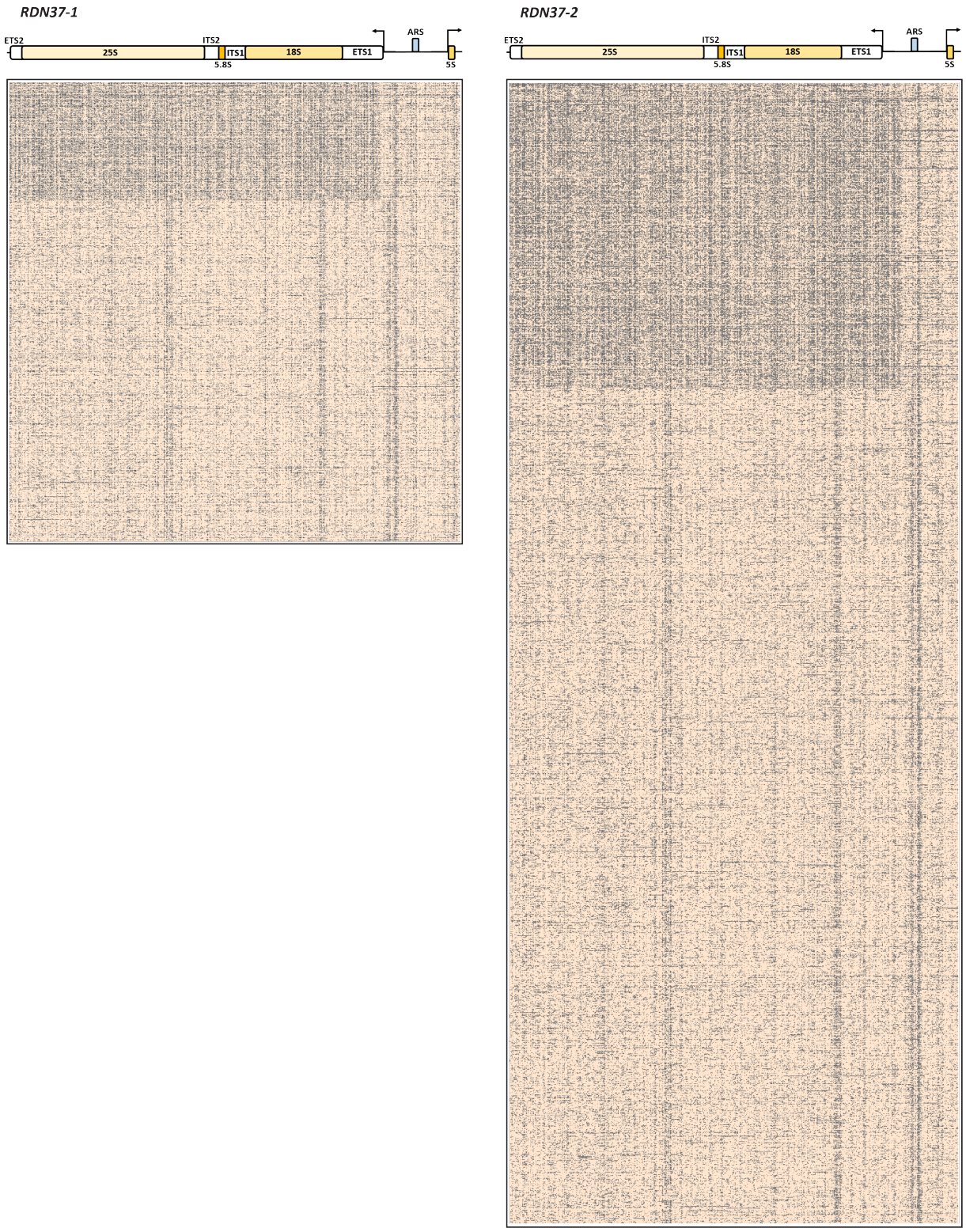

Supplementary Figure 69: SMAC-seq reveals the distribution of alternative chromatin states of rDNA arrays. Shown are all reads covering the *RDN37-1* and *RDN37-2* arrays in the *RDN1* locus in the "diamide 30 min rep1" experiment (unfiltered reads, "aggregate" signal).

RDN37-1

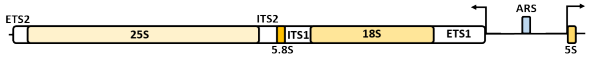

RDN37-2

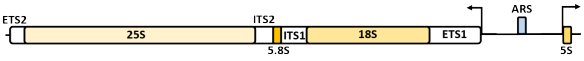

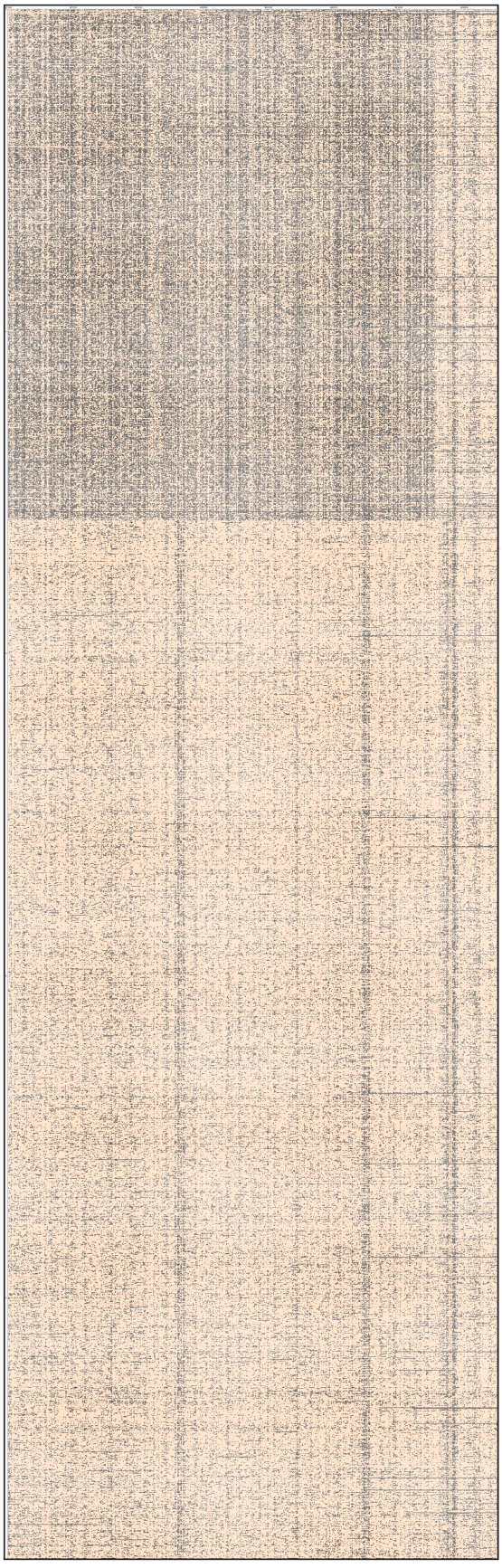

Supplementary Figure 70 ***(preceding page)*****: SMAC-seq reveals the distribution of alternative chromatin states of rDNA arrays. Shown are all reads covering the *RDN37-1* and *RDN37-2* arrays in the *RDN1* locus in the "diamide 60 min rep1" experiment (unfiltered reads, "aggregate" signal).**

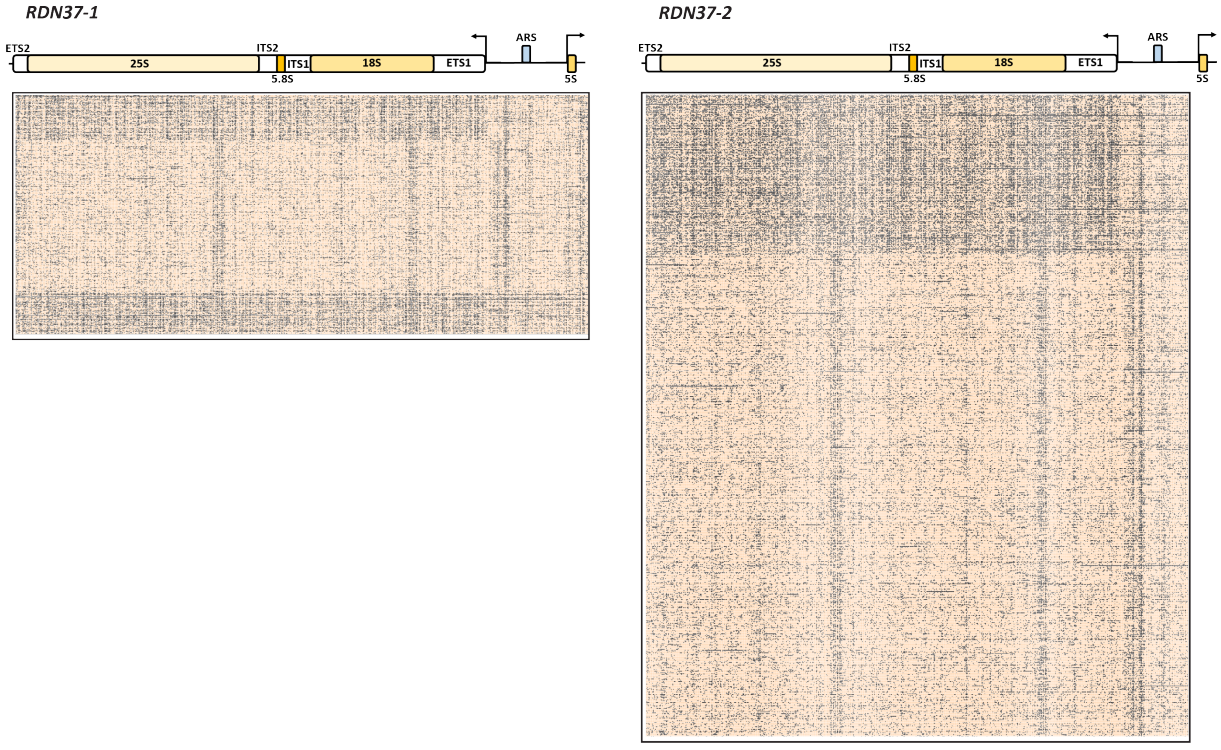

Supplementary Figure 71: SMAC-seq reveals the distribution of alternative chromatin states of rDNA arrays. Shown are all reads covering the *RDN37-1* and *RDN37-2* arrays in the *RDN1* locus in the "diamide 0 min rep1" experiment (unfiltered reads, "aggregate" signal).

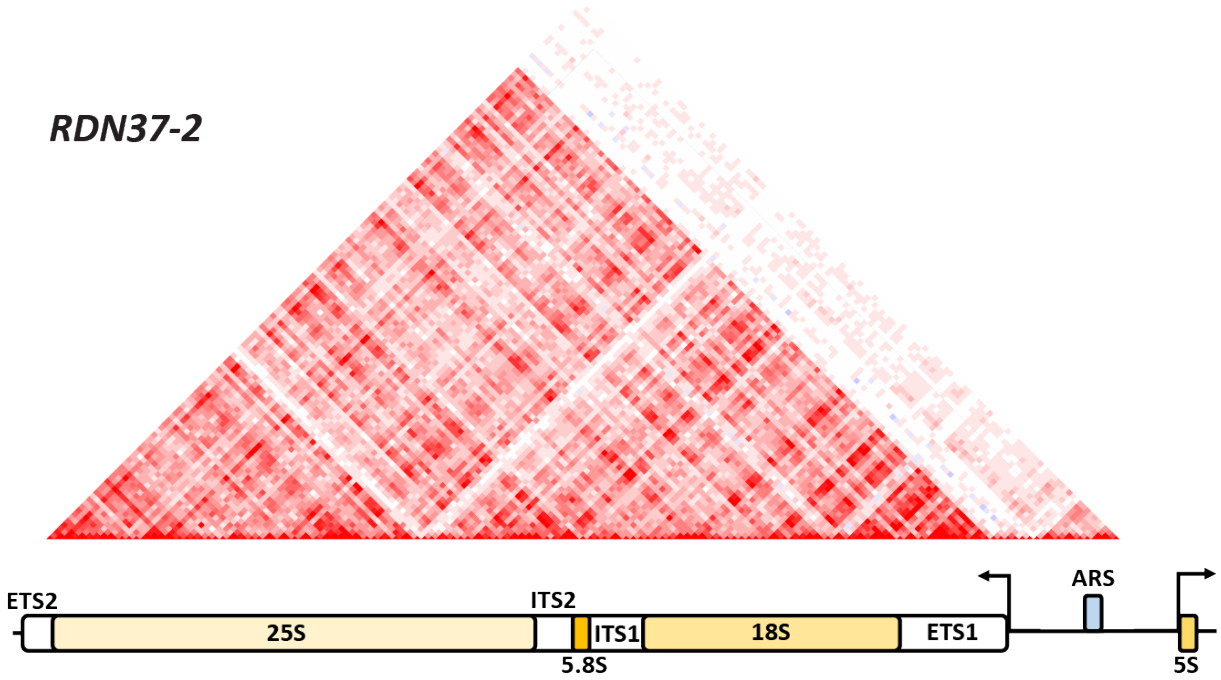

Supplementary Figure 72: NMI profile for the *RDN37-2* array, as in Figure 3b.

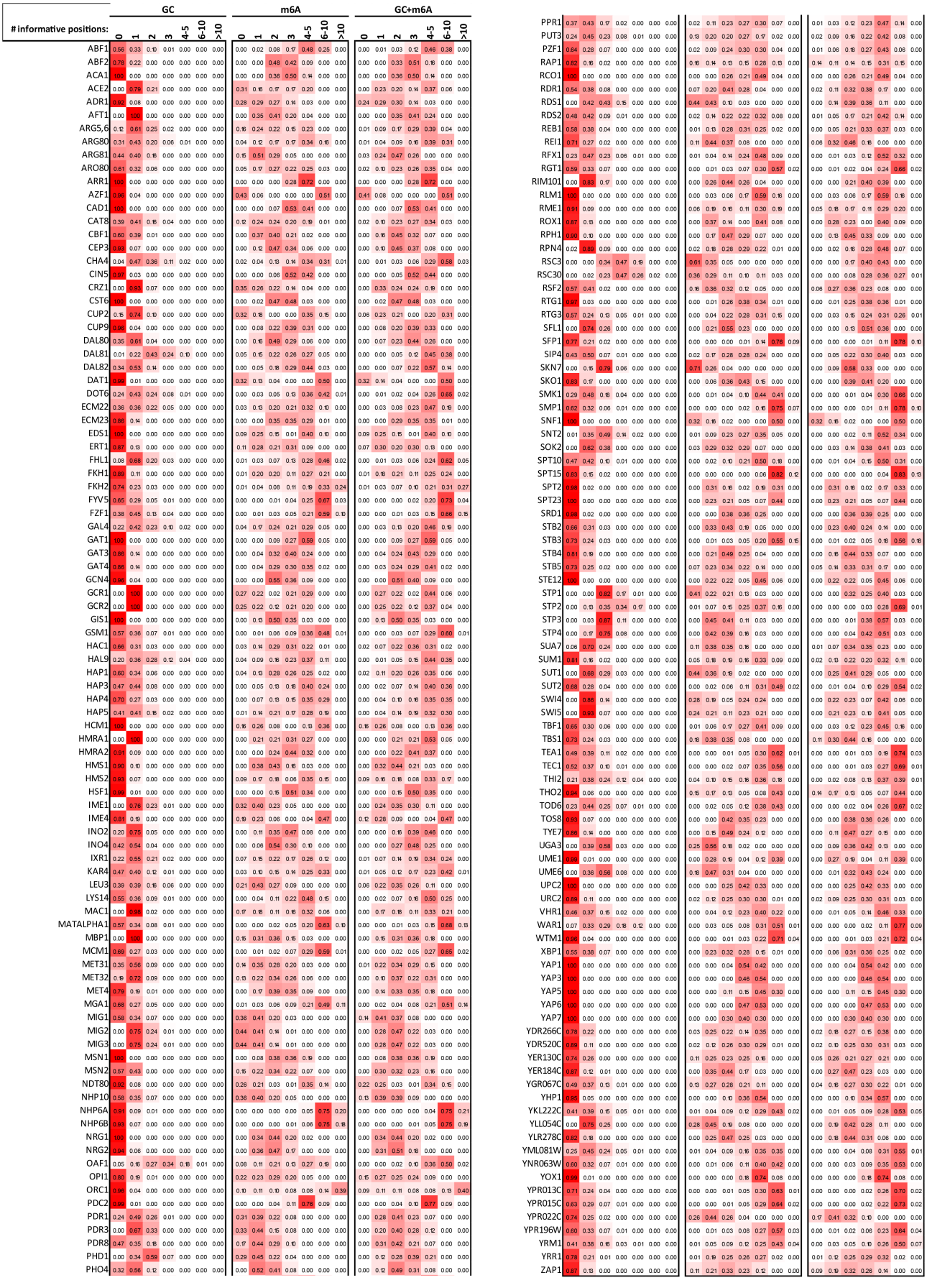
GC
m6A
GC+m6A
informative positions:
0 1 2 3 4-5 6-10 >10
ABF1 0.56 0.33 0.10 0.01 0.00 0.00 0.00
ABF2 0.78 0.22 0.00 0.00 0.00 0.00 0.00
ACA1 1.00 0.00 0.00 0.00 0.00 0.00 0.00
ACE2 0.00 0.79 0.21 0.00 0.00 0.00 0.00
ADR1 0.92 0.08 0.00 0.00 0.00 0.00 0.00
AFT1 0.00 1.00 0.00 0.00 0.00 0.00 0.00
ARG5,6 0.12 0.61 0.25 0.02 0.00 0.00 0.00
ARG80 0.31 0.43 0.20 0.06 0.01 0.00 0.00
ARG81 0.44 0.40 0.16 0.00 0.00 0.00 0.00
ARO80 0.61 0.32 0.06 0.00 0.00 0.00 0.00
ARR1 1.00 0.00 0.00 0.00 0.00 0.00 0.00
AZF1 0.96 0.04 0.00 0.00 0.00 0.00 0.00
CAD1 1.00 0.00 0.00 0.00 0.00 0.00 0.00
CAT8 0.39 0.41 0.16 0.04 0.00 0.00 0.00
CBF1 0.60 0.39 0.01 0.00 0.00 0.00 0.00
CEP3 0.93 0.07 0.00 0.00 0.00 0.00 0.00
CHA4 0.04 0.47 0.36 0.11 0.02 0.00 0.00
CIN5 0.97 0.03 0.00 0.00 0.00 0.00 0.00
CRZ1 0.00 0.93 0.07 0.00 0.00 0.00 0.00
CST6 1.00 0.00 0.00 0.00 0.00 0.00 0.00
CUP2 0.15 0.74 0.10 0.00 0.00 0.00 0.00
CUP9 0.96 0.04 0.00 0.00 0.00 0.00 0.00
DAL80 0.35 0.61 0.04 0.00 0.00 0.00 0.00
DAL81 0.01 0.22 0.43 0.24 0.10 0.00 0.00
DAL82 0.34 0.53 0.14 0.00 0.00 0.00 0.00
DAT1 0.99 0.01 0.00 0.00 0.00 0.00 0.00
DOT6 0.24 0.43 0.24 0.08 0.01 0.00 0.00
ECM22 0.36 0.36 0.22 0.05 0.00 0.00 0.00
ECM23 0.86 0.14 0.00 0.00 0.00 0.00 0.00
EDS1 1.00 0.00 0.00 0.00 0.00 0.00 0.00
ERT1 0.87 0.13 0.00 0.00 0.00 0.00 0.00
FHL1 0.08 0.68 0.20 0.03 0.00 0.00 0.00
FKH1 0.89 0.11 0.00 0.00 0.00 0.00 0.00
FKH2 0.74 0.23 0.03 0.00 0.00 0.00 0.00
FYV5 0.65 0.29 0.05 0.01 0.00 0.00 0.00
FZF1 0.38 0.45 0.13 0.04 0.00 0.00 0.00
GAL4 0.22 0.42 0.23 0.10 0.02 0.00 0.00
GAT1 1.00 0.00 0.00 0.00 0.00 0.00 0.00
GAT3 0.86 0.14 0.00 0.00 0.00 0.00 0.00
GAT4 0.86 0.14 0.00 0.00 0.00 0.00 0.00
GCN4 0.96 0.04 0.00 0.00 0.00 0.00 0.00
GCR1 0.00 1.00 0.00 0.00 0.00 0.00 0.00
GCR2 0.00 1.00 0.00 0.00 0.00 0.00 0.00
GIS1 1.00 0.00 0.00 0.00 0.00 0.00 0.00
GSM1 0.57 0.36 0.07 0.01 0.00 0.00 0.00
HAC1 0.66 0.31 0.03 0.00 0.00 0.00 0.00
HAL9 0.20 0.36 0.28 0.12 0.04 0.00 0.00
HAP1 0.60 0.34 0.06 0.00 0.00 0.00 0.00
HAP3 0.47 0.44 0.08 0.00 0.00 0.00 0.00
HAP4 0.70 0.27 0.03 0.00 0.00 0.00 0.00
HAP5 0.41 0.41 0.16 0.02 0.00 0.00 0.00
HCM1 1.00 0.00 0.00 0.00 0.00 0.00 0.00
HMRA1 0.00 1.00 0.00 0.00 0.00 0.00 0.00
HMRA2 0.91 0.09 0.00 0.00 0.00 0.00 0.00
HMS1 0.90 0.10 0.00 0.00 0.00 0.00 0.00
HMS2 0.93 0.07 0.00 0.00 0.00 0.00 0.00
HSF1 0.99 0.01 0.00 0.00 0.00 0.00 0.00
IME1 0.00 0.76 0.23 0.01 0.00 0.00 0.00
IME4 0.81 0.19 0.00 0.00 0.00 0.00 0.00
INO2 0.20 0.75 0.05 0.00 0.00 0.00 0.00
INO4 0.42 0.54 0.04 0.00 0.00 0.00 0.00
IXR1 0.22 0.55 0.21 0.02 0.00 0.00 0.00
KAR4 0.47 0.40 0.12 0.01 0.00 0.00 0.00
LEU3 0.39 0.39 0.16 0.06 0.00 0.00 0.00
LYS14 0.55 0.36 0.09 0.01 0.00 0.00 0.00
MAC1 0.00 0.98 0.02 0.00 0.00 0.00 0.00
MATALPHA1 0.57 0.34 0.08 0.01 0.00 0.00 0.00
MBP1 0.00 1.00 0.00 0.00 0.00 0.00 0.00
MCM1 0.69 0.27 0.03 0.00 0.00 0.00 0.00
MET31 0.35 0.56 0.09 0.00 0.00 0.00 0.00
MET32 0.19 0.72 0.09 0.00 0.00 0.00 0.00
MET4 0.79 0.19 0.01 0.00 0.00 0.00 0.00
MGA1 0.68 0.27 0.05 0.00 0.00 0.00 0.00
MIG1 0.58 0.34 0.07 0.00 0.00 0.00 0.00
MIG2 0.00 0.75 0.24 0.01 0.00 0.00 0.00
MIG3 0.00 0.75 0.24 0.01 0.00 0.00 0.00
MSN1 1.00 0.00 0.00 0.00 0.00 0.00 0.00
MSN2 0.57 0.43 0.00 0.00 0.00 0.00 0.00
NDT80 0.92 0.08 0.00 0.00 0.00 0.00 0.00
NHP10 0.58 0.35 0.07 0.00 0.00 0.00 0.00
NHP6A 0.91 0.09 0.01 0.00 0.00 0.00 0.00
NHP6B 0.93 0.07 0.00 0.00 0.00 0.00 0.00
NRG1 1.00 0.00 0.00 0.00 0.00 0.00 0.00
NRG2 0.94 0.06 0.00 0.00 0.00 0.00 0.00
OAF1 0.05 0.16 0.27 0.34 0.18 0.01 0.00
OPI1 0.80 0.19 0.01 0.00 0.00 0.00 0.00
ORC1 0.96 0.04 0.00 0.00 0.00 0.00 0.00
PDC2 0.99 0.01 0.00 0.00 0.00 0.00 0.00
PDR1 0.24 0.49 0.26 0.01 0.00 0.00 0.00
PDR3 0.00 0.67 0.33 0.00 0.00 0.00 0.00
PDR8 0.47 0.35 0.18 0.00 0.00 0.00 0.00
PHD1 0.00 0.34 0.59 0.07 0.00 0.00 0.00
PHO4 0.32 0.56 0.12 0.00 0.00 0.00 0.00
PPR1 0.37 0.43 0.17 0.02 0.00 0.00 0.00
PUT3 0.24 0.45 0.23 0.08 0.01 0.00 0.00
PZF1 0.84 0.28 0.07 0.00 0.00 0.00 0.00
RAP1 0.82 0.16 0.02 0.00 0.00 0.00 0.00
RCO1 1.00 0.00 0.00 0.00 0.00 0.00 0.00
RDR1 0.54 0.38 0.08 0.00 0.00 0.00 0.00
RDS1 0.00 0.42 0.43 0.15 0.00 0.00 0.00
RDS2 0.48 0.42 0.09 0.01 0.00 0.00 0.00
REB1 0.58 0.38 0.04 0.00 0.00 0.00 0.00
REI1 0.71 0.27 0.02 0.00 0.00 0.00 0.00
RFX1 0.23 0.47 0.23 0.06 0.01 0.00 0.00
RGT1 0.59 0.33 0.07 0.00 0.00 0.00 0.00
RIM101 0.00 0.83 0.17 0.00 0.00 0.00 0.00
RLM1 1.00 0.00 0.00 0.00 0.00 0.00 0.00
RME1 0.91 0.09 0.00 0.00 0.00 0.00 0.00
ROX1 0.87 0.13 0.00 0.00 0.00 0.00 0.00
RPH1 0.90 0.10 0.00 0.00 0.00 0.00 0.00
RPN4 0.02 0.89 0.09 0.00 0.00 0.00 0.00
RSC3 0.00 0.00 0.34 0.47 0.19 0.00 0.00
RSC30 0.00 0.00 0.23 0.47 0.28 0.02 0.00
RSF2 0.57 0.41 0.02 0.00 0.00 0.00 0.00
RTG1 0.97 0.03 0.00 0.00 0.00 0.00 0.00
RTG3 0.57 0.24 0.13 0.05 0.01 0.00 0.00
SFL1 0.00 0.74 0.26 0.00 0.00 0.00 0.00
SFP1 0.77 0.21 0.02 0.00 0.00 0.00 0.00
SIP4 0.43 0.50 0.07 0.01 0.00 0.00 0.00
SKN7 0.00 0.15 0.79 0.06 0.00 0.00 0.00
SKO1 0.83 0.17 0.00 0.00 0.00 0.00 0.00
SMK1 0.29 0.48 0.18 0.04 0.00 0.00 0.00
SMP1 0.62 0.32 0.06 0.01 0.00 0.00 0.00
SNF1 1.00 0.00 0.00 0.00 0.00 0.00 0.00
SNT2 0.01 0.35 0.49 0.14 0.02 0.00 0.00
SOK2 0.00 0.62 0.38 0.00 0.00 0.00 0.00
SPT10 0.47 0.42 0.10 0.01 0.00 0.00 0.00
SPT15 0.83 0.15 0.02 0.00 0.00 0.00 0.00
SPT2 0.98 0.02 0.00 0.00 0.00 0.00 0.00
SPT23 1.00 0.00 0.00 0.00 0.00 0.00 0.00
SRD1 0.98 0.02 0.00 0.00 0.00 0.00 0.00
STB2 0.66 0.31 0.03 0.00 0.00 0.00 0.00
STB3 0.73 0.24 0.03 0.00 0.00 0.00 0.00
STB4 0.81 0.19 0.00 0.00 0.00 0.00 0.00
STB5 0.73 0.25 0.02 0.00 0.00 0.00 0.00
STE12 1.00 0.00 0.00 0.00 0.00 0.00 0.00
STP1 0.00 0.00 0.82 0.17 0.01 0.00 0.00
STP2 0.00 0.13 0.35 0.34 0.17 0.00 0.00
STP3 0.00 0.03 0.87 0.11 0.00 0.00 0.00
STP4 0.00 0.17 0.75 0.08 0.00 0.00 0.00
SUA7 0.06 0.70 0.24 0.00 0.00 0.00 0.00
SUM1 0.81 0.16 0.02 0.00 0.00 0.00 0.00
SUT1 0.00 0.68 0.29 0.03 0.00 0.00 0.00
SUT2 0.68 0.28 0.04 0.00 0.00 0.00 0.00
SWI4 0.00 0.86 0.14 0.00 0.00 0.00 0.00
SWI5 0.00 0.93 0.07 0.00 0.00 0.00 0.00
TBF1 0.65 0.30 0.06 0.00 0.00 0.00 0.00
TBS1 0.73 0.24 0.03 0.00 0.00 0.00 0.00
TEA1 0.49 0.39 0.11 0.02 0.00 0.00 0.00
TEC1 0.52 0.37 0.10 0.01 0.00 0.00 0.00
THI2 0.21 0.38 0.24 0.12 0.04 0.00 0.00
THO2 0.94 0.06 0.00 0.00 0.00 0.00 0.00
TOD6 0.23 0.44 0.25 0.07 0.01 0.00 0.00
TOS8 0.93 0.07 0.00 0.00 0.00 0.00 0.00
TYE7 0.86 0.14 0.00 0.00 0.00 0.00 0.00
UGA3 0.00 0.39 0.58 0.03 0.00 0.00 0.00
UME1 0.99 0.01 0.00 0.00 0.00 0.00 0.00
UME6 0.00 0.36 0.56 0.08 0.00 0.00 0.00
UPC2 1.00 0.00 0.00 0.00 0.00 0.00 0.00
URC2 0.89 0.11 0.00 0.00 0.00 0.00 0.00
VHR1 0.46 0.37 0.15 0.02 0.00 0.00 0.00
WAR1 0.07 0.33 0.29 0.18 0.12 0.00 0.00
WTM1 0.98 0.04 0.00 0.00 0.00 0.00 0.00
XBP1 0.55 0.38 0.07 0.00 0.00 0.00 0.00
YAP1 1.00 0.00 0.00 0.00 0.00 0.00 0.00
YAP3 1.00 0.00 0.00 0.00 0.00 0.00 0.00
YAP5 1.00 0.00 0.00 0.00 0.00 0.00 0.00
YAP6 1.00 0.00 0.00 0.00 0.00 0.00 0.00
YAP7 1.00 0.00 0.00 0.00 0.00 0.00 0.00
YDR266C 0.78 0.22 0.00 0.00 0.00 0.00 0.00
YDR520C 0.89 0.11 0.00 0.00 0.00 0.00 0.00
YER130C 0.74 0.26 0.00 0.00 0.00 0.00 0.00
YER184C 0.87 0.12 0.01 0.00 0.00 0.00 0.00
YGR067C 0.49 0.37 0.13 0.01 0.00 0.00 0.00
YHP1 0.95 0.05 0.00 0.00 0.00 0.00 0.00
YKL222C 0.41 0.39 0.15 0.05 0.01 0.00 0.00
YLL054C 0.00 0.75 0.25 0.00 0.00 0.00 0.00
YLR278C 0.82 0.18 0.00 0.00 0.00 0.00 0.00
YML081W 0.25 0.45 0.24 0.05 0.01 0.00 0.00
YNR063W 0.60 0.32 0.07 0.01 0.00 0.00 0.00
YOX1 0.99 0.01 0.00 0.00 0.00 0.00 0.00
YPR013C 0.71 0.24 0.04 0.00 0.00 0.00 0.00
YPR015C 0.63 0.29 0.07 0.01 0.00 0.00 0.00
YPR022C 0.74 0.25 0.02 0.00 0.00 0.00 0.00
YPR196W 0.60 0.33 0.07 0.01 0.00 0.00 0.00
YRM1 0.41 0.38 0.16 0.03 0.01 0.00 0.00
YRR1 0.78 0.21 0.01 0.00 0.00 0.00 0.00
ZAP1 0.87 0.13 0.00 0.00 0.00 0.00 0.00

Supplementary Figure 73 *(preceding page)*: The impact of the addition of m6A to SMAC-seq on assay resolution and the potential ability to footprint individual transcription factors. Shown is the fraction of motifs in the genome for each transcription factor in the yeast genome containing the indicated number of informative positions using GC alone, m6A alone, and GC + m6A methyltransferase.

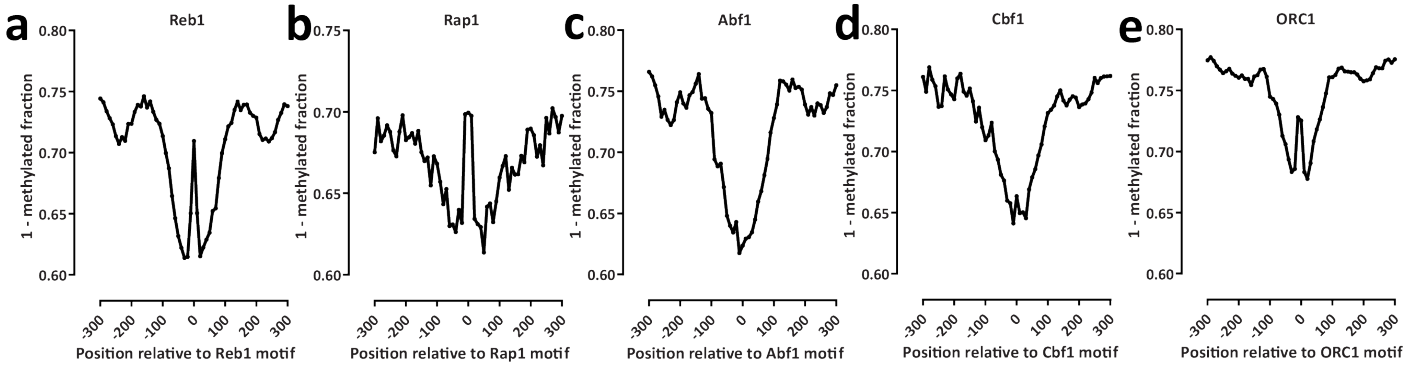

Supplementary Figure 74: Single-molecule footprinting by transcription factors. Shown is the average methylation status (averaged over 10bp) in the neighborhood of occupied (as measured by ChIP-exo or ChIP-seq) recognition motifs for several *S. cerevisiae* DNA binding proteins: (a) Reb1; (b) Rap1; (c) Abf1; (d) Cbf1. (e) ORC1. Strong footprinting is observed for Reb1, Rap1, and ORC1, while Abf1 and Cbf1 occupancy does not appear to be strongly protective against methylation.

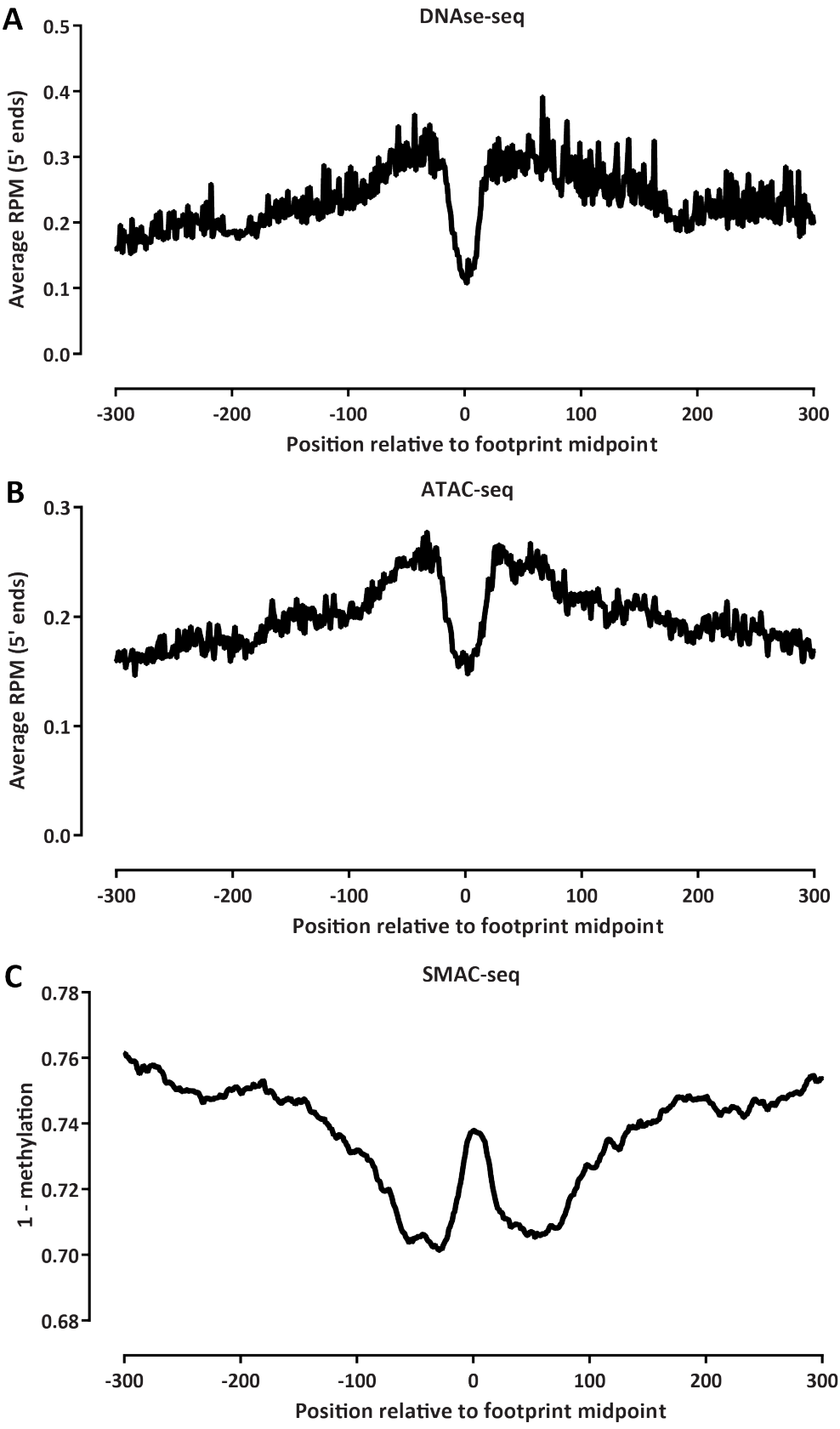

Supplementary Figure 75: Single-molecule footprinting by transcription factors. Shown is the average DNAse-seq (A) and ATAC-seq (B) cut profiles, and the SMAC-seq methylation profile (C) around DNAse footprints identified in yeast by Hesselbreth et al.[7].

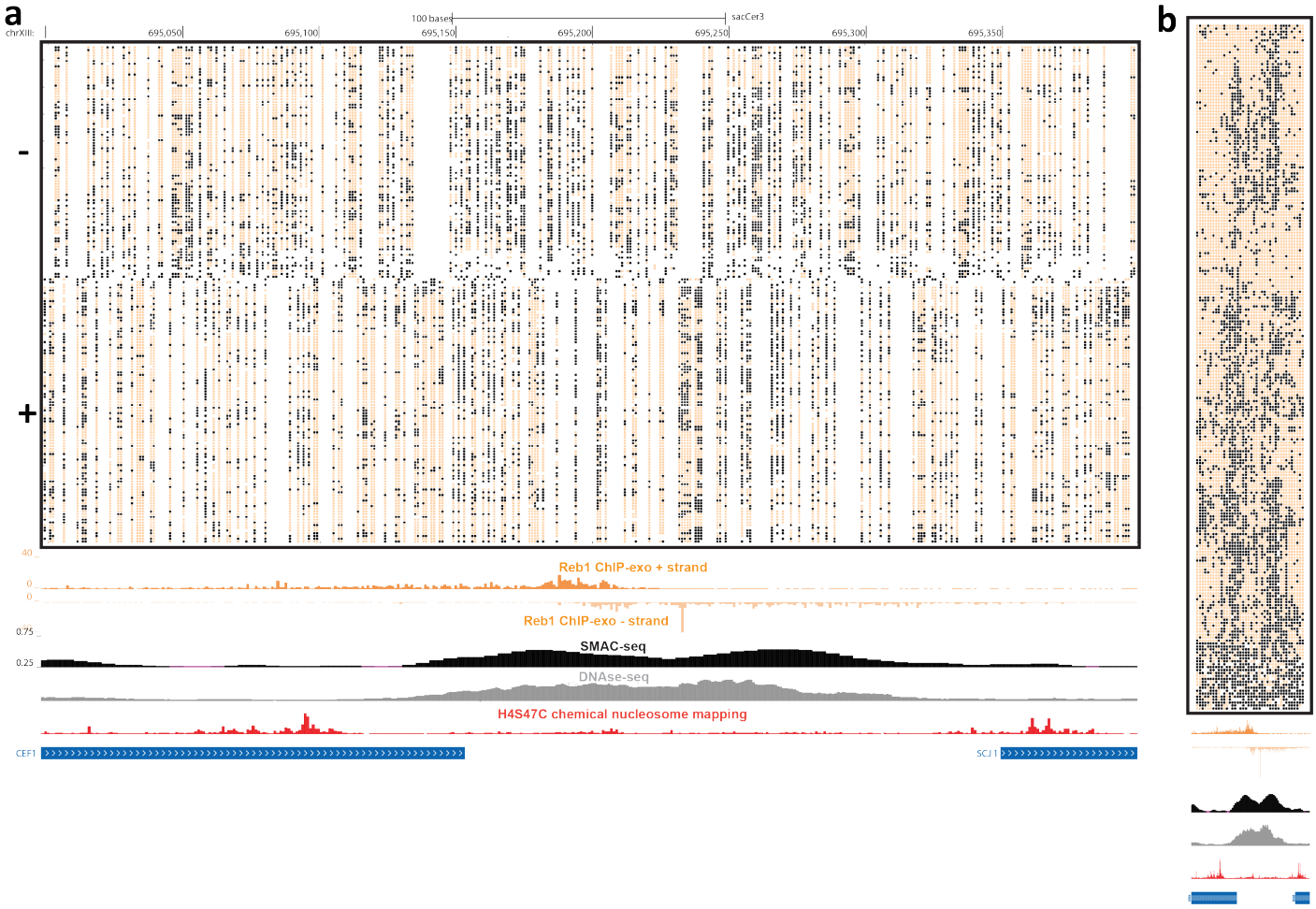

Supplementary Figure 76: Single-molecule footprinting by Reb1 binding sites. (a) Raw unfiltered nanopore reads fully spanning the 400-bp neighborhood of a Reb1 binding site on chrXVIII, at single-bp resolution. White spaces indicate positions for which there is no data (i.e. no CG, GC or A). (b) Same as in (a), but at aggregated 10-bp resolution.

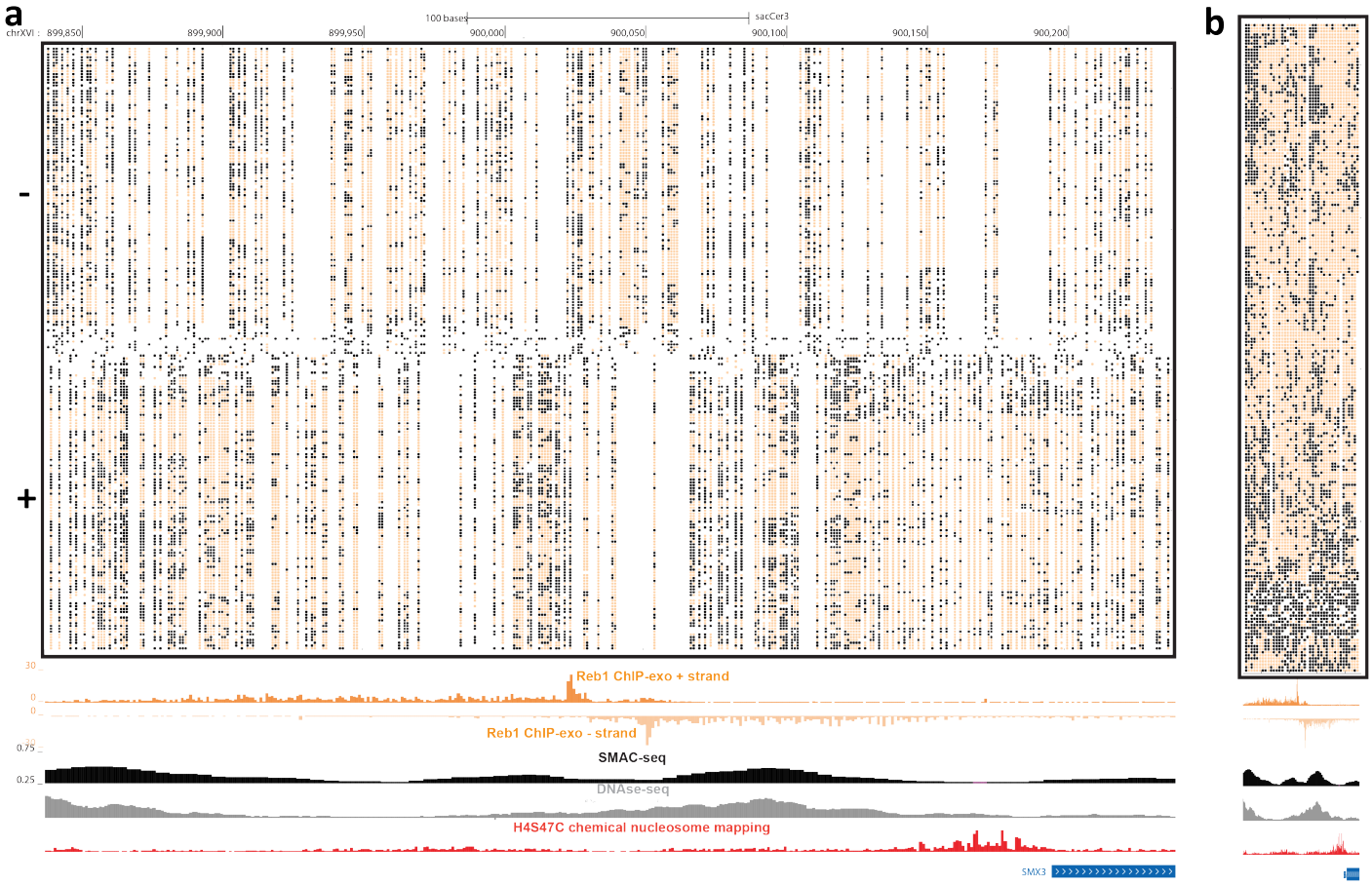

Supplementary Figure 77: Single-molecule footprinting by Reb1 binding sites. (a) Raw unfiltered nanopore reads fully spanning the 400-bp neighborhood of a Reb1 binding site on chrXVIII, at single-bp resolution. White spaces indicate positions for which there is no data (i.e. no CG, GC or A). (b) Same as in (a), but at aggregated 10-bp resolution.

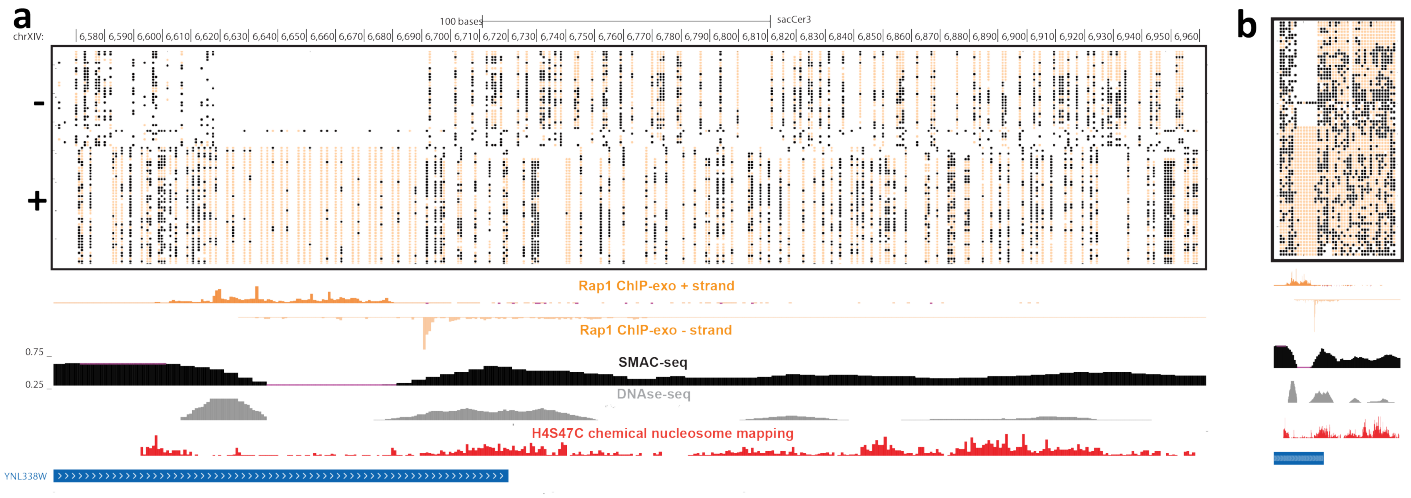

Supplementary Figure 78: Single-molecule footprinting associated with Rap1 occupancy. (a) Raw unfiltered nanopore reads fully spanning a 400-bp neighborhood of the subtelomeric region of chrXIV, at single-bp resolution. White spaces indicate positions for which there is no data (i.e. no CG, GC or A). (b) Same as in (a), but at aggregated 10-bp resolution.

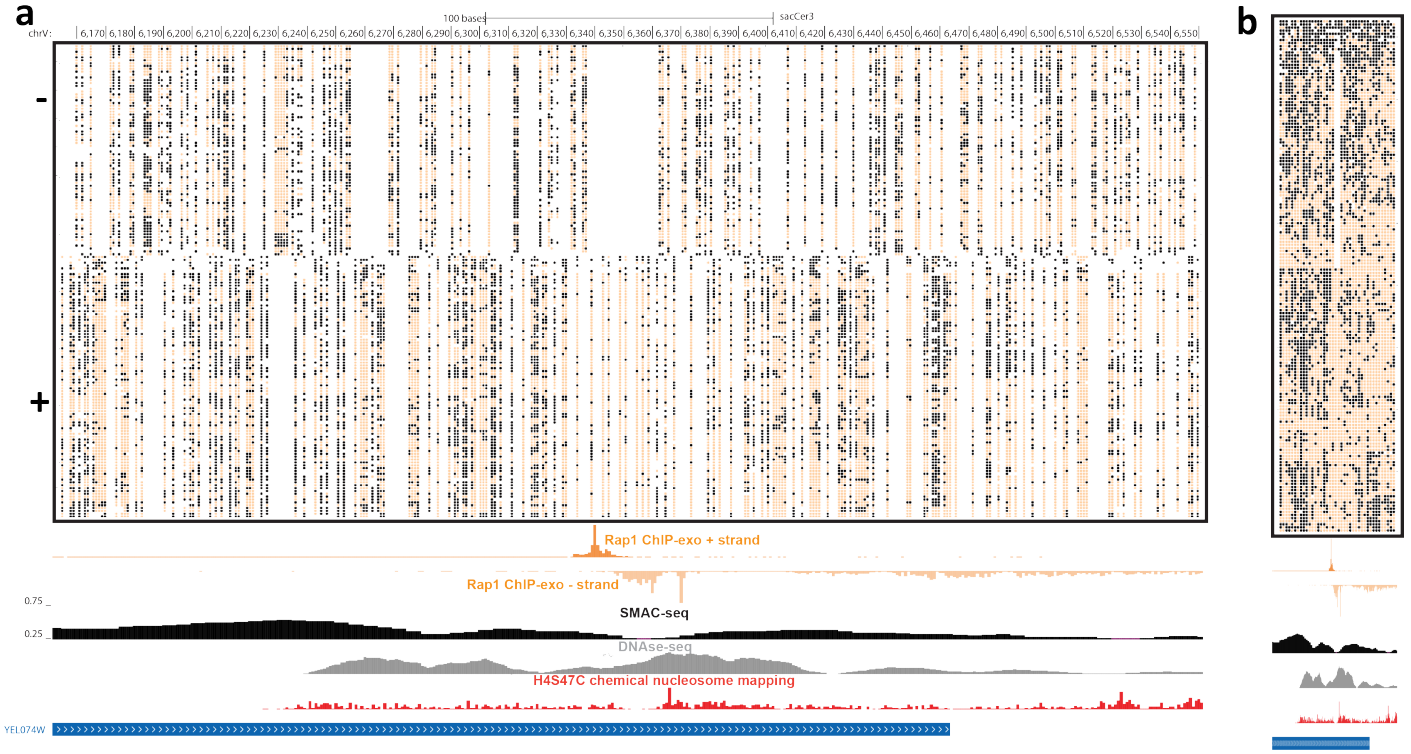

Supplementary Figure 79: Single-molecule footprinting associated with Rap1 occupancy. (a) Raw unfiltered nanopore reads fully spanning a 400-bp neighborhood of the subtelomeric region of chrXV, at single-bp resolution. White spaces indicate positions for which there is no data (i.e. no CG, GC or A). (b) Same as in (a), but at aggregated 10-bp resolution.

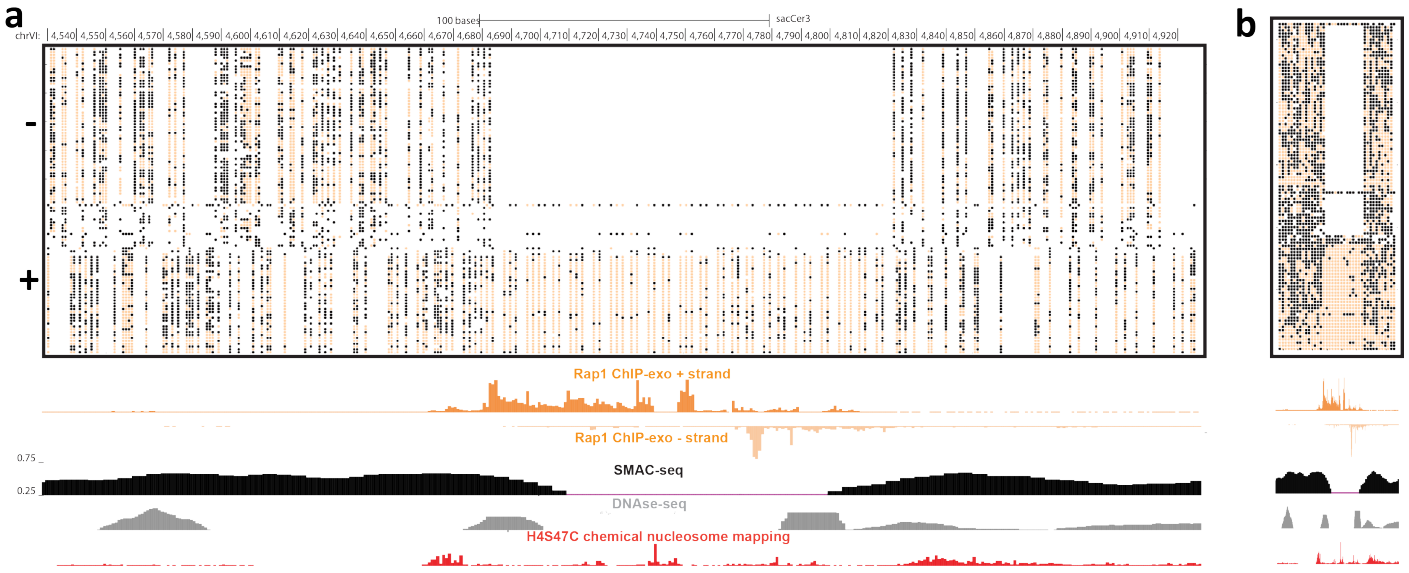

Supplementary Figure 80: Single-molecule footprinting associated with Rap1 occupancy. (a) Raw unfiltered nanopore reads fully spanning a 400-bp neighborhood of the subtelomeric region of chrVI, at single-bp resolution. White spaces indicate positions for which there is no data (i.e. no CG, GC or A). (b) Same as in (a), but at aggregated 10-bp resolution.

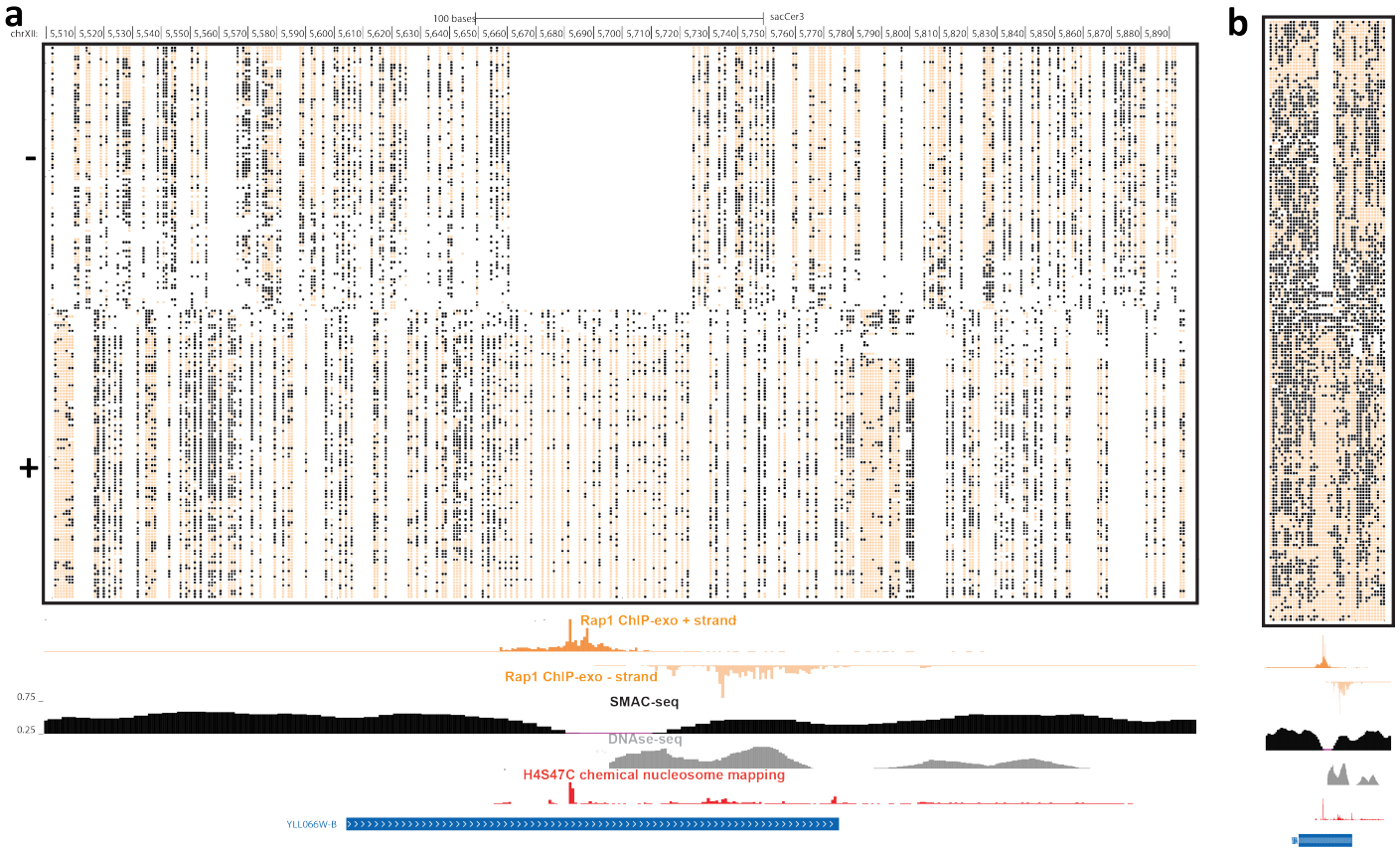

Supplementary Figure 81: Single-molecule footprinting associated with Rap1 occupancy. (a) Raw unfiltered nanopore reads fully spanning a 400-bp neighborhood of the subtelomeric region of chrXII, at single-bp resolution. White spaces indicate positions for which there is no data (i.e. no CG, GC or A). (b) Same as in (a), but at aggregated 10-bp resolution.

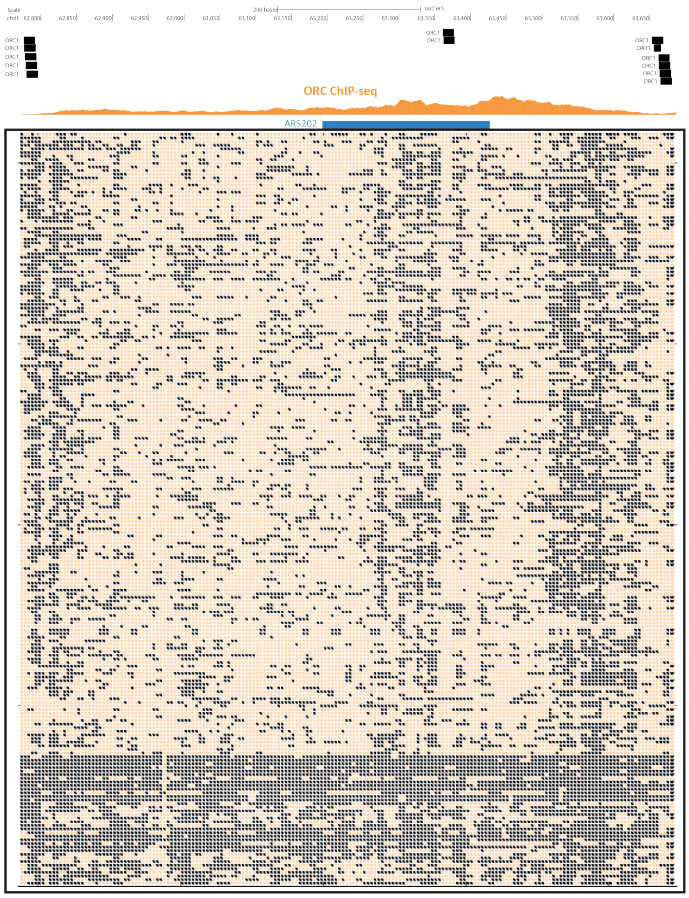

Supplementary Figure 82: Single-molecule footprinting associated with ORC occupancy. (a) Raw unfiltered nanopore reads fully spanning the neighborhood of an ARS site on chrII, at 5-bp aggregated resolution. White spaces indicate positions for which there is no data (i.e. no CG, GC or A).

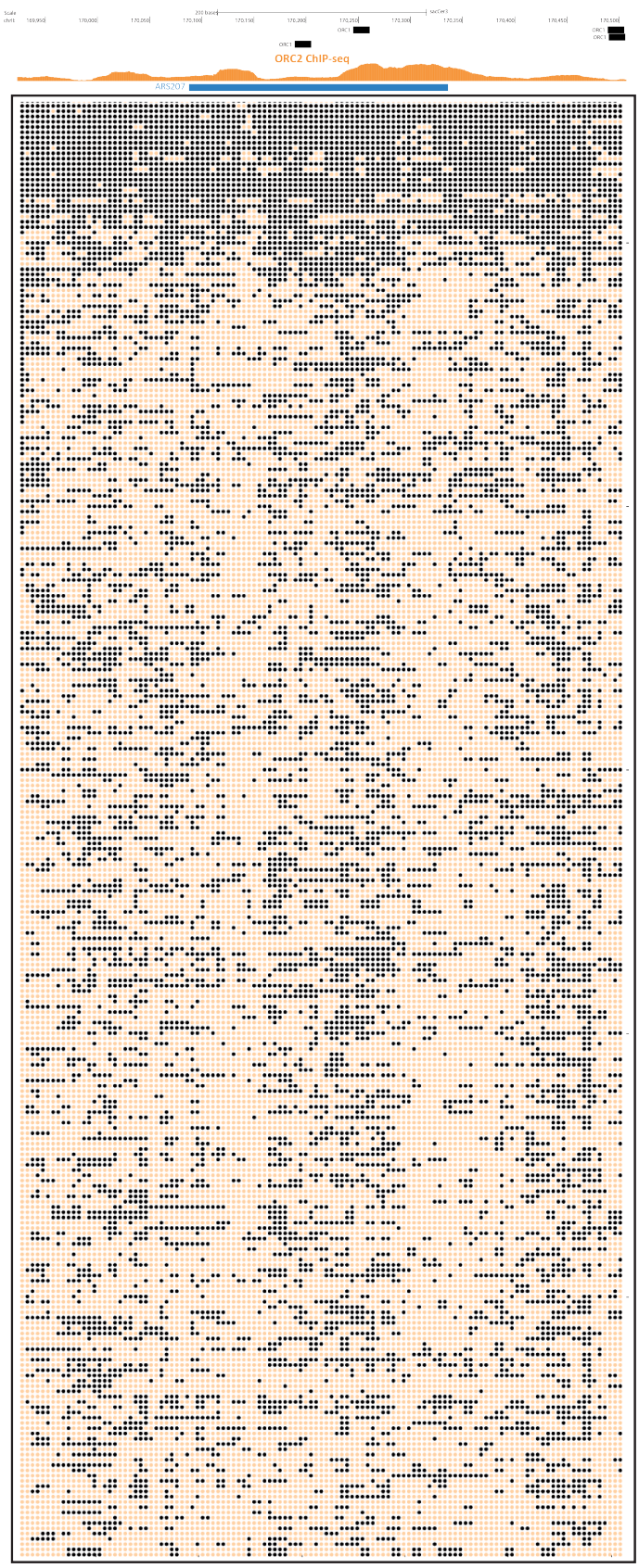

Supplementary Figure 83: Single-molecule footprinting associated with ORC occupancy. (a) Raw unfiltered nanopore reads fully spanning the neighborhood of an ARS site on chrII, at 5-bp aggregated resolution. White spaces indicate positions for which there is no data (i.e. no CG, GC or A).

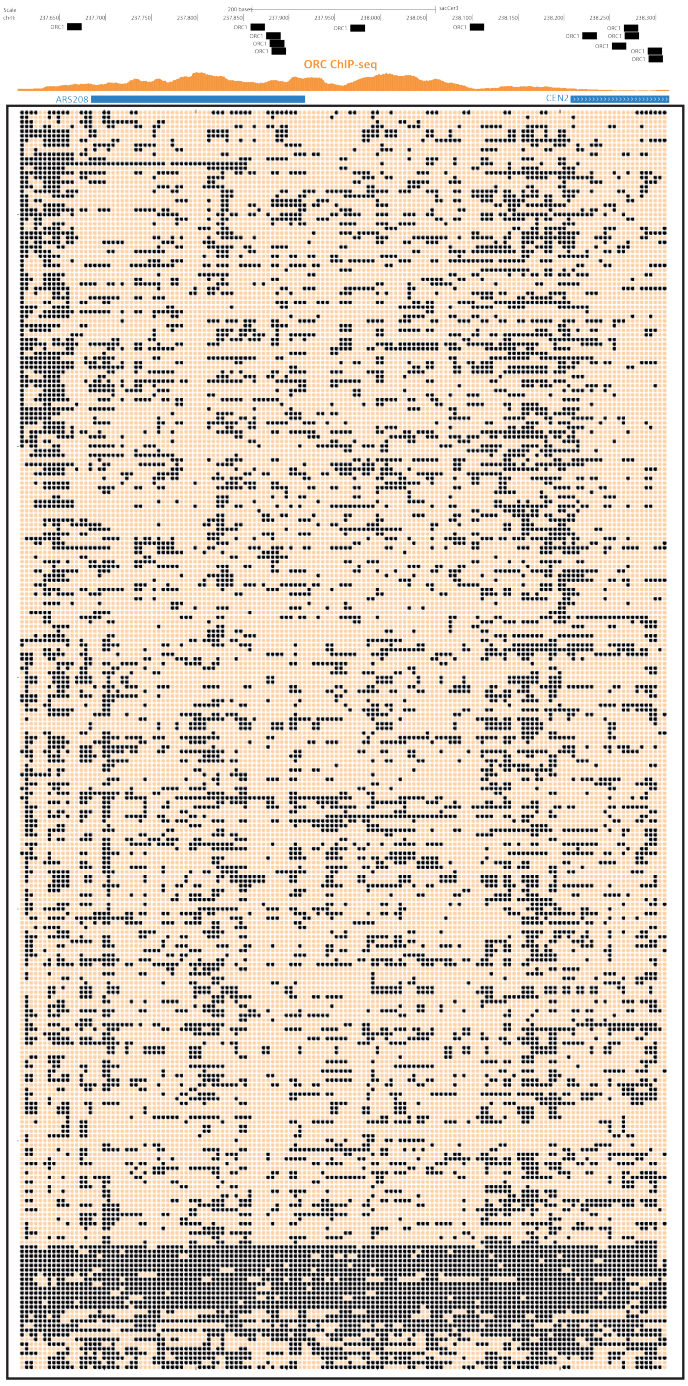

Supplementary Figure 84: Single-molecule footprinting associated with ORC occupancy. (a) Raw unfiltered nanopore reads fully spanning the neighborhood of an ARS site on chrII, at 5-bp aggregated resolution. White spaces indicate positions for which there is no data (i.e. no CG, GC or A).

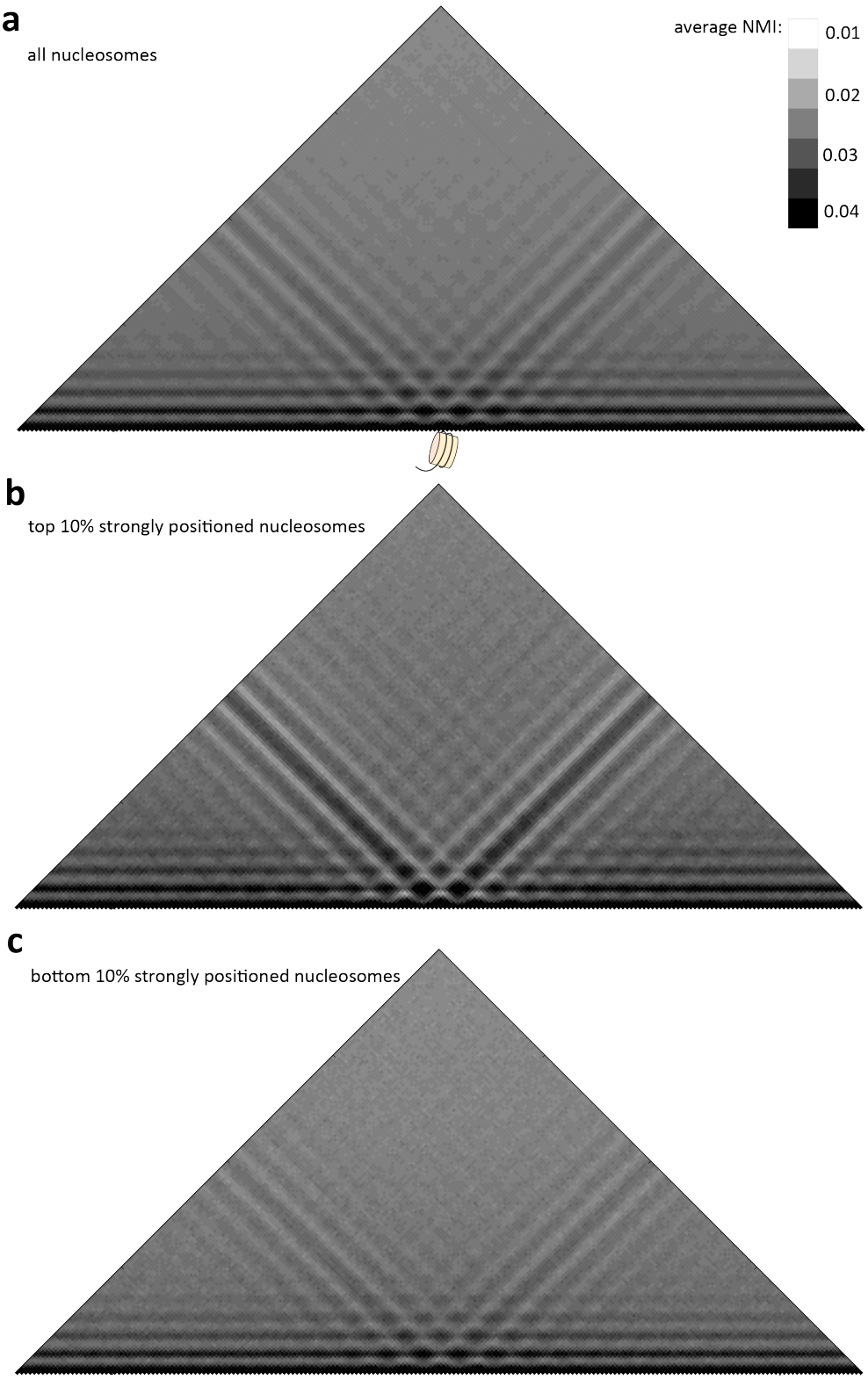

Supplementary Figure 85: Metanucleosome NMI profiles in the yeast genome. Shown are average NMI maps between all 20-bp segments centered on each positioned nucleosome in the genome (a), the top 10% strongly positioned nucleosomes (b), or the top 10% strongly positioned nucleosomes (c).

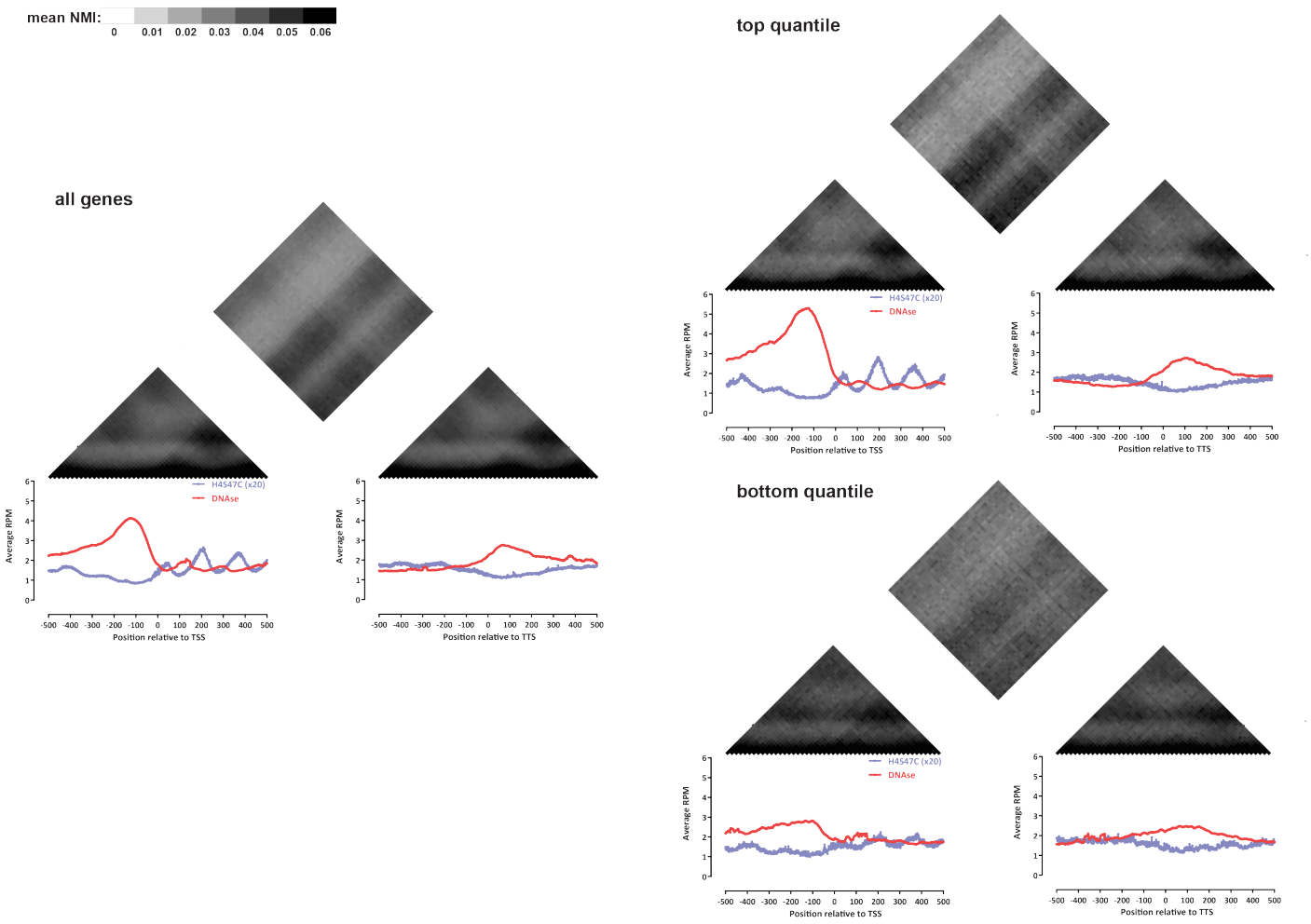

Supplementary Figure 86: Patterns of coaccessibility between the 5′ and 3′ ends of genes. Shown is the average NMI for the ±500bp regions in the 5′ and 3′ end of all yeast genes as well as the top and bottom 20% expression-ranked genes (calculated over 10-bp windows). Only genes ≥1000 bp in length are shown. Similar results are obtained using windows of size 20bp or 50bp (data not shown).

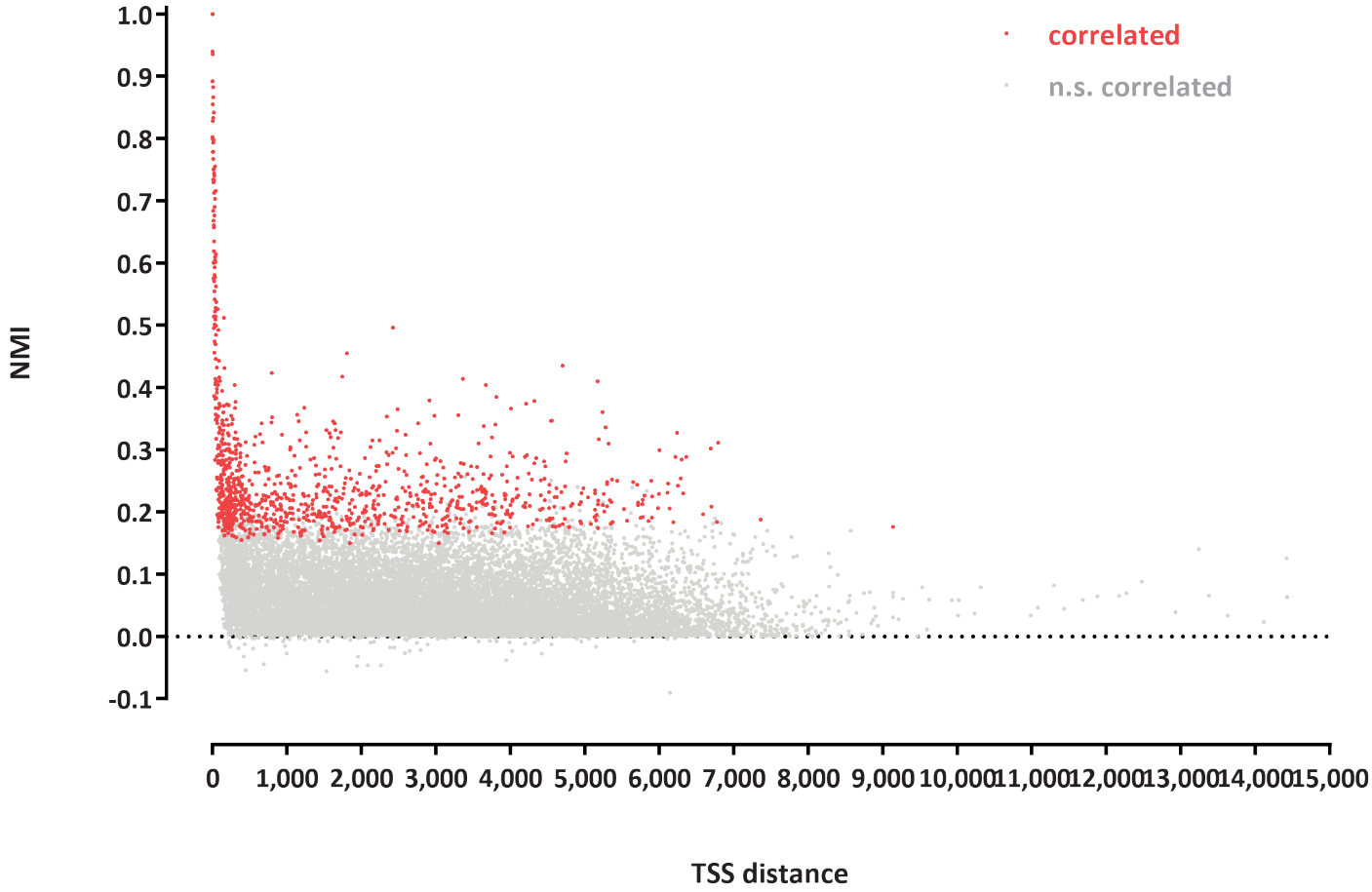

Supplementary Figure 87: Accessibility correlation between TSSs in the yeast genome. Shown are NMI values for each pair of significantly and non-significantly correlated TSSs (defined as the regions ±100 bp around the TSS).

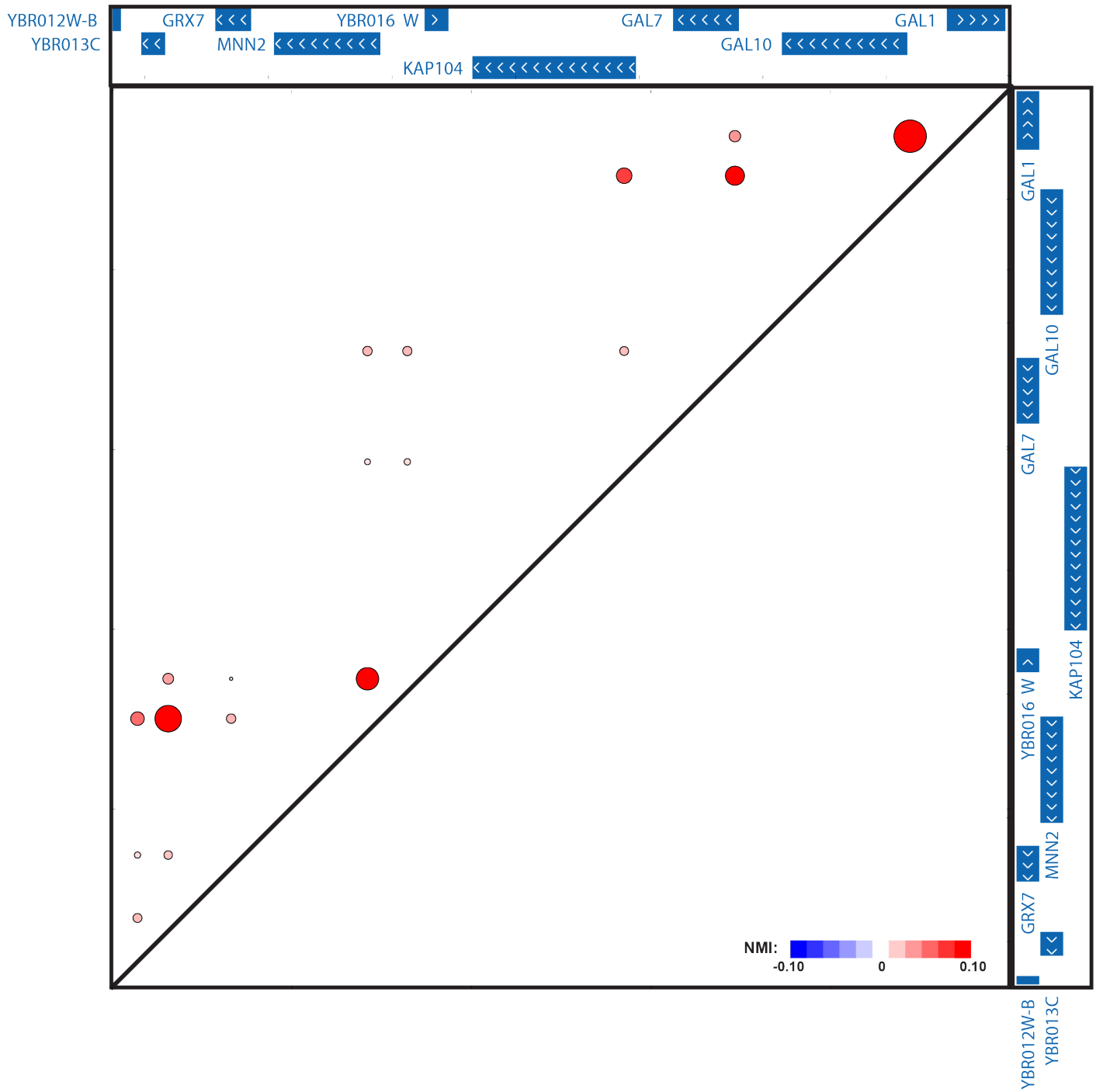

Supplementary Figure 88: Example of accessibility correlation between TSSs. Shown are accessibility correlations between all loci in the region with coordinates "chrII:265000-280000". The size and color of the dots corresponds to their NMI scores.

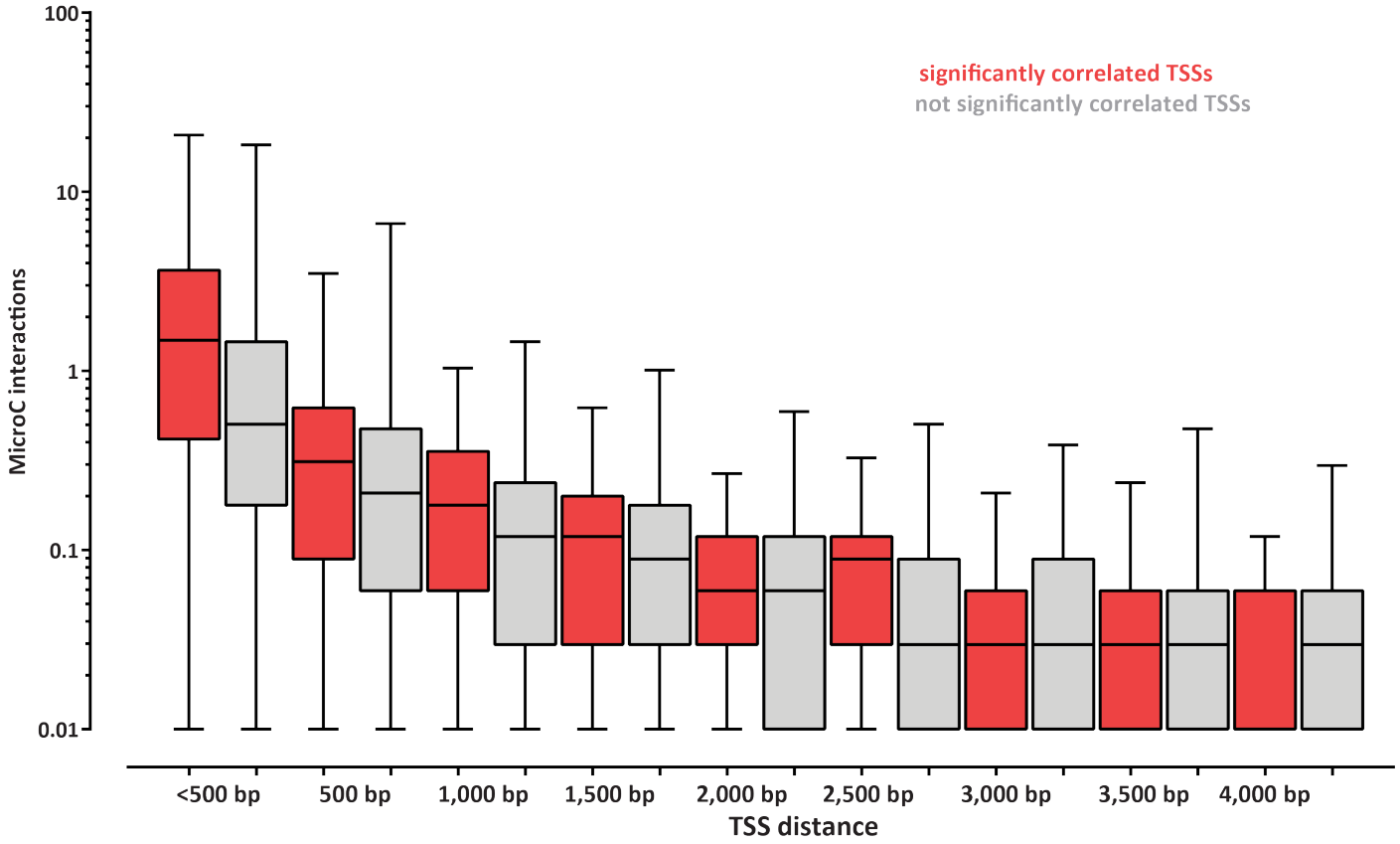

Supplementary Figure 89: Accessibility correlation between TSSs and 3D interactions. Shown are significantly and non-significantly correlated TSSs (defined as the regions ±100 bp around the TSS) split into distance bins and the number of 3D interactions between each group (measured by MicroC).

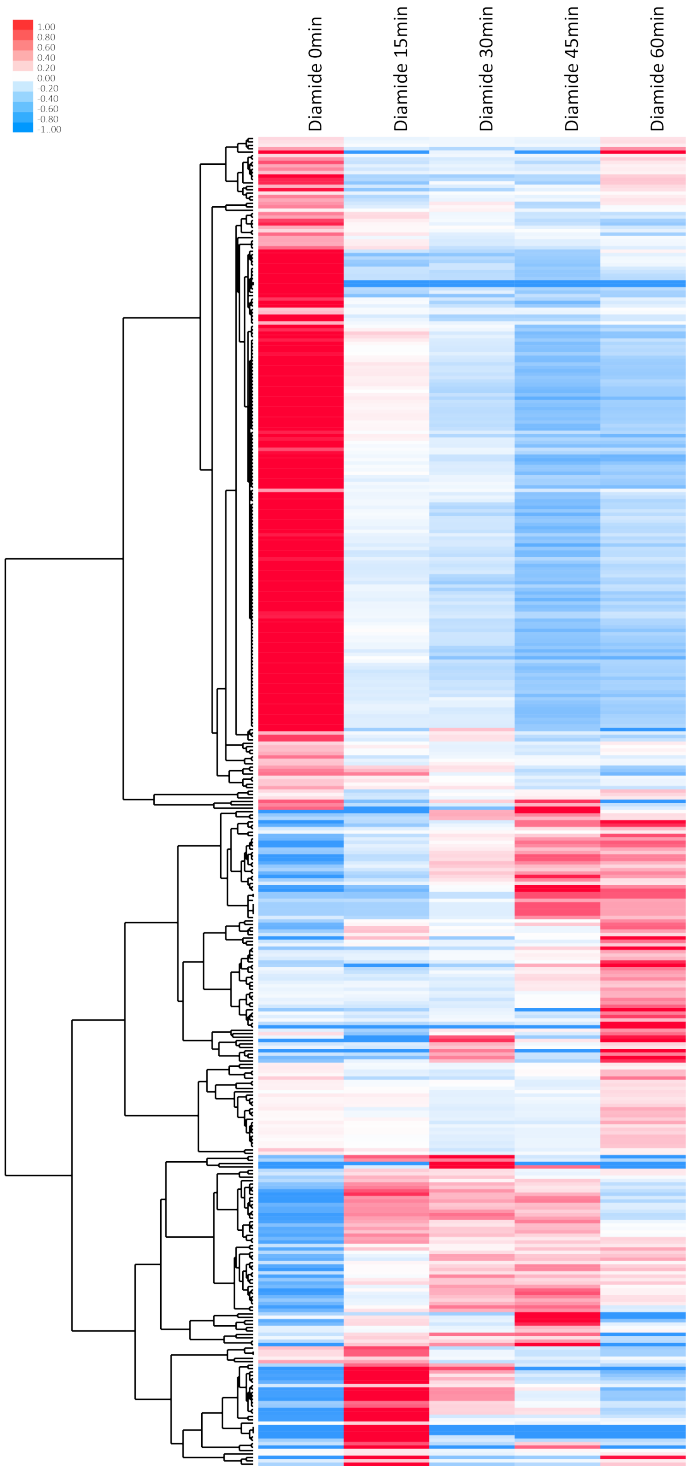

Supplementary Figure 90: Gene expression changes upon diamide treatment. Shown is RNA-seq data (mean and unit-variance normalized across time points) for all genes expressed at ≥50 FPKM in at least one time point.

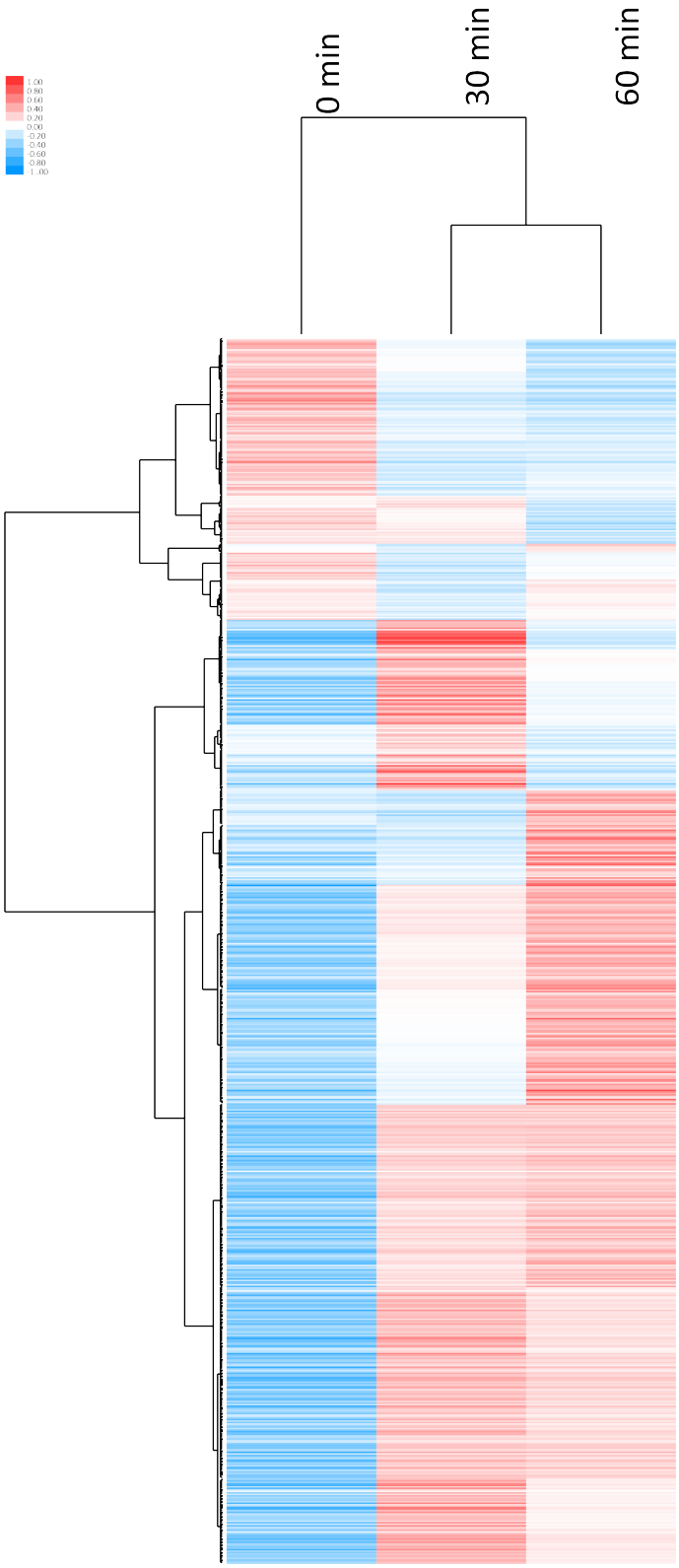

Supplementary Figure 91: Dynamic changes in HSF1 occupancy upon diamide treatment. Shown are ChIP-seq RPMs (mean and unit-variance normalized across time points) for all HSF1 peaks detected in least one time point.

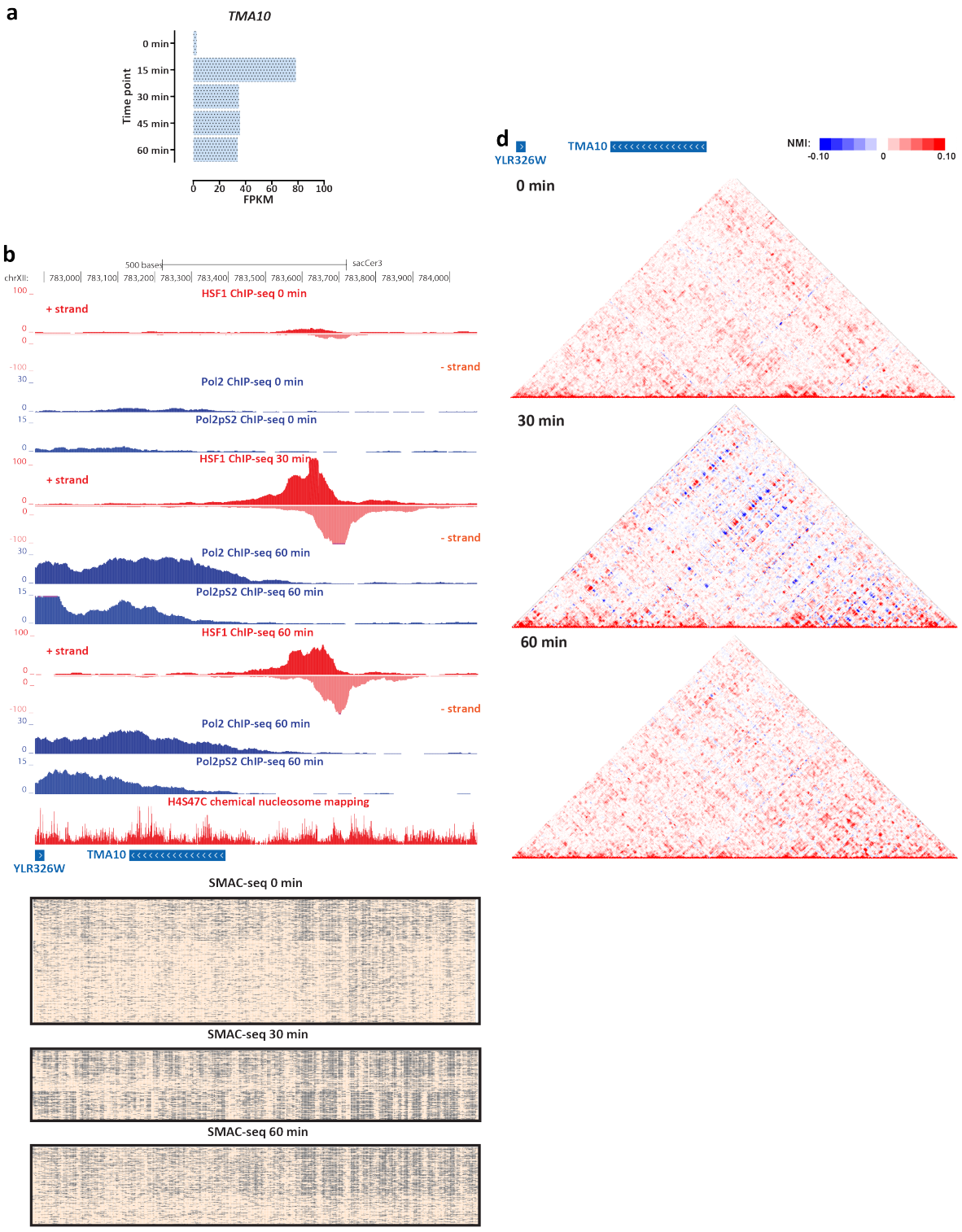

Supplementary Figure 92: Coordinated changes in chromatin accessibility and nucleosomal occupancy during the yeast stress response. Shown are changes in RNA Polymerase and HSF1 occupancy (measured by ChIP-seq), SMAC-seq profiles (1-bp resolution, 10-bp aggregate scores) and NMI profiles in the vicinity of the *TMA10* gene.

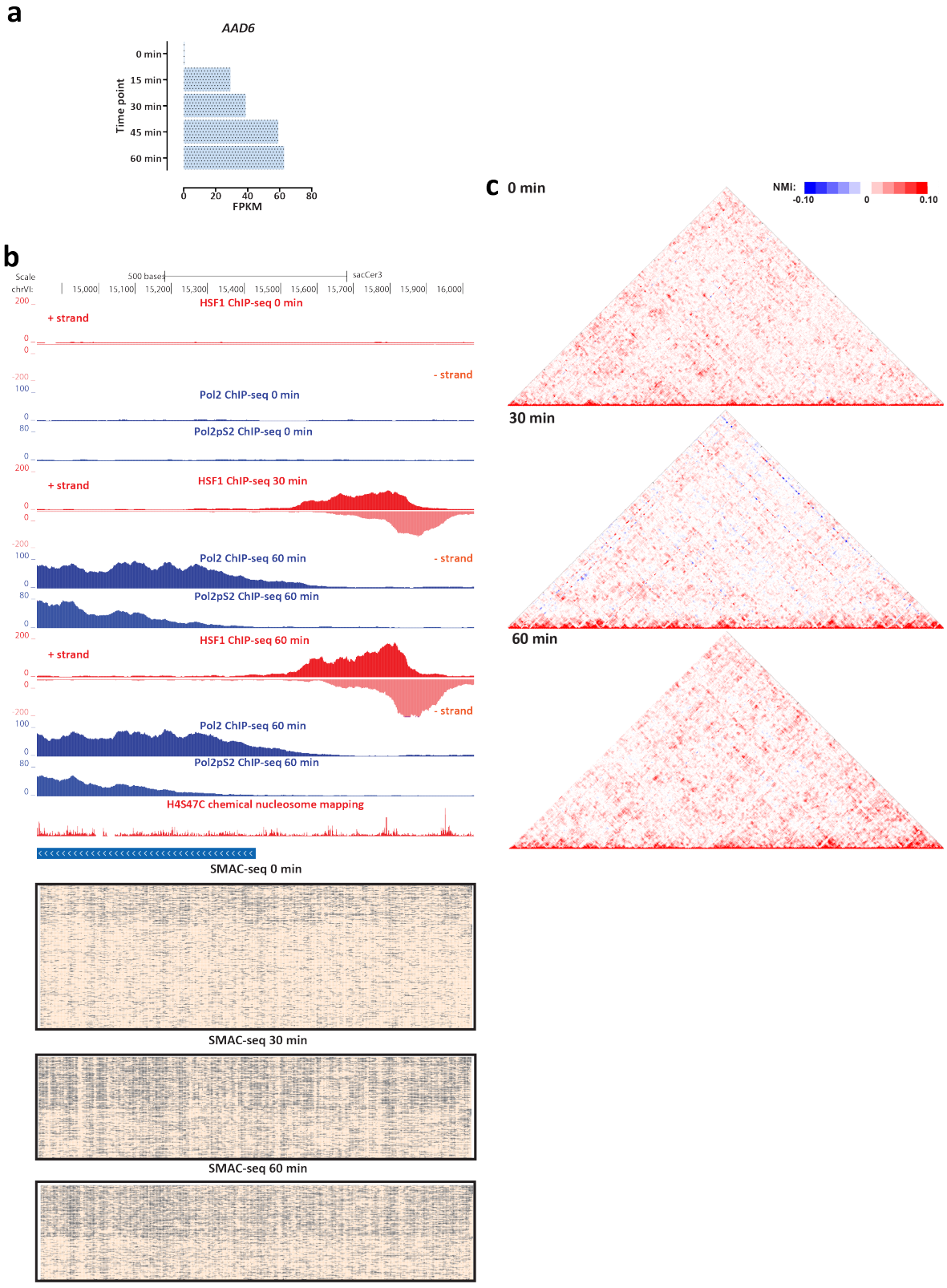

Supplementary Figure 93: Coordinated changes in chromatin accessibility and nucleosomal occupancy during the yeast stress response. Shown are changes in RNA Polymerase and HSF1 occupancy (measured by ChIP-seq), SMAC-seq profiles (1-bp resolution, 10-bp aggregate scores) and NMI profiles in the vicinity of the *AAD6* gene.

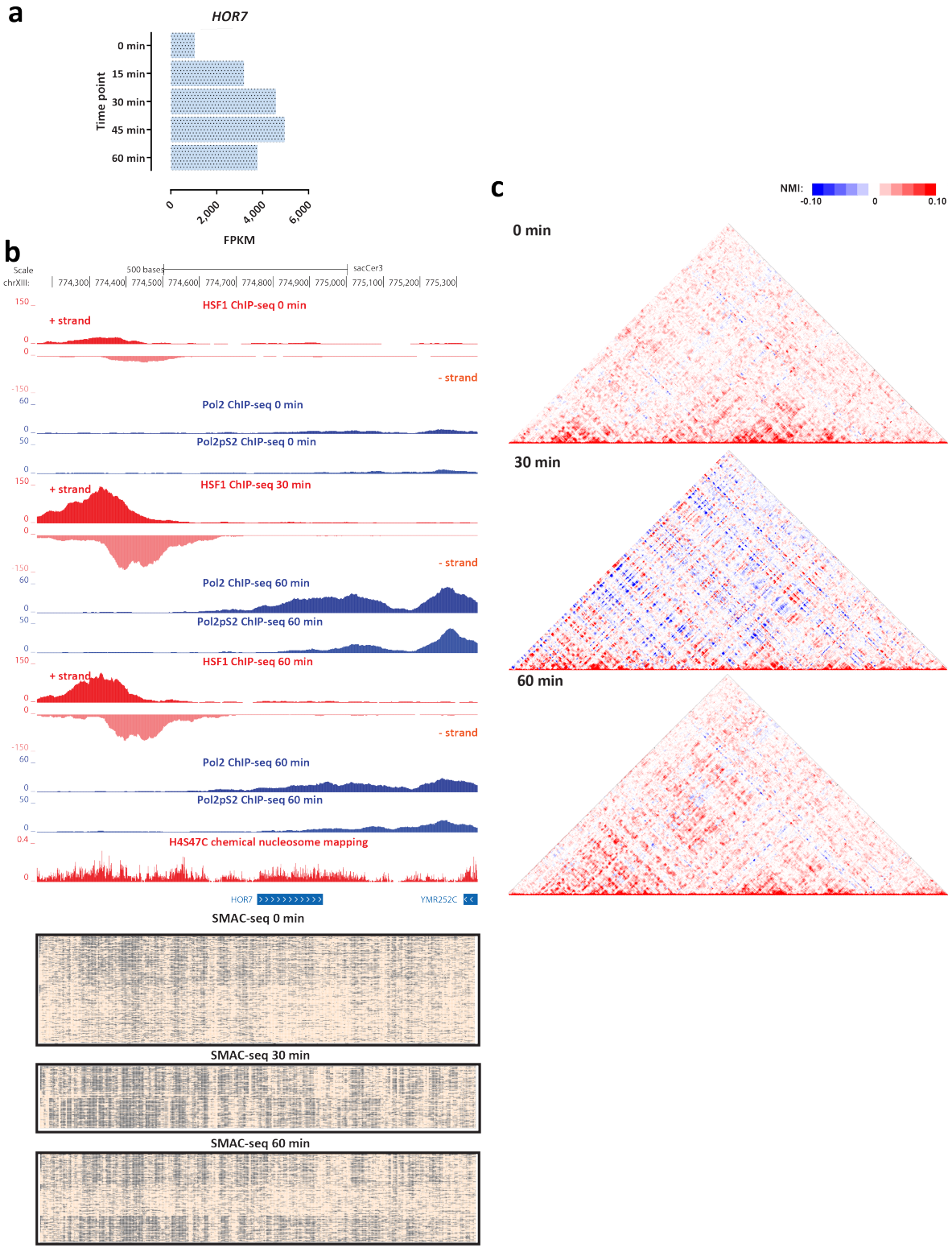

Supplementary Figure 94: Coordinated changes in chromatin accessibility and nucleosomal occupancy during the yeast stress response. Shown are changes in RNA Polymerase and HSF1 occupancy (measured by ChIP-seq), SMAC-seq profiles (1-bp resolution, 10-bp aggregate scores) and NMI profiles in the vicinity of the *HOR7* gene.

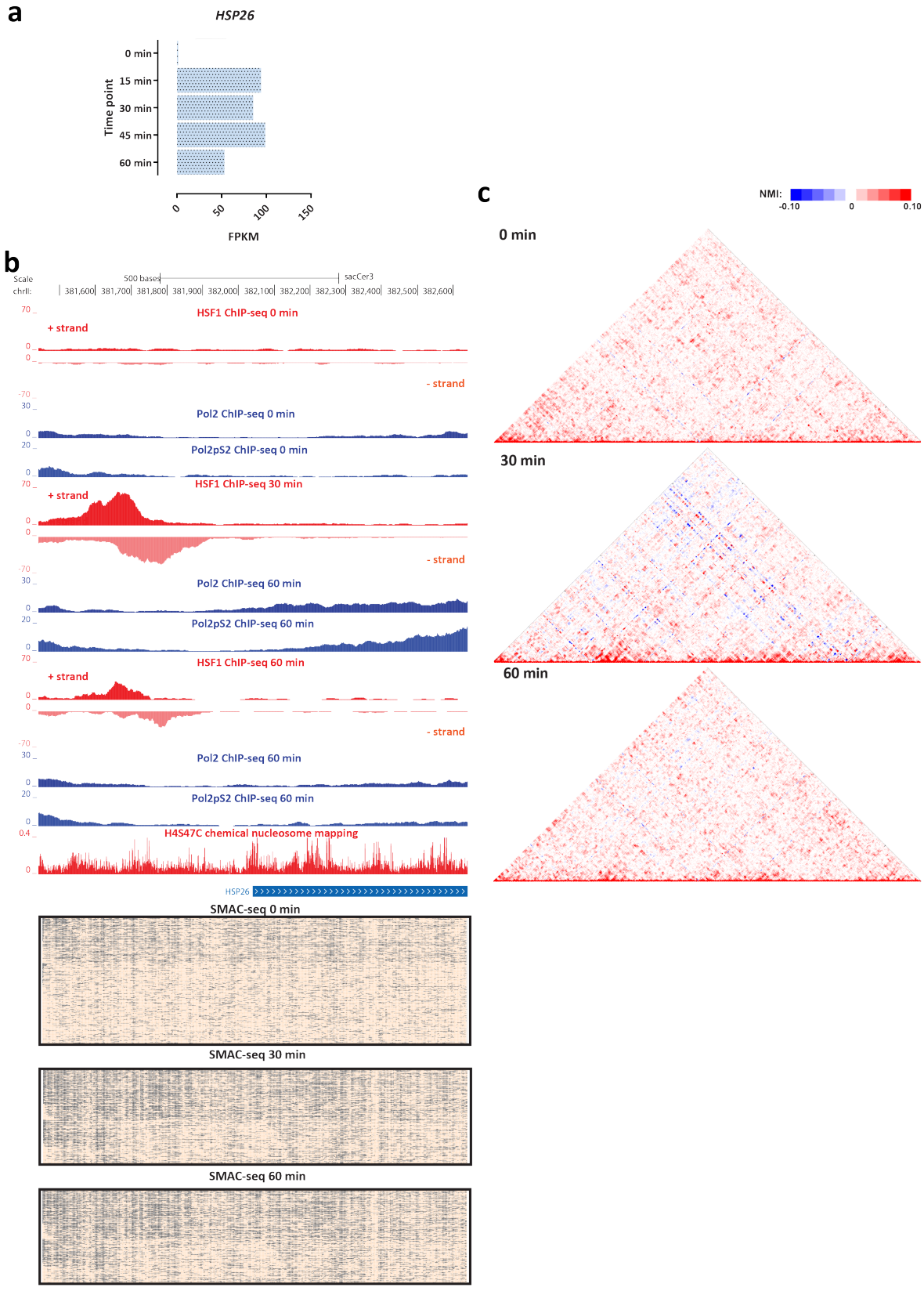

Supplementary Figure 95: Coordinated changes in chromatin accessibility and nucleosomal occupancy during the yeast stress response. Shown are changes in RNA Polymerase and HSF1 occupancy (measured by ChIP-seq), SMAC-seq profiles (1-bp resolution, 10-bp aggregate scores) and NMI profiles in the vicinity of the *HSP26* gene.

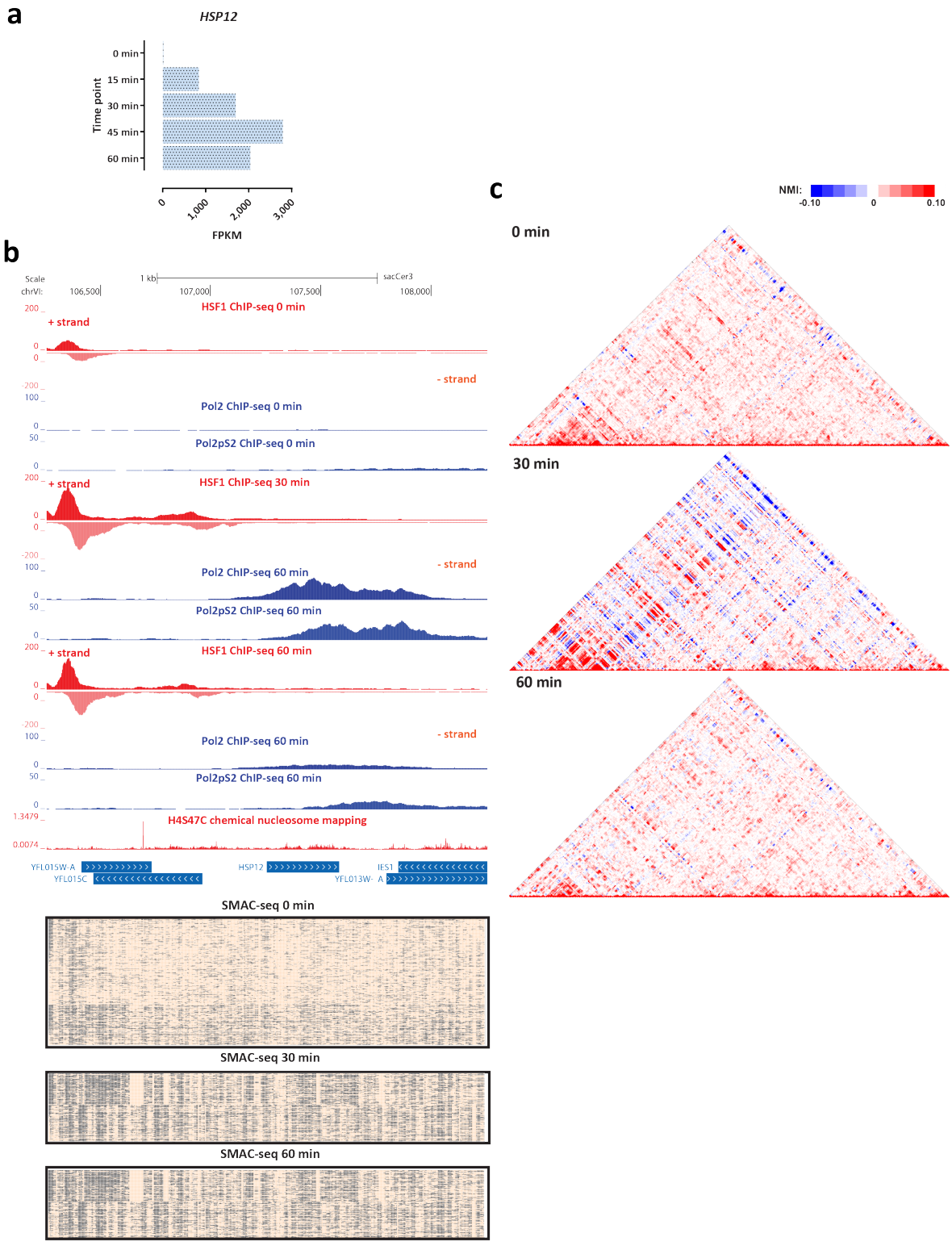

Supplementary Figure 96: Coordinated changes in chromatin accessibility and nucleosomal occupancy during the yeast stress response. Shown are changes in RNA Polymerase and HSF1 occupancy (measured by ChIP-seq), SMAC-seq profiles (1-bp resolution, 10-bp aggregate scores) and NMI profiles in the vicinity of the *HSP12* gene.

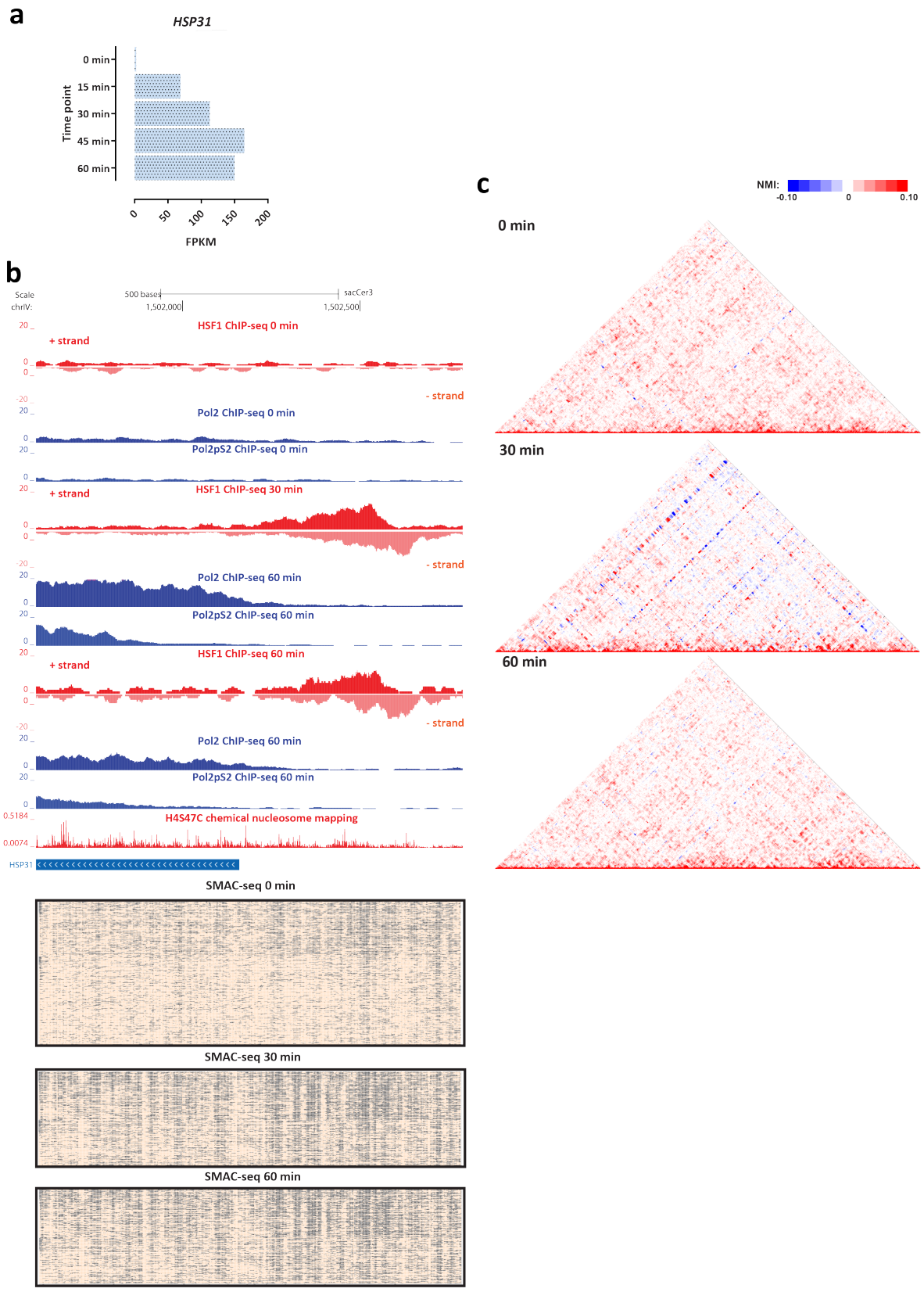

Supplementary Figure 97: Coordinated changes in chromatin accessibility and nucleosomal occupancy during the yeast stress response. Shown are changes in RNA Polymerase and HSF1 occupancy (measured by ChIP-seq), SMAC-seq profiles (1-bp resolution, 10-bp aggregate scores) and NMI profiles in the vicinity of the *HSP31* gene.

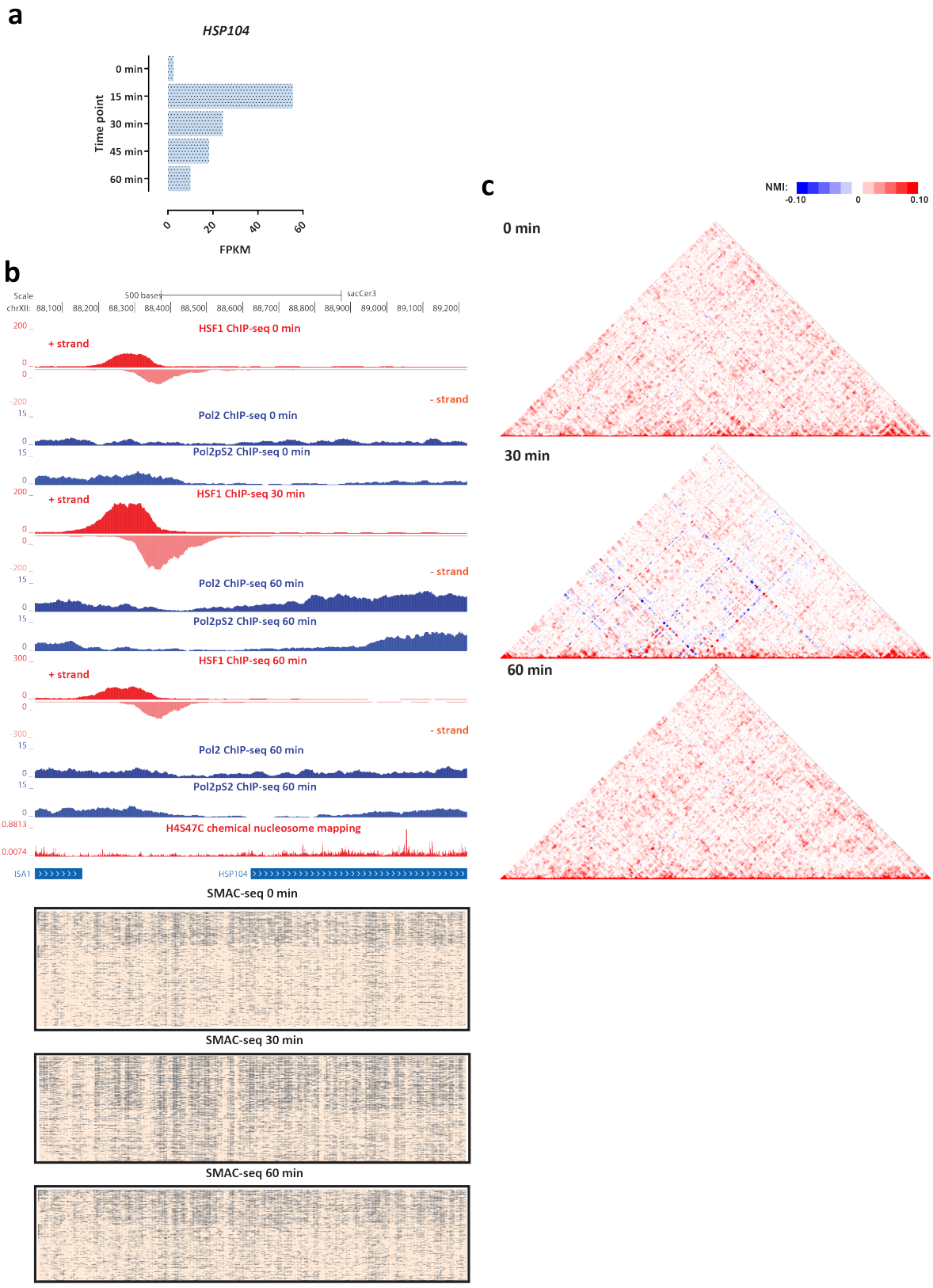

Supplementary Figure 98: Coordinated changes in chromatin accessibility and nucleosomal occupancy during the yeast stress response. Shown are changes in RNA Polymerase and HSF1 occupancy (measured by ChIP-seq), SMAC-seq profiles (1-bp resolution, 10-bp aggregate scores) and NMI profiles in the vicinity of the *HSP104* gene.

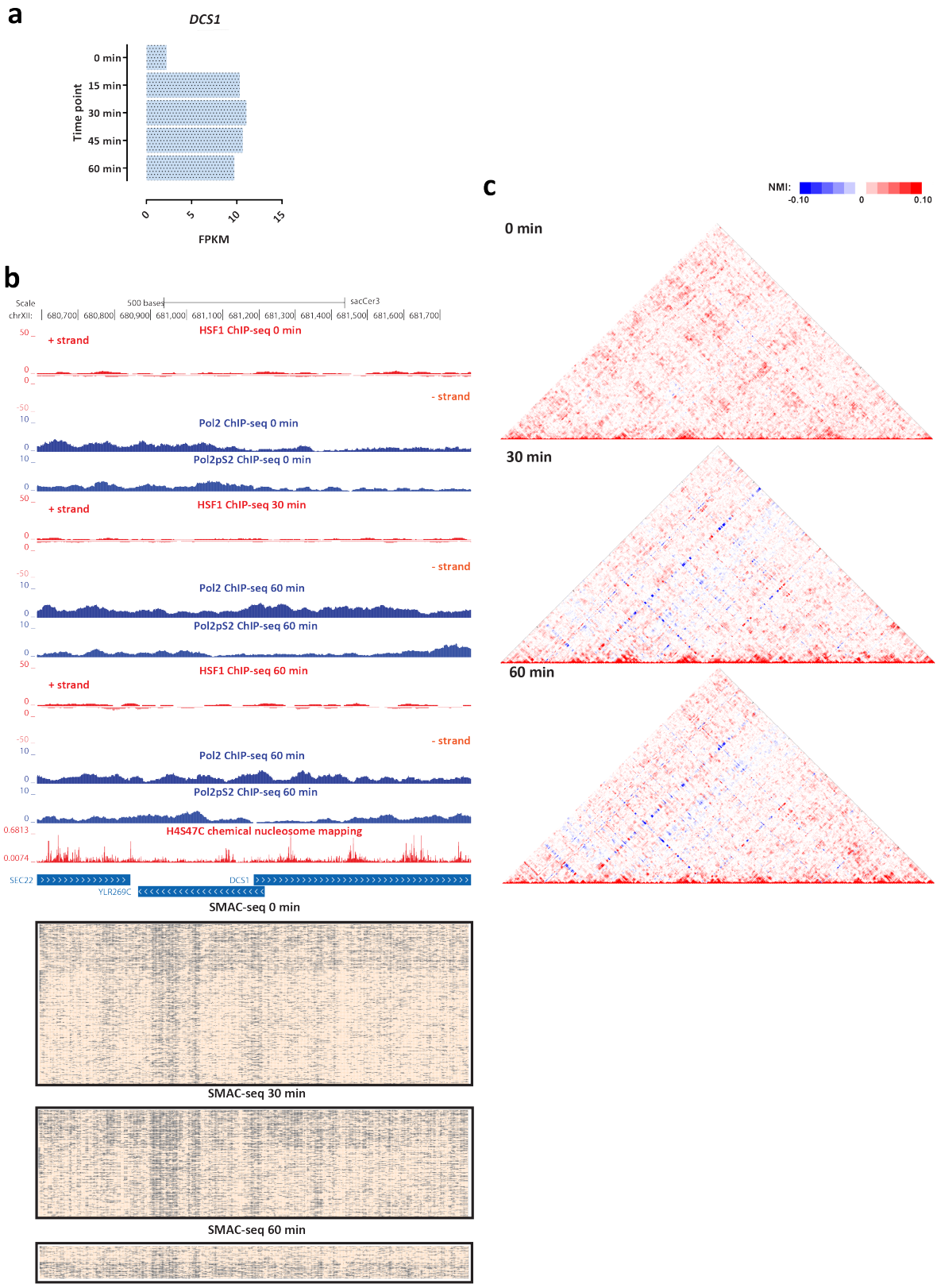

Supplementary Figure 99: Coordinated changes in chromatin accessibility and nucleosomal occupancy during the yeast stress response. Shown are changes in RNA Polymerase and HSF1 occupancy (measured by ChIP-seq), SMAC-seq profiles (1-bp resolution, 10-bp aggregate scores) and NMI profiles in the vicinity of the *DSC1* gene.

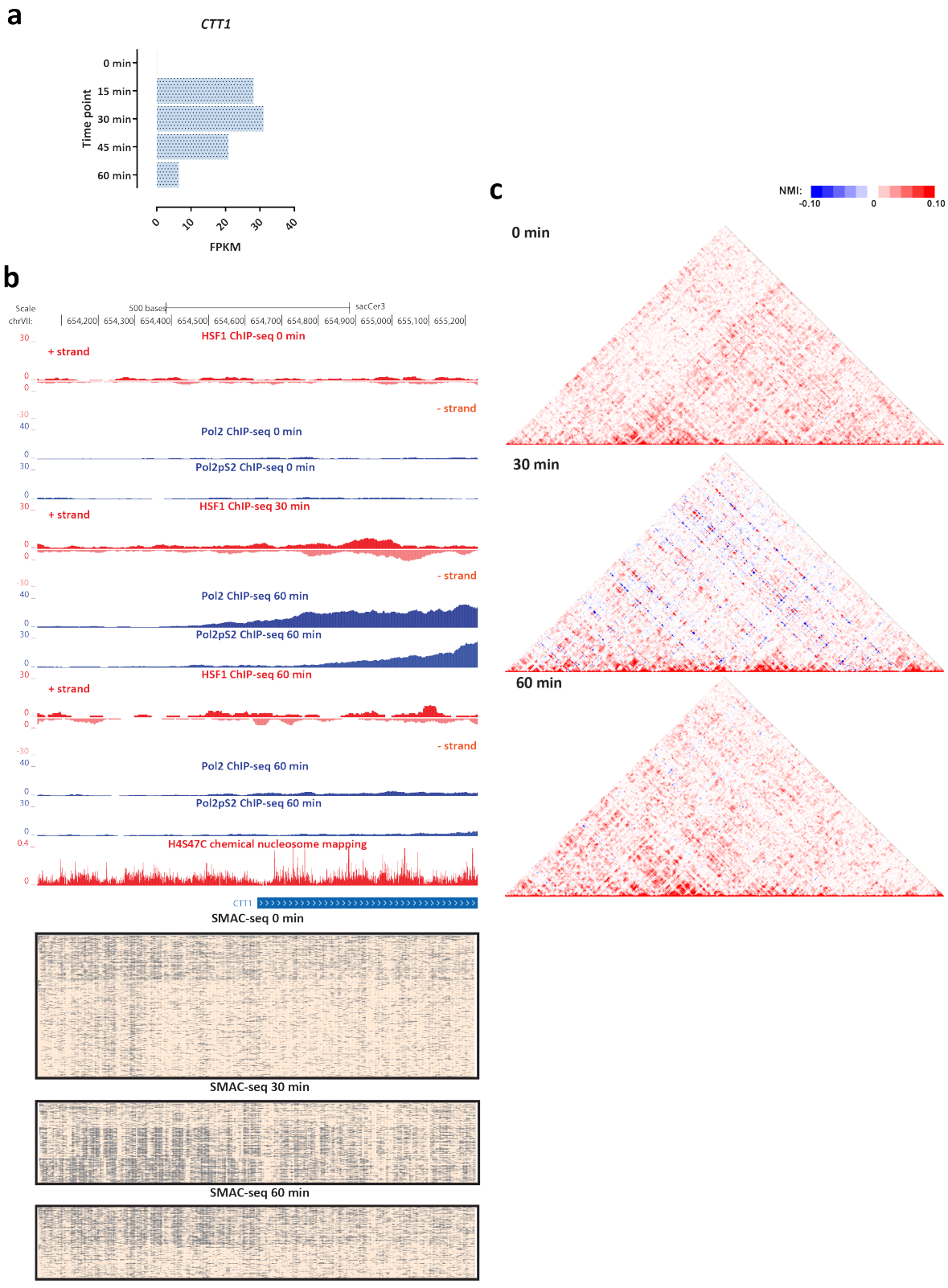

Supplementary Figure 100: Coordinated changes in chromatin accessibility and nucleosomal occupancy during the yeast stress response. Shown are changes in RNA Polymerase and HSF1 occupancy (measured by ChIP-seq), SMAC-seq profiles (1-bp resolution, 10-bp aggregate scores) and NMI profiles in the vicinity of the *CTT1* gene.

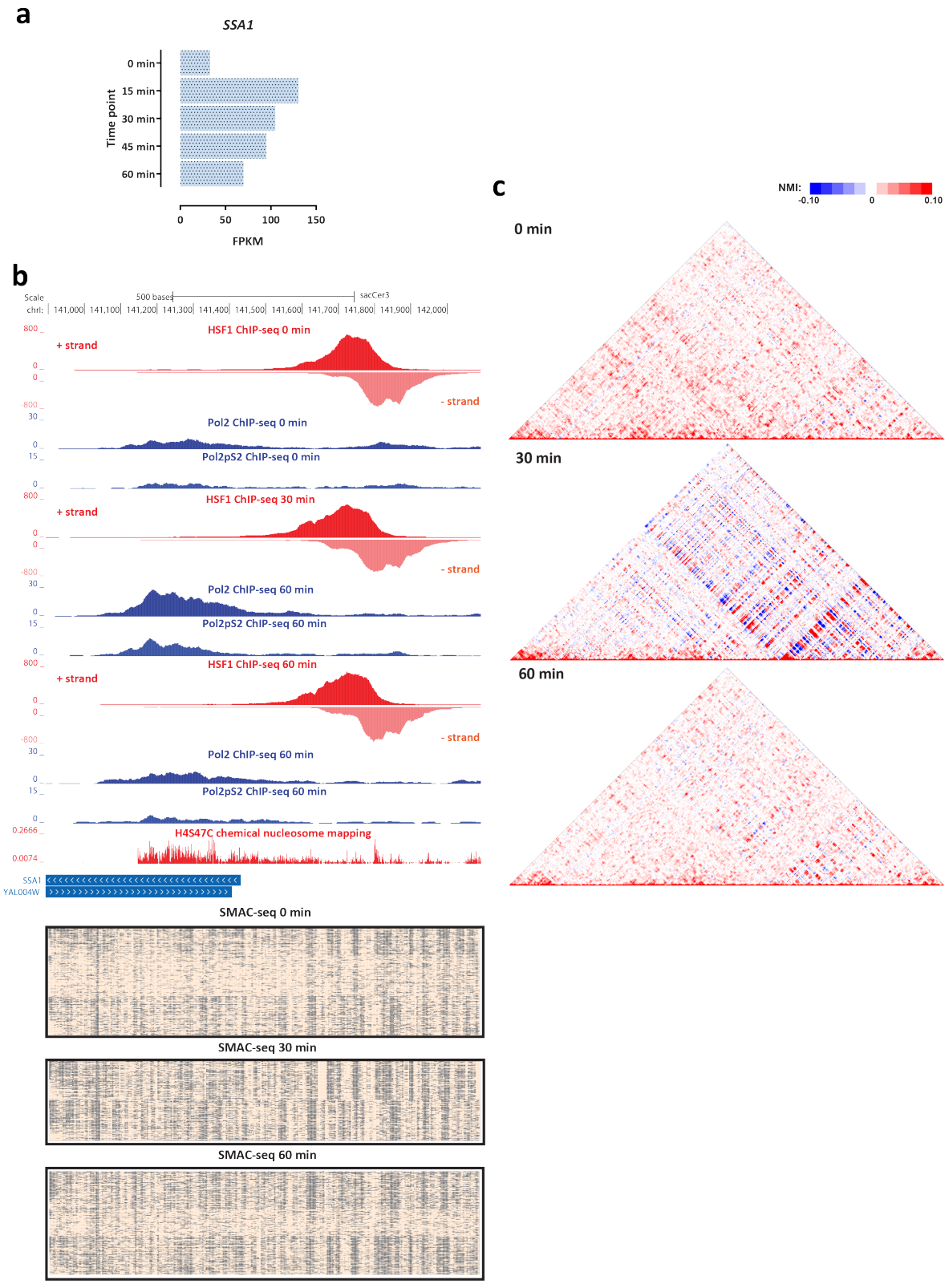

Supplementary Figure 101: Coordinated changes in chromatin accessibility and nucleosomal occupancy during the yeast stress response. Shown are changes in RNA Polymerase and HSF1 occupancy (measured by ChIP-seq), SMAC-seq profiles (1-bp resolution, 10-bp aggregate scores) and NMI profiles in the vicinity of the *SSA1* gene.

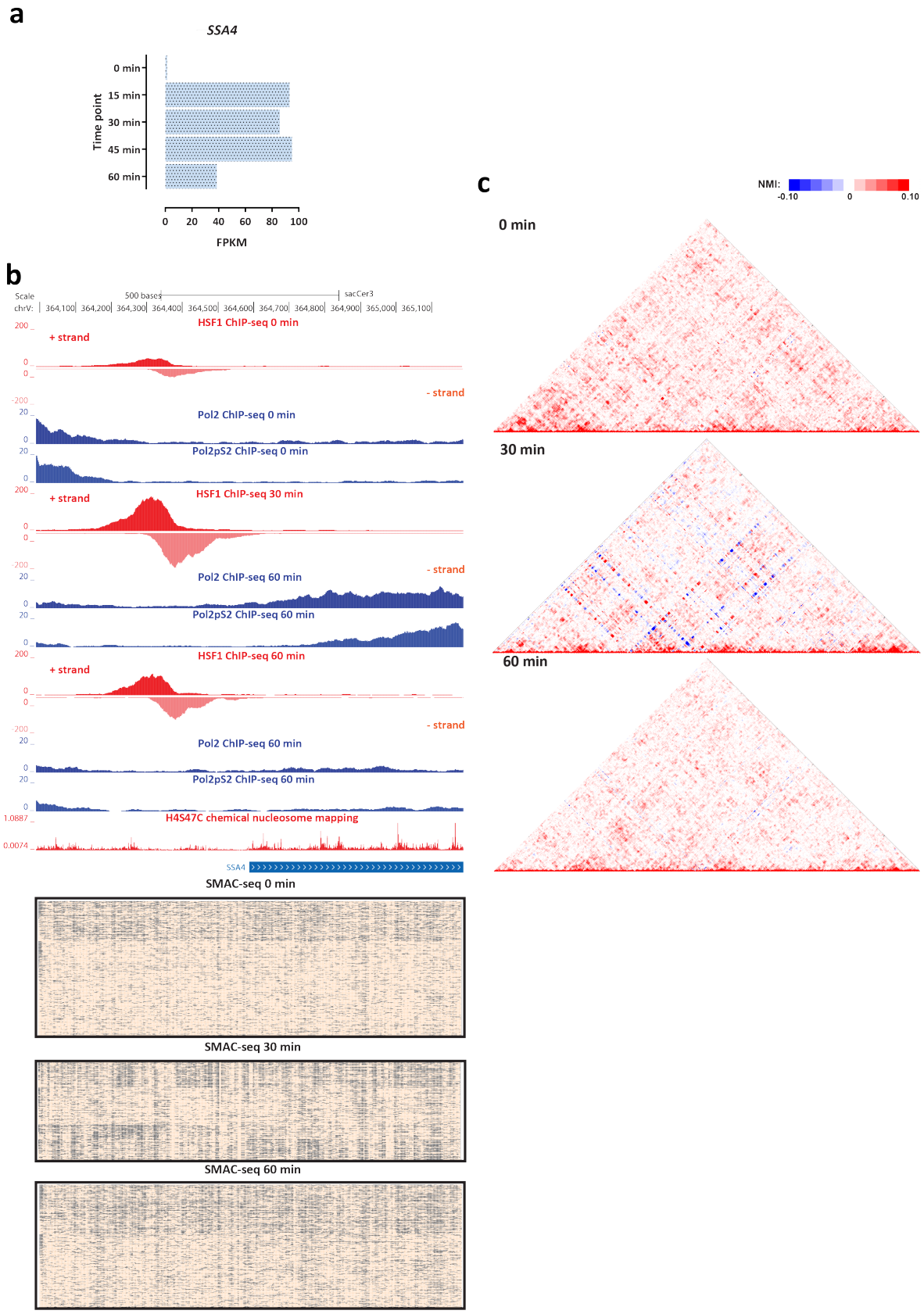

Supplementary Figure 102: Coordinated changes in chromatin accessibility and nucleosomal occupancy during the yeast stress response. Shown are changes in RNA Polymerase and HSF1 occupancy (measured by ChIP-seq), SMAC-seq profiles (1-bp resolution, 10-bp aggregate scores) and NMI profiles in the vicinity of the *SSA4* gene.

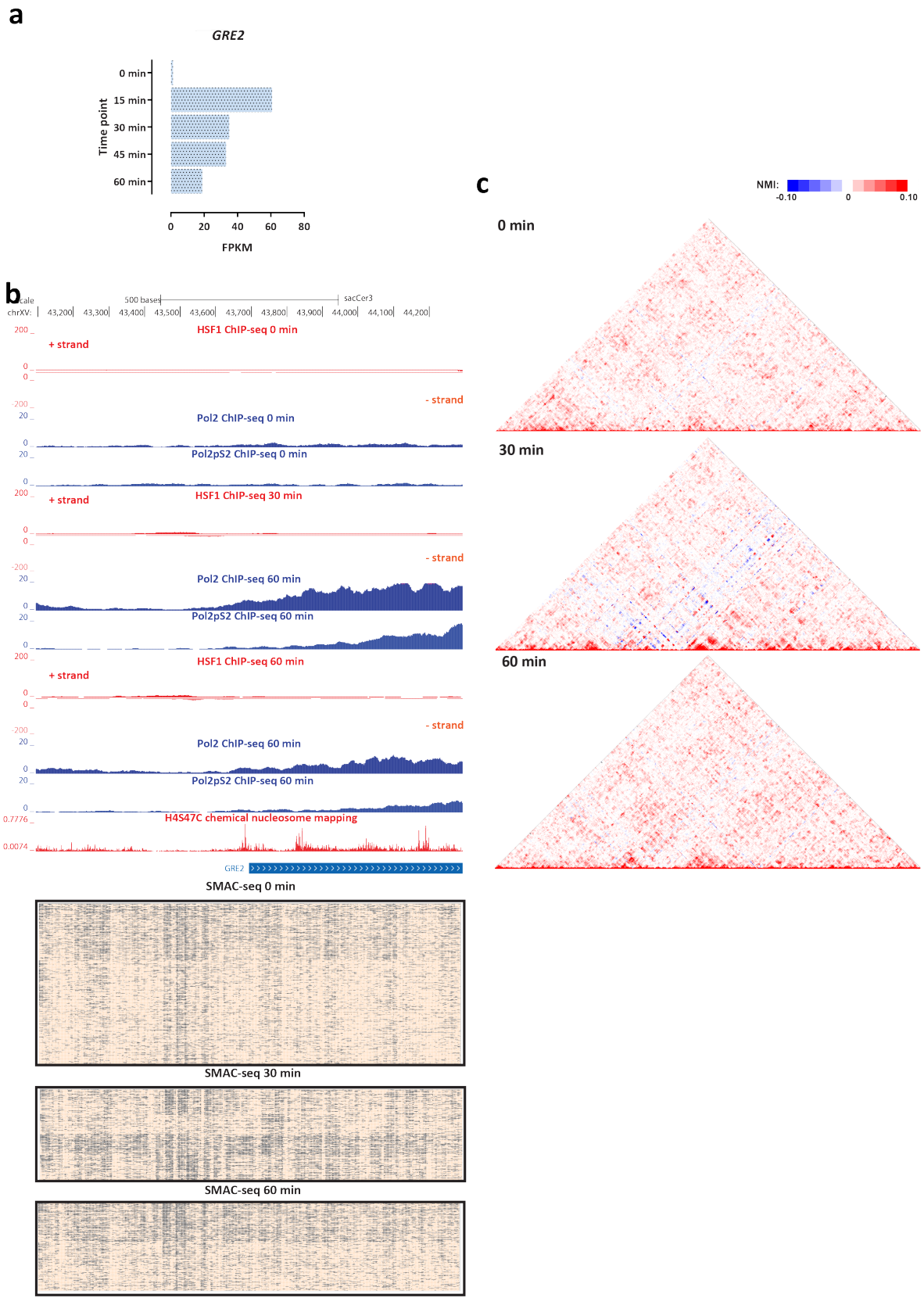

Supplementary Figure 103: Coordinated changes in chromatin accessibility and nucleosomal occupancy during the yeast stress response. Shown are changes in RNA Polymerase and HSF1 occupancy (measured by ChIP-seq), SMAC-seq profiles (1-bp resolution, 10-bp aggregate scores) and NMI profiles in the vicinity of the *GRE2* gene.

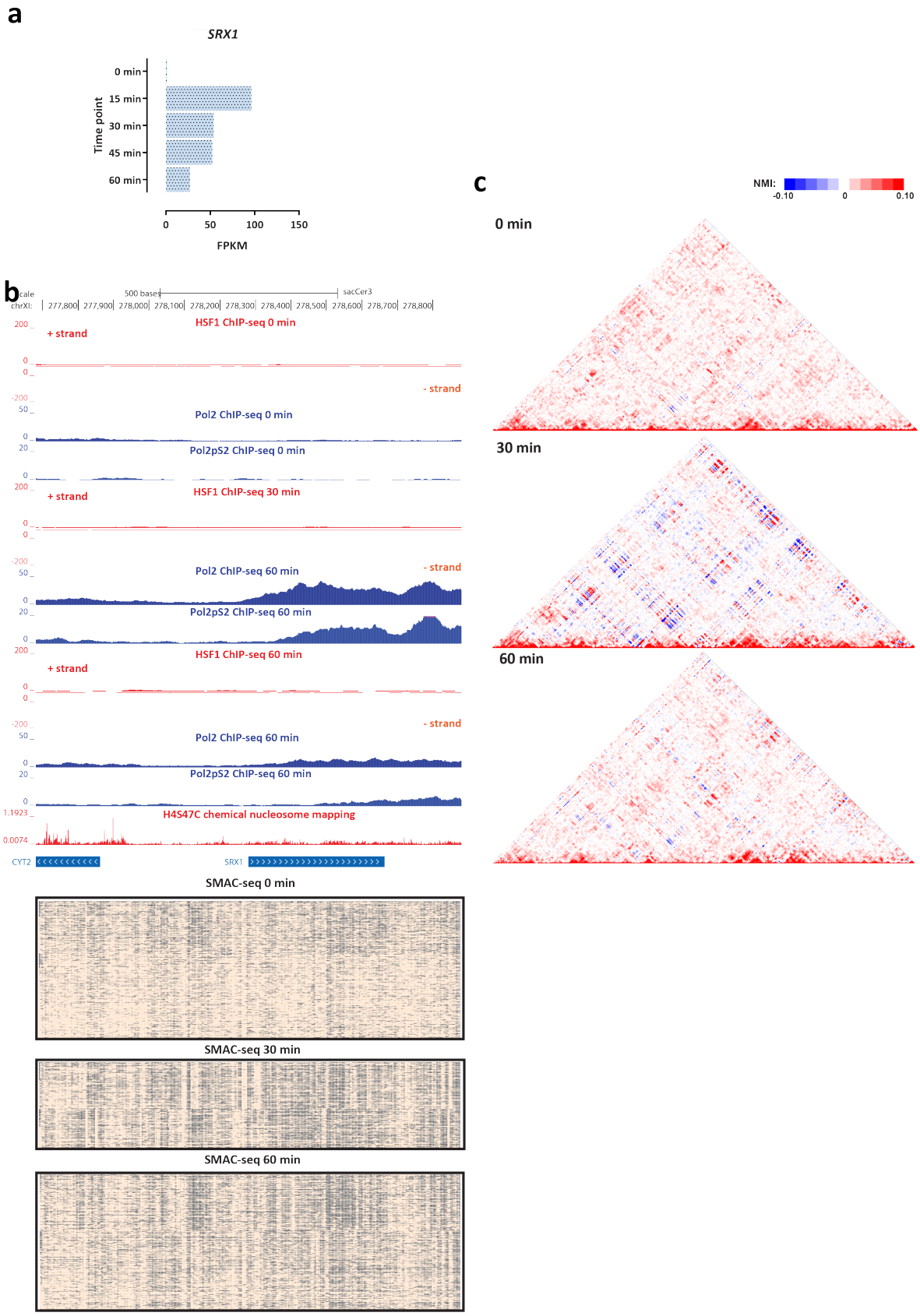

Supplementary Figure 104: Coordinated changes in chromatin accessibility and nucleosomal occupancy during the yeast stress response. Shown are changes in RNA Polymerase and HSF1 occupancy (measured by ChIP-seq), SMAC-seq profiles (1-bp resolution, 10-bp aggregate scores) and NMI profiles in the vicinity of the *SRX1* gene.

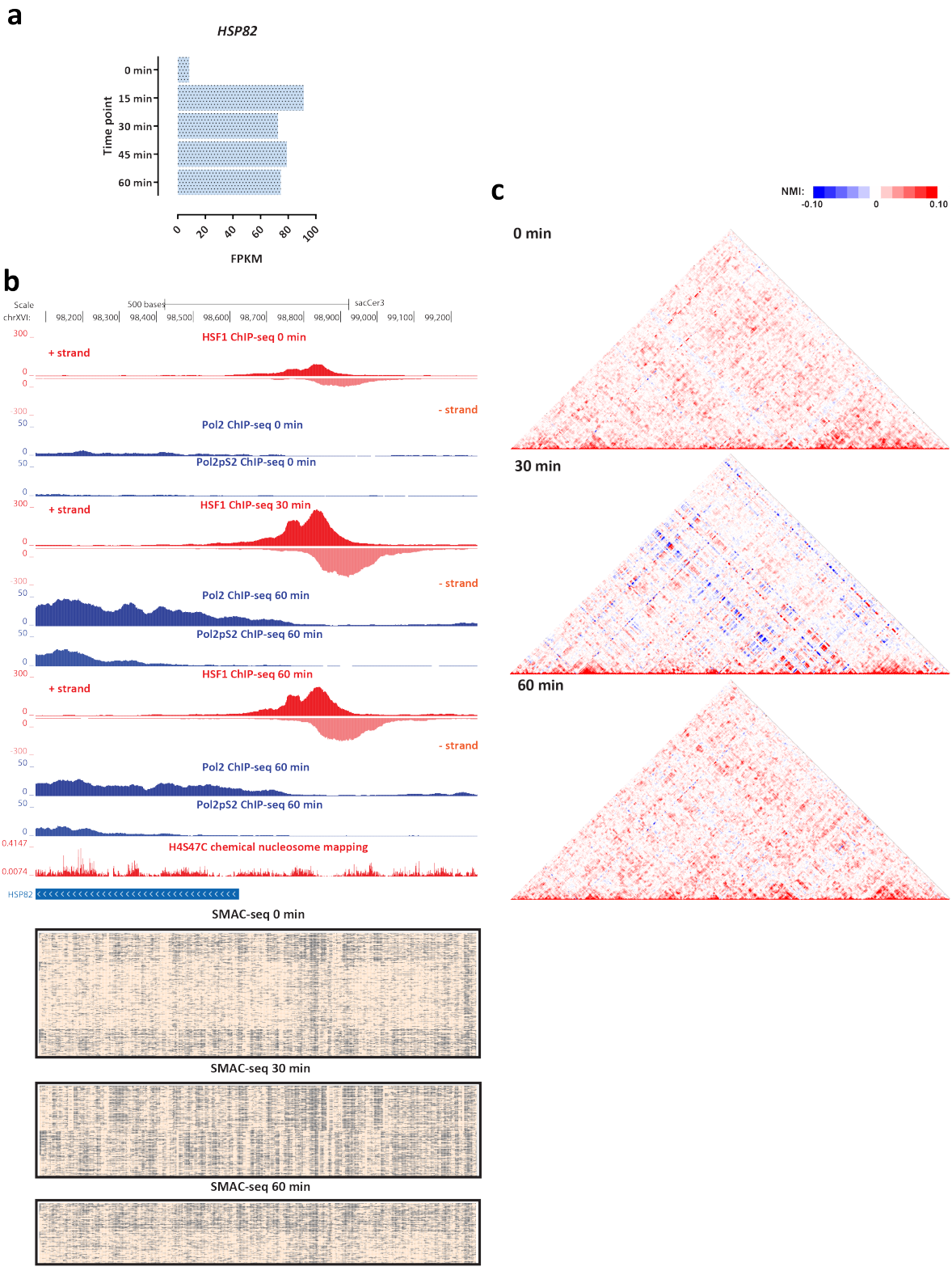

Supplementary Figure 105: Coordinated changes in chromatin accessibility and nucleosomal occupancy during the yeast stress response. Shown are changes in RNA Polymerase and HSF1 occupancy (measured by ChIP-seq), SMAC-seq profiles (1-bp resolution, 10-bp aggregate scores) and NMI profiles in the vicinity of the *HSP82* gene.

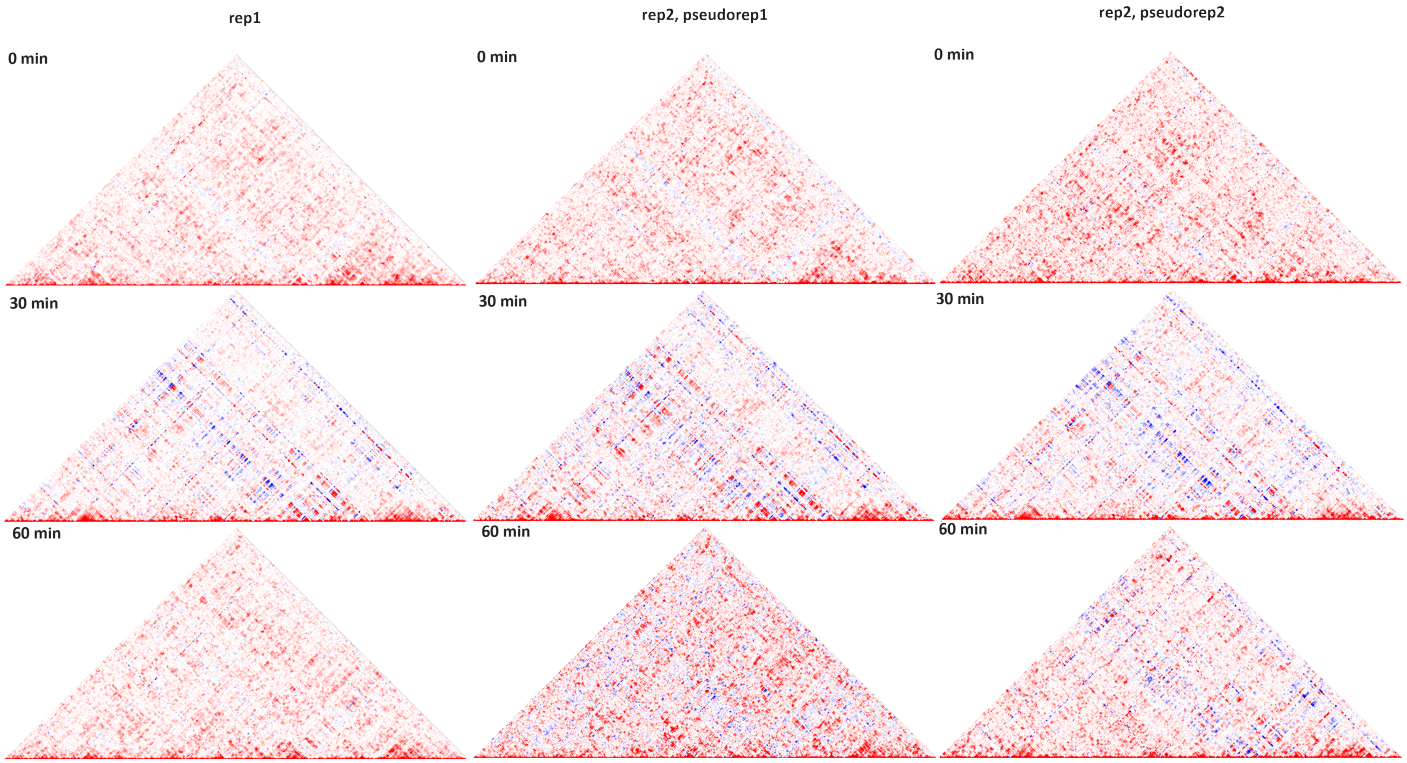

Supplementary Figure 106: Coordinated changes in chromatin accessibility and nucleosomal occupancy during the yeast stress response around the *HSP82* gene. Shown are NMI profiles in the vicinity of the *HSP82* gene for the first replicate of the diamide time course as well as for pseudoreplicates (generated by randomly splitting reads in two halves) from the second replicate of the diamide time course.

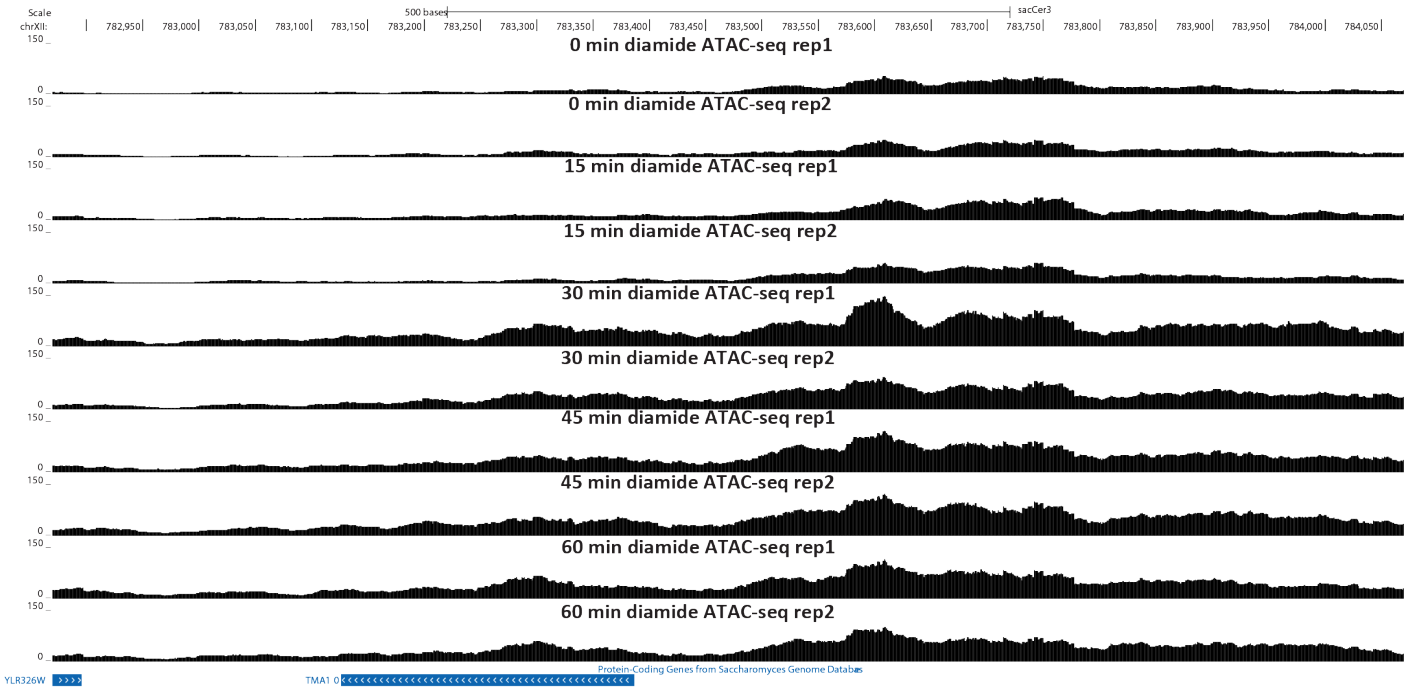

Supplementary Figure 107: Changes in chromatin accessibility during the yeast stress response around the *TMA10* gene as measured by ATAC-seq.

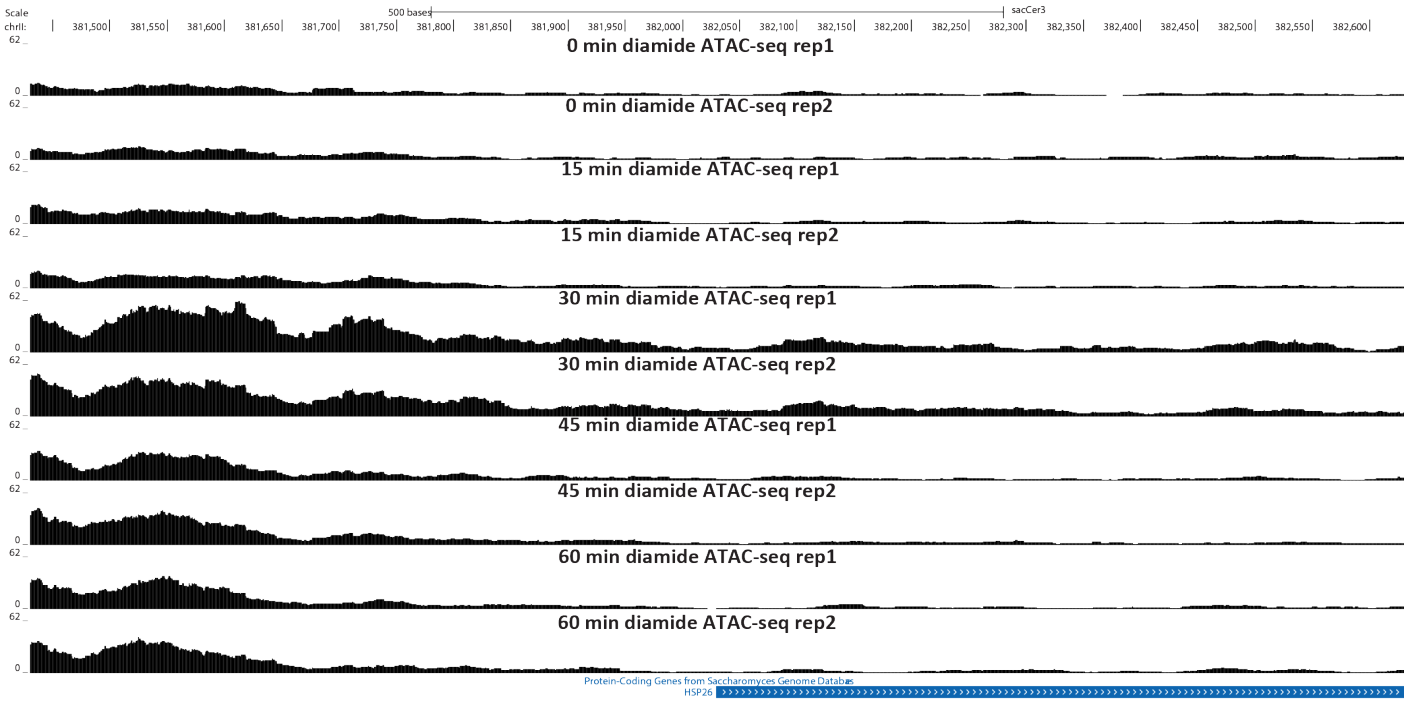

Supplementary Figure 108: Changes in chromatin accessibility during the yeast stress response around the *HSP26* gene as measured by ATAC-seq.

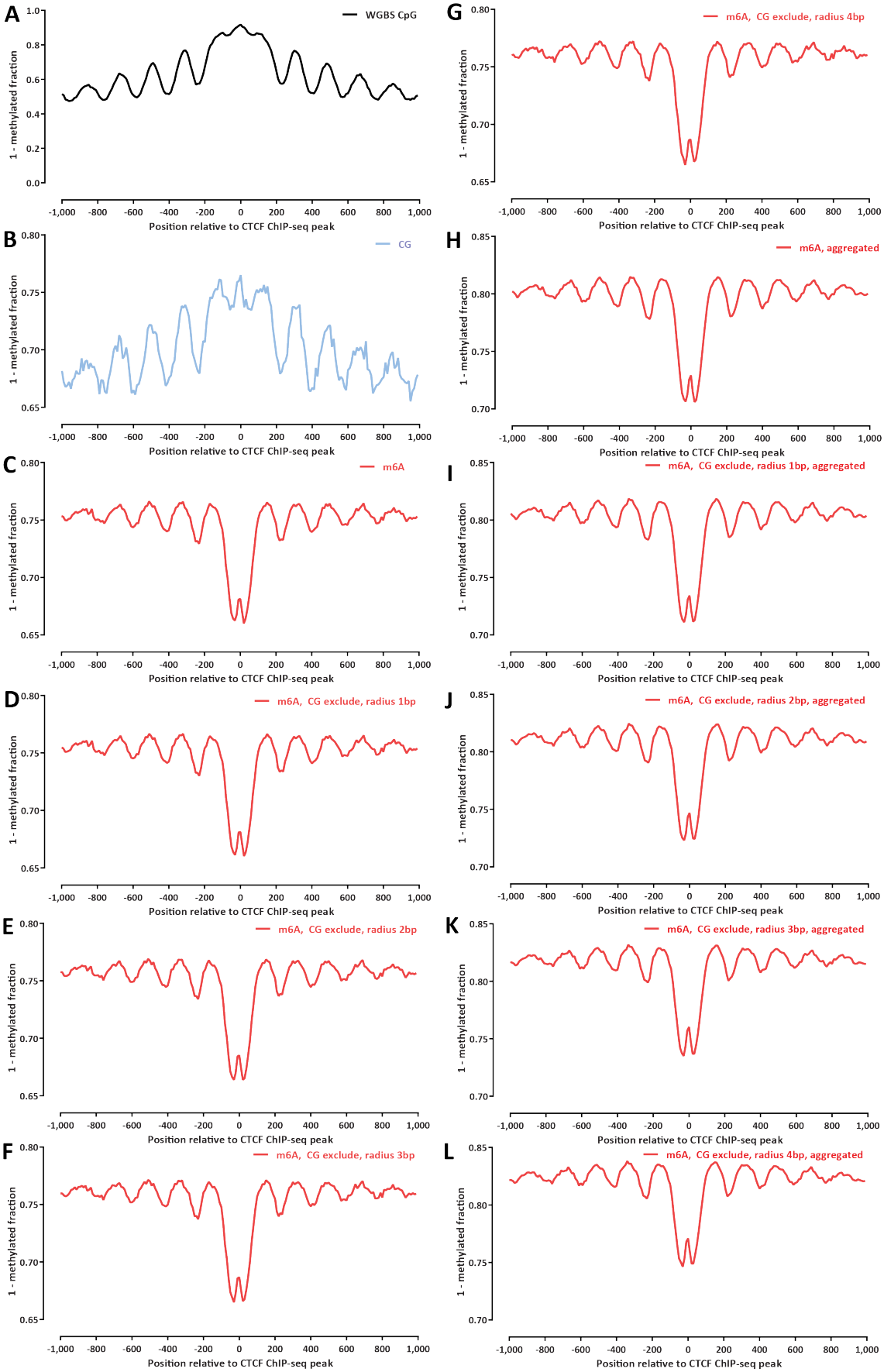
A
WGBS CpG
B
CG
C
m6A
D
m6A, CG exclude, radius 1bp
E
m6A, CG exclude, radius 2bp
F
m6A, CG exclude, radius 3bp
G
m6A, CG exclude, radius 4bp
H
m6A, aggregated
I
m6A, CG exclude, radius 1bp, aggregated
J
m6A, CG exclude, radius 2bp, aggregated
K
m6A, CG exclude, radius 3bp, aggregated
L
m6A, CG exclude, radius 4bp, aggregated
1 - methylated fraction
Position relative to CTCF ChIP-seq peak
-1,000 -800 -600 -400 -200 0 200 400 600 800 1,000

Supplementary Figure 109 *(preceding page)*: Detection of chromatin accessibility features around CTCF ChIP-seq peak summits in human GM12878 cells using m^{6}A-SMAC-seq. (a) Whole-genome bisulfite sequencing data (obtained from the ENCODE Consortium) (b) CpG methylation (from m^{6}A-SMAC-seq experiment generated by this study) (c) m^{6}A methylation (from m^{6}A-SMAC-seq experiment generated by this study), average profile; (d) m^{6}A methylation (excluding A positions within 1 bp of a CpG dinucleotide), average profile; (e) m^{6}A methylation (excluding A positions within 2 bp of a CpG dinucleotide), average profile; (f) m^{6}A methylation (excluding A positions within 3 bp of a CpG dinucleotide), average profile; (g) m^{6}A methylation (excluding A positions within 4 bp of a CpG dinucleotide), average profile; (h) m^{6}A methylation (from m^{6}A-SMAC-seq experiment generated by this study), aggregate profile; (i) m^{6}A methylation (excluding A positions within 1 bp of a CpG dinucleotide), aggregate profile; (j) m^{6}A methylation (excluding A positions within 2 bp of a CpG dinucleotide), aggregate profile; (k) m^{6}A methylation (excluding A positions within 3 bp of a CpG dinucleotide), aggregate profile; (l) m^{6}A methylation (excluding A positions within 4 bp of a CpG dinucleotide), aggregate profile.

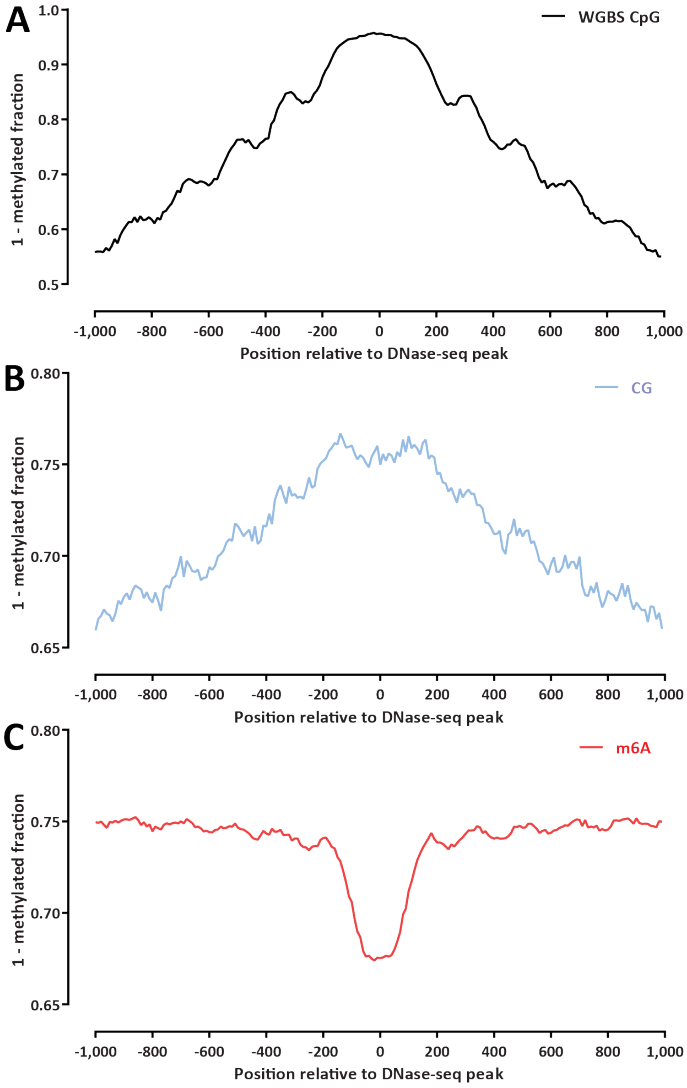

Supplementary Figure 110: Average profiles of endogenous DNA methylation and m^{6}A-SMAC-seq around DNase hypersensitive sites in human GM12878 cells. (a) Whole-genome bisulfite sequencing data (obtained from the ENCODE Consortium); (b) CpG methylation (from m^{6}A-SMAC-seq experiment generated by this study); (c) m^{6}A methylation (from m^{6}A-SMAC-seq experiment generated by this study).

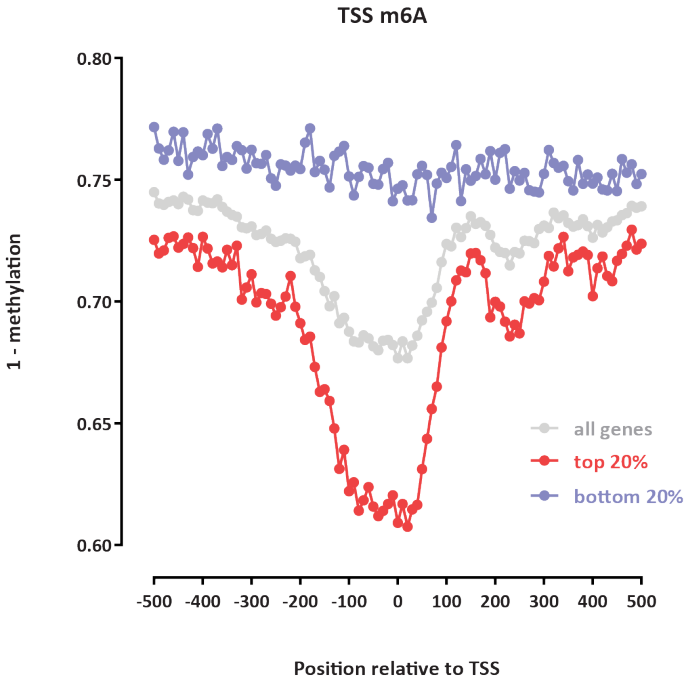

Supplementary Figure 111: Measurement of chromatin accessibility around transcription start sites using m^{6}A-SMAC-seq human GM12878 cells. Shown are the average m^{6}A-SMAC-seq around all protein coding genes, as well as the top 20% and the bottom 20% of genes in GM12878 cells (as determined using RNA-seq measurements provided by the ENCODE Consortium).